MASARYK UNIVERSITY
Faculty of Science
Institute of Condensed Matter Physics

and

JOHANNES KEPLER UNIVERSITÄT LINZ
Technisch-Naturwissenschaftliche Fakultät
Institute of Semiconductor and Solid State Physics

Jiří Novák

Structural investigations of nano-islands using X-ray diffraction techniques

Doctoral thesis

Supervisors: Prof. RNDr. Václav Holý, CSc. (MU Brno)
Univ.-Prof. Dr. Günther Bauer (JKU Linz)

Brno, May 2006

Bibliografická identifikace (Bibliographical data)

Jméno a přijmení (first name and surname): Jiří Novák

Název disertační práce (dissertation title CZ): Studium struktury nano-ostrůvků rentgenovou difrakcí

Název disertační práce anglicky (EN): Structural investigations of nano-islands using X-ray diffraction techniques

Studijní program (study program): Fyzika (Physics)

Studijní obor (study branch): Fyzika pevných látek (Solid state physics)

Školitelé (supervisors): Prof. RNDr. Václav Holý, CSc. a Univ.-Prof. Dr. Günther Bauer

Rok obhajoby (year of defence): 2006

Klíčová slova (key-words CZ): rentgenová difrakce, strukturní analýza, kvantové tečky, nano-ostrůvky, struktura ostrůvků, tří-dimenzionální krystaly, arsenid india, arsenid galia, křemík, germanium, polovodiče, samouspořádání, pružnost, deformace, mikroskopie atomových sil, fotoluminiscence, transmisní elektronová mikroskopie

Klíčová slova v angličtině (EN): X-ray diffraction, structural analysis, quantum dots, nano-islands, island structure, three-dimensional crystals, indium arsenide, gallium arsenide, silicon, germanium, semiconductors, self-assembly, elasticity, deformation, atomic force microscopy, photoluminescence, transmission electron microscopy

Abstract

The thesis deals with structural characterization of quantum dots and nano-islands by means of X-ray diffraction. Coplanar high-angle X-ray diffraction and experiments in grazing-incidence diffraction geometry are applied for investigations of nano-islands grown in Stranski-Krastanow growth mode. In particular we dealt with the following systems: (i) InAs/GaAs(001) quantum-dots grown by molecular beam epitaxy and capped with GaAs, (ii) 11-stack multilayer of laterally ordered and unordered InAs/GaAs quantum-dots grown by molecular beam epitaxy, (iii) Ge/Si(001) nano-islands forming a three-dimensional island crystal, and (iv) In(Ga)As/ GaAs(001) islands grown by low-pressure metal-organic vapour-phase-epitaxy. For the latter we studied effects of island capping with Ga(In)As, and effects of annealing. The results of X-ray analysis are correlated with results obtained by atomic force microscopy, transmission electron microscopy, photoluminescence, and band gap calculations. Furthermore, we discuss and apply new methods for analysis of X-ray diffraction data to obtain structural information on the studied nano-islands: (i) A generalization of the iso-strain scattering method for buried nano-islands is introduced. The method allows for the characterization of strain fields in buried islands and for obtaining the geometry (size and shape) of islands from X-ray data measured in grazing-incidence diffraction geometry without any model assumption on the island shape. (ii) A method for extracting structural information on laterally ordered and unordered nano-islands in cases when X-ray scattering signals from both classes of islands are mixed in the detected data. The procedure also allows for determination of the mean displacement of the ordered nano-islands from the two-dimensional lattice sites. (iii) The combination of an analytical solution of the equilibrium equations of linear elasticity with kinematical X-ray scattering theory is used for structural analysis of a three-dimensional island crystal.

Abstrakt

Disertační práce je zaměřena na studium struktury kvantových teček a nano-ostrůvků difrakcí rentgenových paprsků. Nano-ostrůvky rostlé v Stranski-Krastanowově modu jsou zkoumány pomocí koplanární vysokoúhlové rentgenové difrakce a difrakce při malých úhlech dopadu a výstupu. Konkrétně jsme se zabývali následujícími systémy: (i) InAs/GaAs(001) kvantovými tečkami rostlými pomocí epitaxe molekulových svazků (MBE) a překrytými vrstvou GaAs, (ii) 11-násobnou multivrstvou laterálně uspořádaných a neuspořádaných InAs/GaAs(001) kvantových teček (MBE růst), (iii) tří-dimenzionálním krystalem Ge/Si(001) nano-ostrůvků (MBE růst) a In(Ga)As nano-ostrůvků rostlými epitaxí z organokovových par při nízkém tlaku. Pro vzorky s posledně jmenovanými ostrůvky jsme studovali efekt překrytí ostrůvků Ga(In)As a efekt žíhání. Výsledky rentgenových analýz jsou srovnávány s výsledky obdrženými mikroskopií atomových sil, transmisní elektronovou mikroskopií, fotoluminescencí a výpočty pásových struktur. Dále diskutujeme nové metody pro analýzu dat z rentgenové difrakce, které jsou použity k strukturní charakterizaci studovaných nano-ostrůvků. Jedná se o: (i) Rozšíření metody rozptylu na oblastech konstantní deformace na analýzu překrytých ostrůvků. Pomocí této metody lze určit rozložení deformačního pole v překrytých ostrůvcích a geometrii ostrůvků (velikost a tvar) aniž by byl předpokládán model jejich tvaru. (ii) Metodu umožňující extrahovat strukturní informace o laterálně uspořádaných a neuspořádaných ostrůvcích v případech, kdy jsou současně detekovány signály z obou typů ostrůvků. Tento postup dále poskytuje střední odchylku uspořádaných ostrůvků z uzlů dvou-dimenzionální mřížky. (iii) Kombinaci analytického řešení rovnic rovnováhy lineární elasticity s teorií kinematického rozptylu rentgenova záření, která je použita pro analýzu tří-dimenzionálního krystalu ostrůvků.

Contents

Chapter 1

Introduction

This thesis presents a small contribution to the heap of X-ray methods for the characterization of self assembled semiconductor *quantum dots* (QDs) and *nano-islands*. Before introducing these methods, let us briefly review the history and applications of QDs and nano-islands as well as methods for their characterization. A comprehensive report on applications and physical properties of semiconductor QDs is given in Ref. [BGL99]. For a more recent review of the structural properties of QDs and nano-islands, their growth, and experimental methods for their characterization see Ref. [SHB04].

1.1 History and applications of quantum dots and nano-islands — the motivation

By late 1960's, advent of the novel epitaxial growth techniques, e.g., molecular beam epitaxy and metal organic vapour phase deposition, enabled fabrication of semiconductor heterostructures, so-called nanostructures, in which free carriers are restricted to an extremely small space in range 1–100 nm. The confinement of the carrier motion is achieved by embedding a low bandgap material in a high band gap material, i.e., by potential barriers. This confinement in one, two, or three dimensions, in the case of quantum wells or quantum superlattices, quantum wires, and QDs, respectively, leads to a modified density of states with respect to bulk solids. Three-dimensional carrier motion confinement takes place also in nano-islands. However, they are just too large in the lateral direction to demonstrate quantum confinement effects. Thus, most people claim that they do not deserve to be named quantum dots.

Quantum wells and superlattices were mainly investigated in 1970's and 1980's. The main requirement for applications of these nanostructures is smoothness of the material interfaces. At the end of this period the growth technology and physical properties of these layered nanostructures were rather well understood. Nowadays, we encounter their applications in daily life, e.g., in lasers and detectors of CD players or cash registers, in high-frequency modulators of cellular phones, and in other telecommunication applications.

QDs as quasi-zero-dimensional objects attracted the interest of researchers since the end of 1980's. The main motivation was the complete spatial carrier confinement resulting in atom-like energy spectra [KAT01] and higher density of states when compared to quantum wires and quantum wells. Nowadays, among a variety of nanofabrication techniques [BGL99, GXS$^+$05], e.g., lithographic techniques, molding, embossing, and printing, the process of self-assembly in Stranski-Krastanow growth mode [SHB04] seems to be the most promising for producing defect free semiconductor QDs and nano-islands on a large scale. This process takes place in the epitaxy of materials having a lattice misfit with respect to the crystalline substrate. After growth of a strained planar layer, the so-called *wetting layer,* of a certain thickness, the strain energy relaxation occurs via a two-dimensional to three-dimensional transition. As a result, QDs or nano-islands, i.e., crystallites of the material of the layer, are formed on the top of the wetting layer. The resulting nanostructures can have various shapes and sizes depending on the growth conditions [VCG$^+$00, MWHM99, SNS99] and the postgrowth treatment [CRM$^+$04, RKvK01].

Nanostructures bring two advantages with respect to devices based on a simple p-n interface. First, various properties of the devices, e.g., wavelength of lasers, can be tuned by changing the structural properties of nanostructures, typically size and chemical composition. Secondly, reduced dimensionality leads to improved optical properties, especially increases the probability of electron-hole recombination and thus the gain of lasers and detectors.

Up to now many research groups have demonstrated fabrication of QD-based devices with promising properties. InAs/GaAs QDs are of interest for implementation in lasers and photodetectors for mid-infrared telecommunication applications. **QD lasers** have already outperformed properties of quantum well lasers. They show lower threshold currents, as low as 20 $A \cdot cm^{-2}$ at room temperature [PSHD00], and its independence on temperature up to 250 K (see review articles [Bim05, MS05]). Their main advantage is operation in transmission windows of the optical waveguides, i.e., at wavelengths of 1.3 μm and possibly also at 1.55 μm. **QD photodetectors** are unlike their quantum well counterparts sensitive to the normal incidence light due to the carrier confinement in all three directions. They provide higher detectivity, reduced dark current and enhanced response at elevated temperatures (see review articles [Kri05, MS05]).

One of the emerging applications of quantum dots is in the field of quantum information processing. InAs self-assembled QDs embedded in an optical microcavity can be used as **single photon sources** [MRG$^+$01, PSV$^+$02] and **sources of polarisation correlated photons** [SFP$^+$02], which are potential components of photon-based quantum information applications [LO05]. QDs can also provide an environment for storing qubits in the form of an exciton, i.e., electron-hole pair, or electron spin [LSGS04].

Two-dimensional arrays of SiGe nano-islands are proposed to realize **dot-based field-effect transistors** [SE01]. The misfit strains in Si above buried islands lead to band edge splitting and the inherently smaller effective masses of charge carriers promise faster transistors than are possible for pure Si devices.

Better understanding of the physics of QDs and nano-islands formation, the control of their structural properties, and their precise positioning is a prerequisite for their application on large scale. In particular, size, shape, and chemical composition of these nanostructures are important factors influencing their optical and electric performances. Analytical methods for structural characterization of nanostructures are indispensable aids, which give feedback to sample growers and shed light on the basic physics of nanostructures.

1.2 Characterization of QDs and nano-islands

This thesis focusses on X-ray diffraction techniques for the characterization of nanostructures. A combination of several analytical methods is usually required to obtain comprehensive structural characterization of QDs and nano-islands [1] (NI). Each method has certain advantages and limitations.

X-ray scattering techniques yield the intensity distribution in reciprocal space with a very high resolution. Therefore, X-rays are sensitive to very small changes of lattice parameters. Owing to the coherence length of several μm, information on electron density fluctuations on corresponding length scales can be obtained. Correlations of NI positions and their fluctuations can be studied due to that fact. The penetration depth of X-rays can be tuned between several nm and several hundred μm by controlling the incidence angle of the X-ray beam. Thus, one can non-destructively investigate both free-standing and buried NIs. Purely chemical sensitivity or sensitivity to both material composition and strain fields can be achieved by scanning reciprocal space for small scattering angles or in the vicinity of Bragg reflections of the substrate. These facts make X-ray scattering almost an ideal tool for studying NIs.

However, there are also disadvantages of X-ray scattering techniques: (i) Since the experimental data are obtained in reciprocal space, they must be mostly interpreted using simulations. The structural parameters of a model NI are iteratively fitted to obtain a satisfactory agreement between simulations and experiment. In the case of X-ray diffraction, this process involves demanding calculations of strain fields. Nevertheless, both strain fields and chemical composition distribution in NIs influence photoluminescence (PL) spectra and transmission electron microscopy (TEM) images and the same demanding approach of forward simulations have to be applied to obtain their spatial distribution. (ii) Existence of different types of NIs, which differ substantially in size or shape, can not be simply resolved from X-ray reciprocal space images. Here, direct imaging techniques, i.e., atomic force microscopy (AFM), TEM, and scanning tunnelling microscopy (STM), are of much help for establishing a starting model for X-ray simulations. (iii) Due to the small volume fraction of NIs compared with X-ray penetration depth, the scattering signal is very weak and usage of intensive synchrotron radiation sources is unavoidable.

[1] For convenience, when there is no need to make explicite distinction, the notion nano-islands (NIs) involves also QDs throughout the rest of the thesis.

The potential of conventional X-ray scattering techniques can be enhanced by use of sophisticated methods such as anomalous X-ray scattering and diffraction anomalous fine structure spectroscopy. **Anomalous X-ray scattering** exploits large changes in scattering power of one of the sample's constituent elements in the vicinity of one of its absorbtion edges. Comparison of measurements at two different energies in this region simplifies disentanglement of contributions to the scattered intensity from strain fields and fluctuations in chemical composition.

Diffraction anomalous fine structure spectroscopy (DAFS) combines crystallographic sensitivity of X-ray diffraction with spectroscopic and short-range order sensitivity of absorbtion techniques. Local ordering of atoms, i.e., species of atoms bonded to each other and angles between the bonds, occurring in a region with given strain can be determined by means of DAFS.

Another widely employed characterization method is **photoluminescence spectroscopy** (PL). PL probes energy levels of NIs close to the band edges, which are relevant for optical applications. Size and chemical composition of NIs can be determined from simulations of measured PL spectra.

Raman spectroscopy enables the determination of average lateral and vertical strain components and average material composition in NIs.

The above listed methods based on interaction of electromagnetic radiation with solids bring mostly statistically averaged properties and their dispersions for whole ensembles of NIs. Statistically averaged properties are relevant for performances of devices. However, direct high-resolution images allow studying NI shapes in detail and local atom arrangements on surfaces.

AFM and **STM** are suitable for imaging of morphology of free-standing NIs. In particular, NI size and sidewall angles can be identified using both methods. While AFM can operate in ambient atmosphere and provide resolution of several nm in lateral direction, STM can be used only for conductive surfaces in high vacuum. Atomic resolution can be achieved laterally and vertically using STM. Additionally, the tunnelling current is sensitive to both strain and material composition. Similarly, **plane-view TEM** addresses these properties with a very high resolution. On the other hand, AFM images can be taken on areas up to 100×100 μm, much larger than for the later methods, which allows for characterisation of lateral correlations of NI positions. This is on the account of lateral resolution of individual NIs, however.

Cross-sectional STM and **cross-sectional TEM** are used to investigate buried NIs. Both techniques are able to resolve chemical distribution profile along the growth direction. Cleaving of a sample, which is required for both techniques, is demanding and destructive. Furthermore, observed properties depend on the location of the cleaved surface within investigated NI. In the case of TEM, the thickness of the cross-sectional slice is often comparable to the lateral size of NIs. Thus, this method gives laterally averaged images.

Real space images of small number of islands or nanocrystals and even their internal strains can be obtained using **coherent X-ray scattering** [RVW$^+$01, WPVR03, VRO$^+$05, CDB$^+$06]. However, in order to perform these experiments, the studied part of the sample has to be irradiated coherently with a sufficiently intense beam, i.e., with a micro-beam. This is possible due to recent developments in the field of X-ray optics and the third generation synchrotron sources. The real space island image is retrieved from measured X-ray interferences (speckle pattern) using an iterative numerical algorithm [MSC98, RV01].

1.3 Objectives and structure of this thesis

There are two main objectives of the presented work:

1. To generalize so-called iso-strain scattering method, i.e., a model-free method for obtaining the structure of free-standing QDs from X-ray data, so that it can be applied also to buried QDs

2. To study QDs and NIs ordered in 3D crystals and develop methods for obtaining their structural properties.

Chapter 2 summarizes applied experimental arrangements of X-ray scattering methods and some parts of X-ray theory. This chapter contains only excerpts on topics which are relevant for the thesis.

Chapter 3 introduces the generalization of the iso-strain scattering method for buried QDs. Simulations for various systems are shown and limitations of the method are discussed.

Chapter 4 presents studies on InAs/GaAs QDs grown by MBE. In particular, application of the generalized iso-strain scattering method is demonstrated. Furthermore, investigations on QDs ordered in a 3D QD crystal by means of grazing-incidence diffraction are presented here.

In Chapter 5 we will describe structural characterization of Ge/Si NIs ordered in a 3D NI crystal using high-resolution coplanar diffraction. An effective method for calculation of strain fields in a 3D NI crystal, which is required for simulations of presented X-ray data, is given here. The method is based on an analytical solution of the equilibrium equations of linear elasticity.

Chapter 6 presents structural studies on InGaAs/GaAs QDs and NIs grown by low-pressure metal-organic-vapour-phase epitaxy. In this case we dealt with rather complicated samples containing 3 types of QDs and NIs.

Chapter 2

X-ray scattering – general background

The first section of this chapter reviews some aspects of the X-ray scattering theory, which set the background for calculations of scattered intensity. X-ray scattering geometries applied throughout the thesis are presented in the second section. Both the theory and the experimental techniques were widely documented in many excellent textbooks; hence original works are not cited and the reader is referenced to Refs. [HPB99, Sch04]. The third section of this chapter reviews the iso-strain scattering method for free-standing QDs and NIs, i.e., a model-free method for obtaining structure of nanostructures from X-ray data. The generalization of this method for buried nanostructures, is presented in the next chapter. The last section reviews the anomalous scattering technique and its applications for characterization of NIs.

2.1 A short summary of X-ray scattering theory

The whole thesis deals only with Rayleigh scattering of X-rays, i.e., the contribution to elastic scattering made by the bound electrons of atoms. Thus, scattering from magnetic moments and atom nucleus, Compton scattering, and thermal diffuse scattering from phonons are neglected. Rayleigh scattering dominates the interaction of X-rays with solids. The theory in this section is restricted correspondingly.

2.1.1 Interaction of X-rays with solids

The interaction of X-rays with matter is described by the complex dielectric polarizability $\chi(\mathbf{r}, \lambda)$. It depends on the X-ray energy E and the momentum transfer of the scattering process $\mathbf{Q}$ as

$$\chi(\mathbf{r}, E, \mathbf{Q}) = -\frac{r_{\mathrm{el}} N_{\mathrm{A}} (hc)^2}{\pi E^2} \sum_l \frac{\varrho_{\mathrm{m},l}(\mathbf{r})}{A_l} [f_{0,l}(\mathbf{Q}) + f_l'(E) - \mathrm{i} f_l''(E)]. \tag{2.1}$$

Here N_A is Avogadro's number, $r_\mathrm{el} = 2.818 \times 10^{-5}$ Å is the classical electron radius, $\varrho_{\mathrm{m},l}(\mathbf{r})$ is the local partial mass density of an atomic species l and A_l is the corresponding atomic mass. $f_{0,l}(\mathbf{Q})$ is the atomic form factor and is defined as

$$f_{0,l}(\mathbf{Q}) = \int \mathrm{d}^3\mathbf{r}\, \varrho_{\mathrm{el},l}(\mathbf{r}) \mathrm{e}^{\mathrm{i}\mathbf{Q}\cdot\mathbf{r}}, \tag{2.2}$$

where $\varrho_{\mathrm{el},l}(\mathbf{r})$ is the electron density of the single atom of type l. In general, $f_{0,l}(\mathbf{Q})$ decreases with increasing $|\mathbf{Q}|$. The energy-dependent factors $f_l'(E)$ and $f_l''(E)$ correct for dispersion and absorption, respectively. They change substantially in the vicinity of absorption edges. An increase or a decrease of the polarizability in these energy regions is exploited in the anomalous X-ray techniques to enhance or to suppress scattering from a particular specie or a compound.

Since $\chi(\mathbf{r})$ follows the translation symmetry of the crystal, it can be expressed in the form of a Fourier series over the reciprocal lattice:

$$\chi(\mathbf{r}) = \sum_{\mathbf{g}} \chi_{\mathbf{g}} \mathrm{e}^{\mathrm{i}\mathbf{g}\cdot\mathbf{r}}. \tag{2.3}$$

The scattering of monochromatic X-rays is described by the stationary wave equation

$$(\triangle + K^2)\mathbf{E}(\mathbf{r}) = \mathbb{V}(\mathbf{r})\mathbf{E}(\mathbf{r}), \tag{2.4}$$

where $\mathbf{E}(\mathbf{r})$ is electric field amplitude, $K = E/\hbar c = 2\pi/\lambda$ is the length of the vacuum wave vector, λ is the vacuum wavelength of X-rays, and

$$\mathbb{V}(\mathbf{r}) = (\mathrm{grad}\,\mathrm{div} - K^2\chi(\mathbf{r})) \tag{2.5}$$

being the operator of the scattering potential.

2.1.2 Calculation of the scattered intensity

Solutions of Eq. (2.4) in vacuum, i.e., for $\mathbb{V} \equiv 0$, are plane waves [1]:

$$|\mathbf{K}\rangle = \mathrm{e}^{\mathrm{i}\mathbf{K}\cdot\mathbf{r}}. \tag{2.6}$$

The scattered intensity is measured as function of the directions of the incident $|\mathbf{K}_\mathrm{i}\rangle$ and detected waves $|\mathbf{K}_\mathrm{f}\rangle$. It is proportional to the *differential cross-section* $\frac{\partial\sigma}{\partial\Omega}$. The scattered intensity can not be calculated exactly in most cases. In order to solve Eq. (2.4), an appropriate approximation method has to be used, which is dependent on the structure of an investigated sample. Approximation methods used throughout the thesis are summarized in this sub-section.

[1] The time-dependent term $\exp(-\mathrm{i}\omega t)$ is omitted in all expressions throughout the thesis.

X-ray reflectivity

In case of X-ray reflectivity the intensity of radiation scattered under small scattering angles θ is measured. The scattered wavefield is influenced mainly by the zeroth Fourier component of the polarizability χ_0 and the scattering potential approximately reduces to $\mathbb{V}(\mathbf{r}) = -K^2\chi_0$. Solutions of Eq. (2.4) are again plane waves $|\mathbf{k}\rangle$ with wave vectors

$$k \equiv nK = K\sqrt{1+\chi_0} \approx K(1+\chi_0/2), \tag{2.7}$$

where n is the complex refractive index.

When a primary beam $|\mathbf{K}_\mathrm{i}\rangle$ hits a perfectly smooth surface of a semi-infinite sample under incidence angle α_i one reflected vacuum wave $|\mathbf{K}_\mathrm{r}\rangle$ and one transmitted wave[2] $|\mathbf{k}_\mathrm{t}\rangle$ arise. The following two relations for the z-components of the wave vectors $K_{\mathrm{r}\,z} = -K_{\mathrm{i}\,z}$ and

$$k_{\mathrm{t}\,z} = -\sqrt{K_{\mathrm{i}\,z}^2 + K^2\chi_0} \tag{2.8}$$

follow from the conservation of the in-plane components of the wave vectors and Eq. (2.7). Here $K_{\mathrm{i}\,z} = -K\sin\alpha_\mathrm{i}$ is the z-component of the wave vector of the primary wave and the $z-$axis is parallel to the outward normal of the sample surface. Since $\mathrm{Re}(\chi_0)$ is smaller than 0, total external reflection occurs for incidence angles below the critical angle α_c given by

$$\alpha_\mathrm{c} = \sqrt{-\mathrm{Re}(\chi_0)}, \tag{2.9}$$

and takes values in the range of tenth of a degree. The penetration depth of X-rays Λ is strongly reduced for $\alpha_\mathrm{i} < \alpha_\mathrm{c}$ (see Fig. 2.1). On the other hand, for values $\alpha_\mathrm{i} > \alpha_\mathrm{c}$,

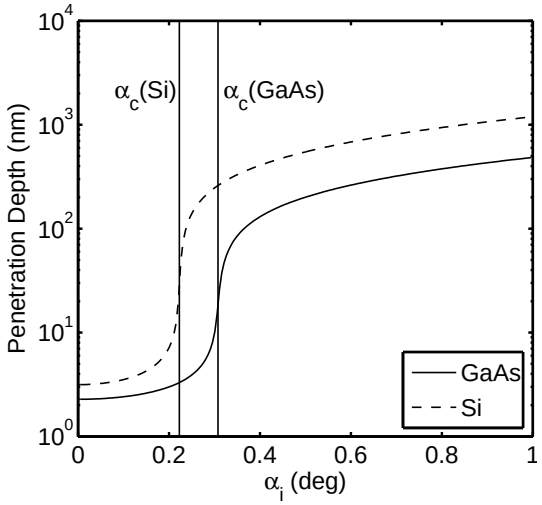

Figure 2.1. Penetration depth of X-rays at $\lambda = 1.54$ Å for GaAs and Si. α_c denotes the critical angle of the respective materials: $\alpha_\mathrm{c}(Si) = 0.22°$ and $\alpha_\mathrm{c}(GaAs) = 0.31°$.

[2]Here we denote wave vectors of waves within a media by small letters while vacuum wave vectors are denoted by capital letters.

the transmitted wave can enter the medium and is attenuated only by absorption. The penetration depth is given by

$$\Lambda = \frac{1}{2\,\mathrm{Im}(k_{\mathrm{t}\,z})} \tag{2.10}$$

The amplitudes of the electric field of X-rays in a planar multilayer are of interest. We introduce column vectors

$$\mathbf{E}_j(z) = \begin{pmatrix} E_j^{(\mathrm{t})}(z) \\ E_j^{(\mathrm{r})}(z) \end{pmatrix}, \tag{2.11}$$

where $E_j^{(\mathrm{t})}$ and $E_j^{(\mathrm{r})}$ are complex amplitudes of the transmitted and reflected wave, respectively, at a vertical position z in the jth layer (see Fig. 2.2). The amplitudes $\mathbf{E}_j(z)$ in

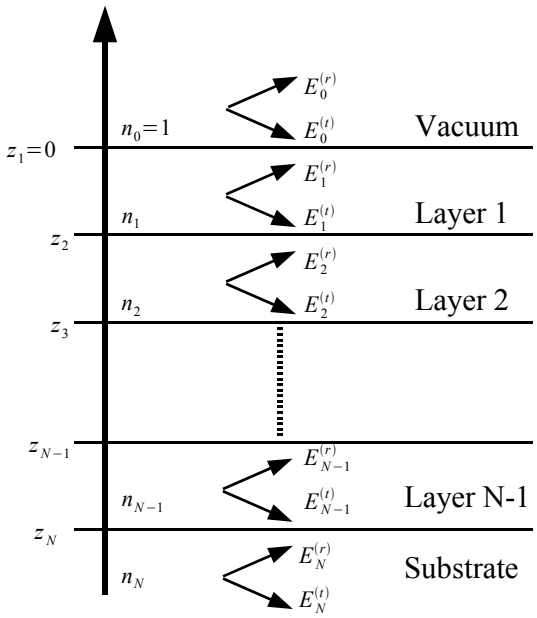

Figure 2.2. Sketch of a multilayer structure and the X-ray wavefield arising due to specular reflections of X-rays on the interfaces of the multilayer.

a multilayer with perfectly smooth interfaces can be expressed as

$$\begin{aligned} \mathbf{E}_j(z) = \hat{\phi}_j(z - z_{j+1})\hat{\mathbf{R}}_{j+1}\hat{\phi}_{j+1}(d_{j+1})\hat{\mathbf{R}}_{j+2}\hat{\phi}_{j+2}(d_{j+2})\hat{\mathbf{R}}_{j+3}\ldots \\ \ldots\hat{\phi}_{N-1}(d_{N-1})\hat{\mathbf{R}}_N\mathbf{E}_{\mathrm{Sub}} = \hat{\mathbf{M}}^{(j)}(z)\mathbf{E}_{\mathrm{Sub}} \end{aligned} \tag{2.12}$$

where

$$\hat{\mathbf{R}}_l = \frac{1}{t_l}\begin{pmatrix} 1 & r_l \\ r_l & 1 \end{pmatrix},\ \hat{\phi}_l(\Delta z) = \begin{pmatrix} \exp(\mathrm{i}k_{z\,l}\Delta z) & 0 \\ 0 & \exp(-\mathrm{i}k_{z\,l}\Delta z) \end{pmatrix}, \tag{2.13}$$

$k_{z\,l}$ is the vertical component of the wave vector of the transmitted wave in the lth layer [see Eq. (2.8)], d_l is the thickness of the lth layer, $\mathbf{K}_{\|}$ is the in-plane component of the wave vector, $\mathbf{E}_{\mathrm{Sub}}$ are amplitudes of the electric field on the top of the substrate, and we have denoted by

$$t_l = \frac{2k_{z\,(l-1)}}{k_{z\,(l-1)} + k_{z\,l}} \text{ and } r_l = \frac{k_{z\,(l-1)} - k_{z\,l}}{k_{z\,(l-1)} + k_{z\,l}} \tag{2.14}$$

the Fresnel complex transmittivity and reflectivity, respectively, of the interface between the $(l-1)$st and lth layer.

We assume that there is no reflected wave in the substrate since it is usually very thick. Then Eq. (2.12) reduces to

$$E_j^{(\mathrm{t})}(z) = \frac{M_{1\,1}^{(j)}(z)}{M_{1\,1}^{(0)}(0)} \quad \text{and} \tag{2.15a}$$

$$E_j^{(\mathrm{r})}(z) = \frac{M_{2\,1}^{(j)}(z)}{M_{1\,1}^{(0)}(0)}, \tag{2.15b}$$

where we have introduced a normalization factor $\hat{\mathbf{M}}_{1\,1}^{(0)}(0)$ to ensure that the amplitude of the primary wave in the origin is unity, i.e., $\mathbf{E}_t(0) = 1$. The specular reflectivity of the multilayer stack is then given by

$$\mathcal{R} = \left| \frac{M_{2\,1}^{(0)}(0)}{M_{1\,1}^{(0)}(0)} \right|^2 . \tag{2.16}$$

Equations (2.15) and (2.16) are valid for both s- and p-polarizations in the approximation of small scattering angles.

For real interfaces with a finite root mean square roughness σ, the intensities of the specularly reflected wave and of the transmitted wave are weakened. The specular beam averages over the lateral structure of the roughness disregarding its lateral correlation properties. This averaging is mostly treated as being Gaussian. Reflectivity is then calculated by Eq. (2.16), where one introduces modified reflection and refraction coefficients [see Eq. (2.14)]

$$r_l' = r_l \mathrm{e}^{-2k_{z\,(l-1)}k_{z\,l}\sigma_l^2} \text{ and } t_l' = t_l \mathrm{e}^{(k_{z\,(l-1)}-k_{z\,l})^2\sigma_l^2/2} \tag{2.17}$$

σ_l is the roughness of the interface between the $(l-1)$st and the lth layer.

Kinematical and Fraunhofer approximation

The kinematical approximation is appropriate for simulations of measured diffuse scattering if the scattering from nanostructures and their close neighbourhood dominates over the scattering from other features in a sample. Then multiple scattering can be neglected and the total scattered amplitude is approximately given by

$$E(\mathbf{r}) = K^2 E_0 C \int_V \mathrm{d}^3\mathbf{r}' \chi(\mathbf{r}') \mathrm{e}^{\mathrm{i}\mathbf{K}_i\cdot\mathbf{r}'} G_0(\mathbf{r}-\mathbf{r}'), \tag{2.18}$$

where

$$G_0(\mathbf{r}-\mathbf{r}') = -\frac{1}{4\pi}\frac{\exp(\mathrm{i}K|\mathbf{r}-\mathbf{r}'|)}{|\mathbf{r}-\mathbf{r}'|} \tag{2.19}$$

is the Green's function of equation (2.4).

$$C = \begin{cases} 1 & \text{s-polarization} \\ |\cos(2\theta)| & \text{p-polarization} \end{cases} \tag{2.20}$$

is the polarization factor and depends on the scattering geometry. In the s- and p-polarizations, the incoming electric field vector is perpendicular and parallel, respectively, to the scattering plane. 2θ is the angle between the incident and scattered waves. The integration in Eq. (2.18) is performed over the sample volume V.

The Fraunhofer approximation can be introduced, if the coherently illuminated volume of the sample is smaller than the diameter of the first Fresnel zone $d = 2\sqrt{|\mathbf{r}|\lambda/2}$ and the sample to detector distance $|\mathbf{r}|$ is much larger than the sample size,[3] i.e., $\max(|\mathbf{r}'|) \ll |\mathbf{r}|$. Then the term in the exponent of Eq. (2.19) can be approximated as $K|\mathbf{r}-\mathbf{r}'| \approx Kr - \mathbf{K}_s \cdot \mathbf{r}'$, where $\mathbf{K}_s = K\mathbf{r}/r$. Equation (2.18) then simplifies to the Fourier transform of $\chi(\mathbf{r})$

$$E(\mathbf{r}) = -\frac{K^2}{4\pi}\frac{E_0 C}{|\mathbf{r}|}\mathrm{e}^{\mathrm{i}K|\mathbf{r}|}\int_V \mathrm{d}^3\mathbf{r}'\mathrm{e}^{-\mathrm{i}(\mathbf{K}_s-\mathbf{K}_i)\mathbf{r}'}\chi(\mathbf{r}). \tag{2.21}$$

In common laboratory experimental arrangements, the diameter of the first Fresnel zone is typically several μm. It is usually larger than the size of islands and their coherently deformed surrounding. The Fraunhofer approximation can be applied in this case. However, for laterally large samples, like perfect single crystals and thin layers, the Fraunhofer approximation is usually not valid. In these cases the scattered wavefield can be assumed to be homogeneous. The intensity of the scattered wave does not depend on the position $\mathbf{r}$ of the observer and can be expressed as a superposition of contributions of all plane-wave components constituting the homogeneous wave [HPB99].

Lattice deformation due to the misfit strain between the NI lattice and the substrate lattice gives rise to diffuse scattering in the vicinity of substrate Bragg peaks $\mathbf{h} \neq 0$. Polarizability of the deformed lattice is $\chi_{\mathrm{deformed}}(\mathbf{r}) = \chi_{\mathrm{undeformed}}(\mathbf{r}-\mathbf{u}_{\mathrm{at}}(\mathbf{r}))$, where $\mathbf{u}_{\mathrm{at}}(\mathbf{r})$ is the displacement field of atoms. Usually, only displacements of whole unit cells are taken into account and the displacements of individual atoms is neglected for calculations of the diffuse scattering. Equation (2.3) is then modified as follows:

$$\chi_{\mathrm{deformed}}(\mathbf{r}) \approx \sum_{\mathbf{g}} \chi_{\mathbf{g}\ \mathrm{undeformed}}\mathrm{e}^{\mathrm{i}\mathbf{g}\cdot(\mathbf{r}-\mathbf{u}(\mathbf{r}))}. \tag{2.22}$$

The displacement field $\mathbf{u}(\mathbf{r})$ for purposes of X-ray scattering simulations is mostly calculated by solving equations of linear elasticity via either analytical or numerical methods (for a review see Ref. [SHB04]).

Additionally, fluctuations of the chemical composition due to the presence of NIs material lead to local change of the polarizability $\chi_{\mathbf{g}\ \mathrm{undeformed}}$. To take this fact into account we split the real polarizability of a unit cell at position $\mathbf{r}$ into the polarizability of the substrate or the matrix surrounding the nanostructure[4] $\chi_{\mathbf{g}}^{(\mathrm{s})}$ and a perturbation $\Delta\chi_{\mathbf{g}}(\mathbf{r})$

$$\chi_{\mathrm{deformed}}(\mathbf{r}) \approx \sum_{\mathbf{g}} (\chi_{\mathbf{g}}^{(\mathrm{s})} + \Delta\chi_{\mathbf{g}})\mathrm{e}^{\mathrm{i}\mathbf{g}\cdot(\mathbf{r}-\mathbf{u}(\mathbf{r}))}. \tag{2.23}$$

[3] Here we assume that the origin of the coordinates is chosen within the sample.

[4] We write $\chi_{\mathbf{g}}$ instead of $\chi_{\mathbf{g}\ \mathrm{undeformed}}$ in the rest of the thesis.

A measurement of the diffusely scattered intensity is performed in the vicinity of a certain reciprocal space point $\mathbf{h}$. When we substitute Eq. (2.23) for $\chi(\mathbf{r})$ into Eq. (2.21), only one term $(\chi_{\mathbf{h}}^{(\mathrm{s})} + \Delta\chi_{\mathbf{h}}) \exp(\mathrm{i}\mathbf{h} \cdot (\mathbf{r} - \mathbf{u}(\mathbf{r})))$ contributes predominantly to the integral. Thus, Eq. (2.21) can be simplified to

$$E(\mathbf{r}) \approx -\frac{K^2}{4\pi} \frac{E_0 C}{|\mathbf{r}|} \mathrm{e}^{\mathrm{i}K|\mathbf{r}|} \int_V \mathrm{d}^3\mathbf{r}' \mathrm{e}^{-\mathrm{i}[(\mathbf{Q}-\mathbf{h})\cdot\mathbf{r}' + \mathbf{h}\cdot\mathbf{u}(\mathbf{r}')]} (\chi_{\mathbf{h}}^{(\mathrm{s})} + \Delta\chi_{\mathbf{h}}(\mathbf{r}')), \tag{2.24}$$

where $\mathbf{Q} = \mathbf{K}_s - \mathbf{K}_i$ is the scattering vector. When the measurement is performed in the vicinity of the origin of the reciprocal space, i.e., in the vicinity of $\mathbf{h} = 0$, Eq. (2.24) reduces to the Fourier transform from $\Delta\chi_0(\mathbf{r}')$. Thus, the measurement is sensitive to the chemical composition only and not to the strain fields.

Distorted Wave Born Approximation

Distorted Wave Born Approximation (DWBA) is appropriate if the relatively weak scattering from nanostructures is superimposed with a signal from strongly scattering features in the sample. DWBA can be applied if the scattering potential can be divided into two parts $\mathbb{V} = \mathbb{V}_A + \mathbb{V}_B$. $\mathbb{V}_A$ is the potential of the strongly scattering features for which an exact solution E_A of the scattering problem can be obtained. The second term $\mathbb{V}_B$ can then be regarded as a (small) perturbation of $\mathbb{V}_A$. Typically, $\mathbb{V}_A$ describes specular reflections on planar interfaces in a sample and/or diffraction on the substrate lattice while $\mathbb{V}_B$ corresponds to the scattering on the nanostructures.

Let us denote $E_A^{(1,2)}$ two independent solutions of Eq. (2.4) for the unperturbed potential $\mathbb{V}_A$, where $E_A^{(1)}$ describes the wavefield excited by the incident wave $|\mathbf{K}_i\rangle$, and the time-inverted solution $E_A^{(2)}$ corresponds to the wavefield, which would be excited by the time-inverted wave $|\mathbf{K}_f\rangle$. $|\mathbf{K}_f\rangle$ denotes the detected outgoing wave. The differential scattering cross section can then be expressed as

$$\frac{\partial\sigma}{\partial\Omega} = \frac{1}{16\pi^2} \left| \left\langle E_A^{(2)} \left| \mathbb{V}_A \right| \mathbf{K}_i \right\rangle + \left\langle E_A^{(2)} \left| \mathbb{V}_B \right| E_A^{(1)} \right\rangle \right|^2. \tag{2.25}$$

Multiple scattering processes due to $\mathbb{V}_B$ are neglected, which is justified if the perturbing potential is small compared to $\mathbb{V}_A$.

For small-angle scattering on buried islands, which is sensitive only to the difference of the refractive index between islands and the surrounding matrix material $\Delta\chi_0$, a proper choice of the potentials is as follows. $\mathbb{V}_A$ is scattering potential of a semiinfinite substrate and contains only the polarizability of the matrix $\chi_0^{(\mathrm{m})}$. The perturbation potential is then

$$\mathbb{V}_B = -K^2 \Delta\chi_0 \Omega(\mathbf{r}), \tag{2.26}$$

where $\Omega(\mathbf{r})$ is the shape function of the island.

For X-ray and grazing-incidence diffraction with the diffraction vector $\mathbf{g} = \mathbf{h}$, a semiinfinite crystalline substrate can be chosen as the non-disturbed system. The solution of

the non-disturbed wave equation can be found using the two beam approximation of the dynamical X-ray theory [HPB99]. The perturbation potential $\mathbb{V}_B$ is expressed by

$$\mathbb{V}_B = -K^2[\Delta\chi_{\mathbf{h}}\Omega(\mathbf{r})\mathrm{e}^{-\mathrm{i}\mathbf{h}\cdot\mathbf{u}(\mathbf{r})} + \chi_{\mathbf{h}}^{(\mathrm{m})}(\mathrm{e}^{-\mathrm{i}\mathbf{h}\cdot\mathbf{u}(\mathbf{r})} - 1)]\mathrm{e}^{\mathrm{i}\mathbf{h}\cdot\mathbf{r}}, \tag{2.27}$$

where $\Delta\chi_{\mathbf{h}}$ is the difference of the $\mathbf{h}$-th Fourier component of the polarizability of the islands and that of the substrate $\chi_{\mathbf{h}}^{(\mathrm{m})}$, $\mathbf{u}(\mathbf{r})$ is the displacement field in point $\mathbf{r}$ due to the islands.

In most cases, the scattering potential $\mathbb{V}_B$ is random due to the random distribution of NIs. In this case the differential cross-section, Eq. (2.25), can be divided into the coherent and diffuse (incoherent) parts. The diffuse part is used in the following chapters for characterization of NIs and it is expressed by

$$\left(\frac{\partial\sigma}{\partial\Omega}\right)_{\mathrm{incoh}} = \frac{1}{16\pi^2}\,\mathrm{Cov}\left(\left\langle E_A^{(2)}\left|\mathbb{V}_B\right|E_A^{(1)}\right\rangle, \left\langle E_A^{(2)}\left|\mathbb{V}_B\right|E_A^{(1)}\right\rangle\right), \tag{2.28}$$

where the operator $\mathrm{Cov}(T,T) = \langle TT^\star\rangle - \langle T\rangle\langle T\rangle^\star$ is the covariance, the brackets $\langle\cdots\rangle$ in Cov denote statistical averaging, and the star * denotes the complex conjugation.

Island position correlation

If nano-island positions are random and the islands have approximately identical shape and size, the scattered intensity is in a good approximation proportional to the scattering from a single island. However, the positions of the islands can be correlated, resulting in a significant interference of the diffusely scattered waves from the individual islands. Depending on the strength of the position correlation, this can lead to more or less pronounced and sharp satellite peaks in the diffuse scattering. The distances between the nearest neighbour satellite peaks in reciprocal space Δq are approximately related to the mean nearest neighbour island to island distance $\langle d\rangle$ in real space via

$$\Delta q \approx \frac{2\pi}{\langle d\rangle}. \tag{2.29}$$

In the framework of the kinematical theory, the amplitude of the diffuse scattering from an ensemble of nano-islands can be treated as a coherent sum of the amplitude contributions $E_m^{\mathrm{diffuse}}(\mathbf{q})$ from islands at positions $\mathbf{R}_m$. This approximation is valid as long as the distances between the islands are significantly larger than their size. In this case we can write the following for the amplitude of the wave scattered by the whole island ensemble:

$$E_{\mathrm{ensemble}}^{\mathrm{diffuse}}(\mathbf{q}) = \sum_m E_m^{\mathrm{diffuse}}(\mathbf{q})\mathrm{e}^{\mathrm{i}\mathbf{q}\cdot\mathbf{R}_m}. \tag{2.30}$$

For practical reasons, we can extract only average information on the size, shape and chemical composition of the islands. Extracting this structural information is only possible

if all islands are sufficiently similar and the island structure is not correlated with their positions. In this case, Eq. (2.30) can be approximated by

$$E^{\text{diffuse}}_{\text{ensemble}}(\mathbf{q}) \approx \sqrt{\langle |E^{\text{diffuse}}_m(\mathbf{q})|^2 \rangle_{\text{structure}}} \sum_m \mathrm{e}^{\mathrm{i}\mathbf{q}\cdot\mathbf{R}_m}, \tag{2.31}$$

where the brackets $\langle \cdots \rangle_{\text{structure}}$ denote averaging over all possible combinations of the structural properties of the islands. The total diffuse intensity is then

$$\left(\frac{\mathrm{d}\sigma(\mathbf{q})}{\mathrm{d}\Omega}\right)_{\text{ensemble}} \approx \left\langle \frac{\mathrm{d}\sigma(\mathbf{q})}{\mathrm{d}\Omega} \right\rangle_{\text{structure}} P(\mathbf{q}), \text{ where} \tag{2.32}$$

$$P(\mathbf{q}) = \left\langle \sum_{m,n} \mathrm{e}^{\mathrm{i}\mathbf{q}(\mathbf{R}_m - \mathbf{R}_n)} \right\rangle_{\text{position}} \tag{2.33}$$

is the interference function, the brackets $\langle \cdots \rangle_{\text{position}}$ denote averaging over all possible island spatial distributions of the entire ensemble of scattering islands, and $\langle \mathrm{d}\sigma(\mathbf{q})/\mathrm{d}\Omega \rangle_{\text{structure}}$ is the average differential cross-section of a single island.

2.2 Scattering geometries

For characterization of nano-islands we used angular dispersive methods, where the intensity of the diffuse scattering is measured as a function of the direction of the incoming X-ray beam $|\mathbf{K}_i\rangle$ and the detected wave $|\mathbf{K}_f\rangle$. The intensity distribution is usually plotted as a function of the scattering vector[5] $\mathbf{Q} = \mathbf{K}_f - \mathbf{K}_i$ in reciprocal space maps (RSMs).

The maximal length of the scattering vector is $\max(Q) = 2K = \frac{4\pi}{\lambda}$. The accessible part of the reciprocal space is therefore restricted to the volume inside a hemisphere of radius $2K = \frac{4\pi}{\lambda}$, which is called extended Ewald sphere (see Fig. 2.3). Since substrates of the studied samples are mostly thick, all X-rays are absorbed on the path through the samples and there is no transmitted beam. Thus, only reflection geometry can be used and the accessible volume of the reciprocal space is further limited to the region outside hemispheres of radius $K = \frac{2\pi}{\lambda}$, the so called Laue zones. Transmission takes place for $\mathbf{Q}$ inside the Laue zones.

Choosing a proper scattering geometry, i.e., a proper region in the accessible part of the reciprocal space in Fig. 2.3, one can tune the penetration depth of X-rays so that information is gained about the near surface structures or about the more deeply buried ones. Additionally, a measurement can be sensitive to variations of the electron density averaged over unit cell volumes, i.e., to the chemical composition, or both to the average electron density and to the strain field distribution, when the measurement is performed in the vicinity of reciprocal space points $\mathbf{h} = 0$ or $\mathbf{h} \neq 0$, respectively.

[5]The reduced scattering vector $\mathbf{q} = \mathbf{K}_f - \mathbf{K}_i - \mathbf{h} = \mathbf{Q} - \mathbf{h}$ is often introduced for convenience.

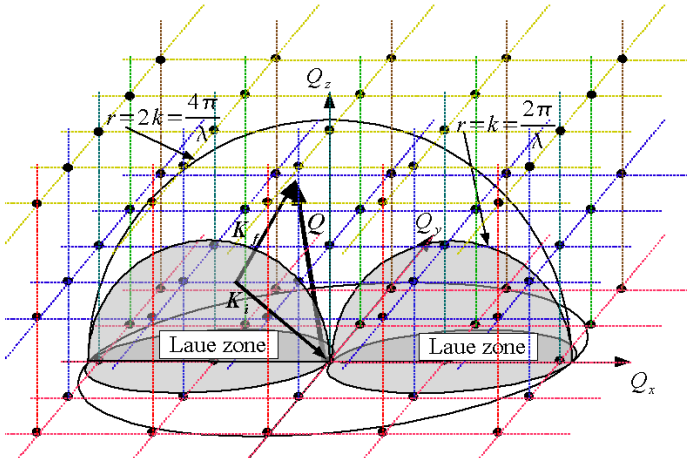

Figure 2.3. The reciprocal space is probed in the vicinity of the substrate reciprocal space points (black dots) by varying the directions of the incoming and outgoing waves, $\mathbf{K}_i$ and $\mathbf{K}_f$, respectively. The accessible part of reciprocal space is restricted to the volume inside the extended Ewald sphere, i.e., a hemisphere of radius $\frac{4\pi}{\lambda}$, and outside the Laue zones, i.e., two hemispheres of radius $\frac{2\pi}{\lambda}$. The base planes of the hemispheres are parallel to the sample surface. The centres of the Laue zones lies on the Q_x axis, which is defined as the intersection of the sample surface and the plane containing vector $\mathbf{K}_i$ and the sample surface normal.

X-ray reflectometry

In X-ray reflectometry, the scattering plane is perpendicular to the sample surface and only the vicinity of the origin of the reciprocal space $\mathbf{h} = 0$ is probed (see Fig. 2.4). The method is sensitive purely to the modulations of the 0th order component of the polarizability $\chi_0(\mathbf{r})$, i.e., to the modulations of the electron density averaged over unit cell volumes. Thus, if there is a difference between electron densities of the components of a sample, X-ray reflectometry provides information on the spatial material distribution.

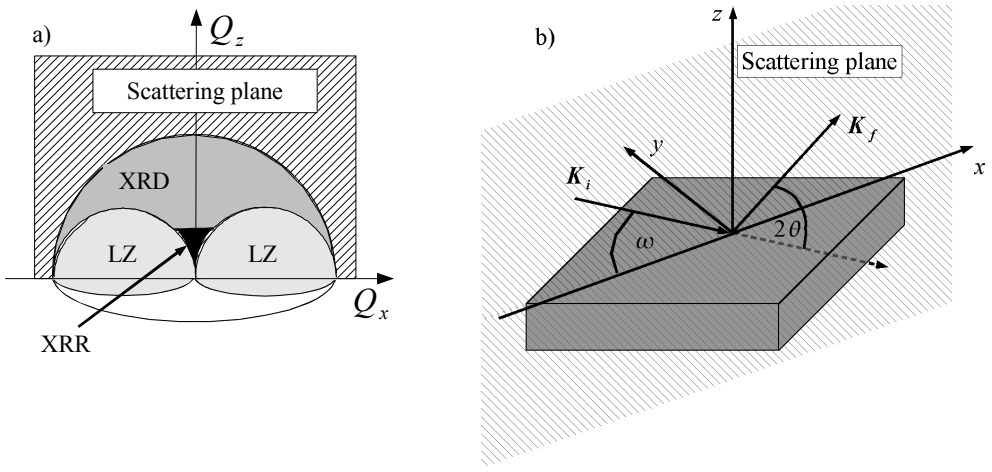

Figure 2.4. a) Sub-volume of the reciprocal space accessible by X-ray reflectometry (XRR) and coplanar X-ray diffraction (XRD). LZ denotes Laue zones. b) Coplanar scattering geometry for XRR and XRD in direct space. ω denotes incidence angle and 2θ is the scattering angle.

The specularly reflected beam fulfils the condition $\omega = \theta$ and the specular scan runs along the Q_z axis, i.e., along the truncation rod. Specular reflectivity measurements are used for characterization of multilayers. It provides information on the composition of layers and the roughness of interfaces. Rough interfaces give rise to diffuse scattering, which provides information on lateral and vertical correlation of the interfacial roughness.

If small length scale modulations of $\chi_0(\mathbf{r})$ along a plane parallel to the sample surface are studied, the necessary range in Q_x direction can be obtained only for sufficiently high values of Q_z due to the Laue zones. In this case, it is better to use grazing-incidence small-angle scattering geometry, where the intensity distribution is measured along the Q_y axis for fixed incidence and exit angles (see [HPB99, Sch04]).

Since the scattering is measured only in the plane perpendicular to the sample surface, only two components of the scattering vector are used to describe the intensity distribution in the reciprocal space. The relations between the reciprocal space coordinates and the incidence and scattering angles ω and 2θ, respectively, are:

$$Q_x = 2K \sin\theta \sin(\omega - \theta) \tag{2.34a}$$

$$Q_z = 2K \sin\theta \cos(\omega - \theta). \tag{2.34b}$$

Coplanar X-ray diffraction

In coplanar X-ray diffraction (XRD), the scattered intensity is measured in the vicinity of reciprocal space points $\mathbf{h} \neq 0$ within the plane perpendicular to the sample surface (see Fig. 2.4). The intensity distribution in XRD is influenced by both the chemical composition and the lattice deformation. However, one has to differentiate between measurements in the vicinity of symmetrical reflections, where the reciprocal space point $\mathbf{h}$ lies on the Q_z-axis perpendicular to the sample surface, and asymmetrical reflections, where $\mathbf{h}$ lies outside the Q_z-axis. From a symmetrical reflection, information can be obtained about lattice strains in the vertical direction only. The intensity distribution along the Q_x axis is purely influenced by shape, possible lateral correlations, and local lattice tilts. For an asymmetrical reflection, a discrimination into strain and shape effects is not possible anymore. The reciprocal space coordinates obey again Eq. (2.34).

Since the incidence angles are usually much larger than the critical angle, X-rays penetrate deep into the sample. Thus XRD is an ideal tool for the characterization of deeply buried islands and island multilayers.

Grazing incidence X-ray diffraction

In the grazing-incidence X-ray diffraction (GID) geometry (see Fig. 2.5, the diffraction process takes place at lattice planes perpendicular to the sample surface and the scattering plane is nearly parallel to the sample surface. In the measurements presented in this thesis we used a position sensitive detector in the arrangement shown in Fig. 2.5 for detection of the scattered intensity. Position sensitive detector records simultaneously the intensity distribution as a function of exit angle α_f. Reflections of X-rays at the sample

surface are significant since the angles of incidence and exit, $\alpha_{i,f}$, are small. Total external reflection occurs below a critical glancing angle α_c, and the penetration depth shrinks to a few nanometers (see Fig. 2.1). Slightly above the critical angle, the penetration depth increases by a factor of 10^2 nm. This allows for tuning of the information depth in ranges from several nm to thousands of nm.

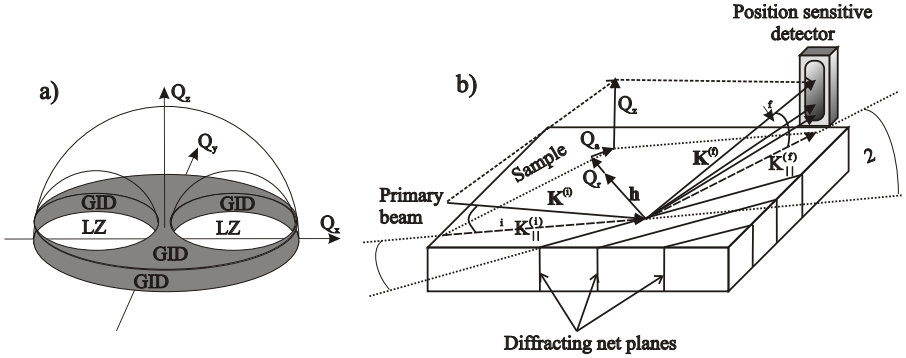

Figure 2.5. a) Sub-volume of the reciprocal space accessible in a grazing-incidence diffraction (GID) experiment. LZ denotes Laue zones. b) A sketch of an experiment in GID geometry in direct space. The scattered intensity is measured in the vicinity of an in-plane reciprocal space point $\mathbf{h}$. α_i and α_f denote angle of incidence and exit, respectively, 2θ is the scattering angle in the plane of the sample surface and ω is the angle between $\mathbf{K}_\parallel^{(\mathrm{i})}$ and the diffracting net planes. $\mathbf{K}_\parallel^{(\mathrm{i})}$ and $\mathbf{K}_\parallel^{(\mathrm{f})}$ are the projections of the wave vectors of the primary and scattered wave, respectively. The in-plane components of the scattering vector $\mathbf{Q}_\parallel = \mathbf{K}_\parallel^{(\mathrm{f})} - \mathbf{K}_\parallel^{(\mathrm{i})}$ are referred to as radial Q_r and angular Q_a components.

In GID, one usually uses a reciprocal space coordinate system $(Q_\mathrm{a}, Q_\mathrm{r}, Q_z)$ connected to the reciprocal space vector $\mathbf{h}$, around which the measurement is performed. Here, Q_r is the distance from the origin of the reciprocal space in the direction of the $\mathbf{h}-$vector, the so called radial direction. Q_a is the in-plane component of the $\mathbf{Q}$ perpendicular to $\mathbf{h}$, i.e., the in-plane distance from the radial axis. The relations between the goniometer angles $\alpha_{i,\,f}, \omega, 2\theta$, and the reciprocal space coordinates are

$$Q_\mathrm{r} = K(\cos\alpha_\mathrm{f}\sin(2\theta-\omega) + \cos\alpha_\mathrm{i}\sin\omega) \tag{2.35a}$$

$$Q_\mathrm{a} = K(\cos\alpha_\mathrm{f}\cos(2\theta-\omega) - \cos\alpha_\mathrm{i}\cos\omega) \tag{2.35b}$$

$$Q_z = K(\sin\alpha_\mathrm{f} + \cos\alpha_\mathrm{i}). \tag{2.35c}$$

In the limit of small incidence and exit angles $\alpha_{\mathrm{i,\,f}} \ll 1$ rad and small deviations from the radial axis $|\omega - \theta| \ll 1$ rad, Eq. (2.35) reduces to

$$Q_\mathrm{r} \approx 2K\sin\theta\cos(\omega-\theta) \approx 2K\sin\theta \tag{2.36a}$$

$$Q_\mathrm{a} \approx 2K\sin\theta\sin(\omega-\theta) \approx Q_\mathrm{r}\sin(\omega-\theta) \tag{2.36b}$$

$$Q_z \approx K(\alpha_f + \alpha_i). \tag{2.36c}$$

The diffuse scattering is influenced by the displacement field $\mathbf{u}(\mathbf{r})$ via the term $\mathrm{e}^{-\mathrm{i}\mathbf{u}(\mathbf{r})\cdot\mathbf{h}}$ [see Eqs. (2.24) and (2.27)]. Therefore, the diffuse scattering is influenced only by the lattice strains parallel to the radial direction, i.e., only by the in-plane strains. This is in contrast to XRD, where the measured intensity is sensitive to the vertical strain as well. Scans along the radial (Q_r) and angular (Q_a) directions are sensitive to the strain and to the shape of the nanostructures, respectively.

In practise, the radial and angular scans are performed by the movement of the goniometer motors in coupled $\omega = 2\theta/2$ mode and by a movement of the ω-motor at a fixed detector position 2θ, respectively.

2.3 Iso-strain scattering method for uncapped nano-islands

Basically, two approaches are used for the evaluation of X-ray data. First, in indirect methods the shape and the chemical composition of a model NI are fitted to obtain a satisfactory agreement between the experimental data and simulations (e.g., in Refs. [SHH$^+$03, HSH$^+$02, WSH$^+$00, DSH$^+$97]). Secondly, the iso-strain scattering method (ISSM), which was introduced in [KML$^+$01, KML$^+$00, KMF$^+$99] and successfully applied, e.g., in Refs. [KMF$^+$99, KML$^+$00, KML$^+$01, SSC$^+$02, MPMRM$^+$02, MKMR$^+$03, HLH$^+$03, SSZ$^+$03, MMPKC04], [SSH$^+$05, KMR$^+$05], allows for a direct structural characterization of *uncapped* NIs without demanding strain field calculations.

The ISSM for uncapped NIs is based on measurements in GID (see Fig. 2.5. Reciprocal space scans are measured along the q_a (angular scans) and q_z directions for various values of q_r. Such scans taken at a certain position $q_\mathrm{r} = q_{\mathrm{r}0}$ probe X-rays dominantly scattered from a certain sub-volume of NIs with an in-plane lattice parameter $a_\parallel = 2\pi/(q_{\mathrm{r}0} + |\mathbf{h}|)\sqrt{h^2+k^2+l^2}$. This is a volume of constant in-plane strain, a so-called iso-strain volume (ISV) (see [KML$^+$01]). The lateral strain with respect to the substrate is $\epsilon_{\parallel 0} = (a_\parallel - a_\mathrm{sub})/a_\mathrm{sub} = -q_{\mathrm{r}0}/|\mathbf{h}|$. The corresponding ISV can be characterized using q_a and q_z scans if the following conditions are fulfilled: (i) the probed ISV has to spread along a section along the growth direction, which is small compared to the NIs height h_NI. (ii) The change of the island radius along this section must be small as well. (iii) The radius of the ISV $r(z_0)$ has to be sufficiently large, since the finite size of the ISV results in the broadening of the Bragg reflection along the q_r direction $\Delta q_\mathrm{r} = 2\pi/r(z_0)$. (iv) The strain gradient along the vertical axis $\mathrm{d}\epsilon_\parallel(z)/\mathrm{d}z\big|_{z=z_0}$ has to be sufficiently large. As an estimate, ISS can be applied if the condition

$$r(z)\left|\frac{\mathrm{d}\epsilon_\parallel(z)}{\mathrm{d}z}\right|\Bigg|_{z=z_0} |\mathbf{h}|\cdot h_\mathrm{NI} \gg 1 \tag{2.37}$$

is fulfilled [KML$^+$01], for a ISV at the vertical position z_0.

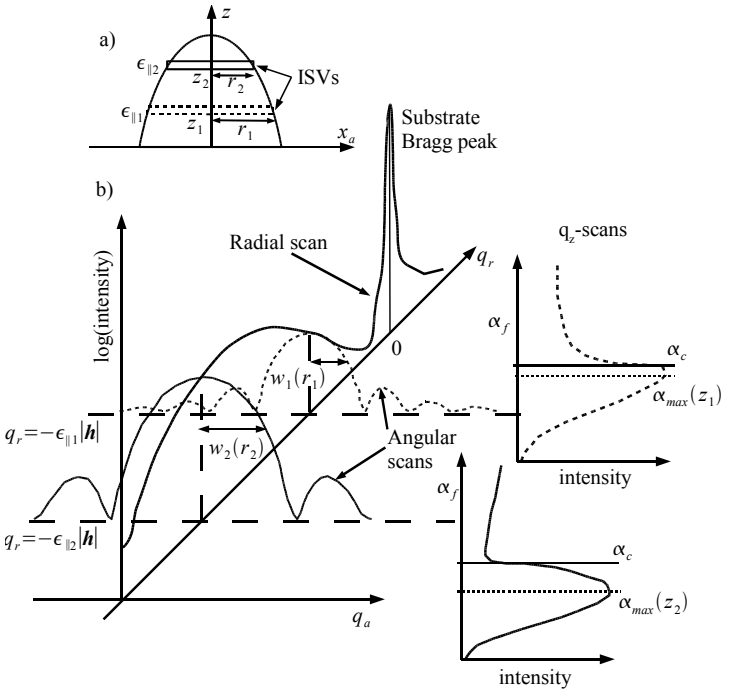

Figure 2.6. Principle of the iso-strain scattering method. a) The model of nano-islands (NIs) for ISSM. The NI is represented by a stack of iso-strain volumes (ISVs). Each ISV is characterized by its strain with respect to the substrate $\epsilon_{\|i}$, radius r_i, vertical position z_i, and content of the island material x_i. b) The radius and the vertical position of a ISV i is extracted from the angular and q_z scans, respectively, measured at the radial position $q_{ri} = -|\mathbf{h}|\epsilon_{\|i}$. For details see text.

Lateral sizes of the ISVs

The lateral size of the selected ISV is deduced from a fit of the intensity distribution along the angular direction (see Fig. 2.6), which is in the kinematical approximation given by

$$I(q_\mathrm{r} = -|\mathbf{h}|\epsilon_{\|i}, q_a) \propto \left| \int \mathrm{d}\mathbf{r}\Omega_i(\mathbf{r}) \exp(-\mathrm{i}q_\mathrm{a}x_\mathrm{a}) \right|^2 , \tag{2.38}$$

where x_a is the component of the direct space vector $\mathbf{r}$ along the q_a-axis and Ω_i is the shape function of the ISV i. The width of of the scattering pattern in reciprocal space is inversely proportional to the lateral size of the ISV. For rotationally symmetric NIs Eq. (2.38) reduces to

$$I(q_\mathrm{r} = -|\mathbf{h}|\epsilon_{\|i}, q_\mathrm{a}) \propto \left| r_i \frac{J_1(q_\mathrm{a}r_i)}{q_\mathrm{a}} \right|^2 , \tag{2.39}$$

where $J_1(x)$ is the Bessel function of the first order and r_i is the radius of the ISV. If ISVs have rectangular projections to the sample surface plane with one side of the rectangle along the $q_\mathrm{a}-$axis we obtain

$$I(q_\mathrm{r} = -|\mathbf{h}|\epsilon_{\|i}, q_\mathrm{a}) \propto \left| \frac{\sin(q_\mathrm{a}D_i/2)}{q_\mathrm{a}} \right|^2 . \tag{2.40}$$

Here, D_i is the length of the rectangle side along $q_\mathrm{a}-$axis.

ISV elevation above the sample surface

From fitting of the q_z-intensity profiles one obtains the elevation z_i of the selected ISV above the sample surface. The intensity distribution along the q_z-axis is described by the

coherent superposition of waves resulting from four scattering processes of the first order perturbation theory (see Fig. 2.7): (i) direct Bragg reflection of the primary wave at the ISV selected by the momentum transfer $q_{\mathrm{r}i}$, (ii) the specular reflection at a grazing angle of α_{i} at the free sample surface between NIs takes place before the Bragg reflection at the ISV, (iii) the specular reflection at grazing angle of α_{f} takes place after the Bragg reflection at the ISV, and (iv) combines the specular reflections of the processes (ii) and (iii) before and after the Bragg reflection, respectively. The approximative formula for the scattered intensity distribution is then

$$I(q_{\mathrm{z}}, z_i) \propto \left|t(\alpha_{\mathrm{i}}, z_i)t(\alpha_{\mathrm{f}}, z_i)\right|^2 \quad \text{where} \tag{2.41a}$$

$$t(\alpha, z) \propto 1 + r(\alpha)e^{\mathrm{i}2K\alpha z}, \tag{2.41b}$$

$r(\alpha)$ is the Fresnel complex reflectivity [see Eq. (2.14)] at the interface air/substrate, and $q_{\mathrm{z}} \approx -K(\alpha_{\mathrm{i}} + \alpha_{\mathrm{f}})$ is the vertical component of the wave vector transfer. The q_{z}-intensity profiles are usually measured as a function of α_{f} (see Fig. 2.6) using a position sensitive detector for a fixed incidence angle α_{i} [as shown in Fig. 2.5(b)]. The intensity distribution exhibits a characteristic maximum. The α_{f} position of the maxima decreases with increasing z_i, which can be approximately determined from the equation

$$z_i = \frac{1}{K\alpha_{\max}} \arccos \frac{\alpha_{\max}}{\alpha_{\mathrm{c}}}. \tag{2.42}$$

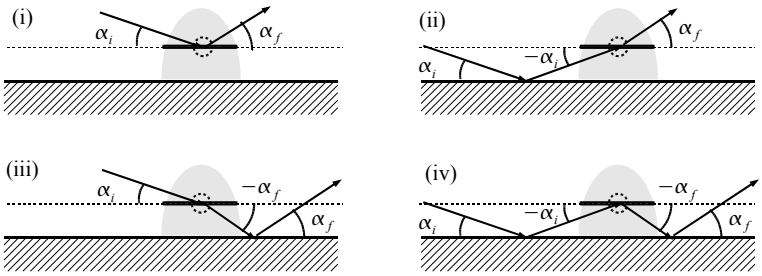

Figure 2.7. Four scattering processes from the first order perturbation theory (sideview). Coherent superposition of the resulting outgoing waves explains the intensity distribution along the q_{z}-axis in an iso-strain scattering experiment. Dashed circle denotes direct Bragg reflection at the iso-strain volume selected by q_{r}. For details see text.

Chemical composition

For III-V zinc-blend compounds (i.g., InAs, GaAs), information on the chemical composition of the selected ISV i is obtained from the intensity measurements at radial position $q_{\mathrm{r}i} = -|\mathbf{h}|\epsilon_{\|i}$ and $q'_{\mathrm{r}i} = -|\mathbf{h}'|\epsilon_{\|i}$ for a strong reflection $\mathbf{h}$ and a weak reflection $\mathbf{h}'$, respec-

tively. For example (400) and (200) reflections can be used [KML+01]. The expression for the intensity ratio $r_{\mathrm{int}\,i} = I(q_{\mathrm{r}i} = -|\mathbf{h}|\epsilon_{\|i}) / I'(q'_{\mathrm{r}i} = -|\mathbf{h}'|\epsilon_{\|i})$ then reads

$$r_{\mathrm{int}\,i} = \left| \frac{x_i \chi^{(\mathrm{i})}_{\mathbf{h}} + (1-x_i)\chi^{(\mathrm{m})}_{\mathbf{h}}}{x_i \chi^{(\mathrm{i})}_{\mathbf{h}'} + (1-x_i)\chi^{(\mathrm{m})}_{\mathbf{h}'}} \right|^2 , \tag{2.43}$$

where $x_i \in \langle 0; 1\rangle$ is the molar concentration of the island material in the ISV i, $\chi^{(\mathrm{i})}_{\mathbf{h}}$, $\chi^{(\mathrm{i})}_{\mathbf{h}'}$ and $\chi^{(\mathrm{m})}_{\mathbf{h}}$, $\chi^{(\mathrm{m})}_{\mathbf{h}'}$ are polarizabilities of the island and substrate materials, respectively. The concentration is then calculated from

$$x_i = \frac{-B \pm \sqrt{B^2 - AC}}{A} \text{ with } 0 \le x_i \le 1, \tag{2.44}$$

where

$$A = r_{\mathrm{int}\,i} |\Delta_{\mathbf{h}'}|^2 - |\Delta_{\mathbf{h}}|^2 \tag{2.45a}$$

$$B = r_{\mathrm{int}\,i} (\mathrm{Re}\,\Delta_{\mathbf{h}'}\,\mathrm{Re}\,\chi^{(\mathrm{m})}_{\mathbf{h}'} + \mathrm{Im}\,\Delta_{\mathbf{h}'}\,\mathrm{Im}\,\chi^{(\mathrm{m})}_{\mathbf{h}'}) - (\mathrm{Re}\,\Delta_{\mathbf{h}}\,\mathrm{Re}\,\chi^{(\mathrm{m})}_{\mathbf{h}} + \mathrm{Im}\,\Delta_{\mathbf{h}}\,\mathrm{Im}\,\chi^{(\mathrm{m})}_{\mathbf{h}}) \tag{2.45b}$$

$$C = r_{\mathrm{int}\,i} |\chi^{(\mathrm{m})}_{\mathbf{h}'}|^2 - |\chi^{(\mathrm{m})}_{\mathbf{h}}|^2 \tag{2.45c}$$

$$\Delta_{\mathbf{h}} = \chi^{(\mathrm{i})}_{\mathbf{h}} - \chi^{(\mathrm{m})}_{\mathbf{h}}, \text{ and } \Delta_{\mathbf{h}'} = \chi^{(\mathrm{i})}_{\mathbf{h}'} - \chi^{(\mathrm{m})}_{\mathbf{h}'}. \tag{2.45d}$$

For GeSi islands on Si, which both crystallize in the diamond lattice, no weak reflections exist and the above mentioned method of the chemical composition determination fails. In this case, the measurements of intensities I and I' is performed at two different energies in order to ensure the essential difference between polarizabilities: the ratio of the polarizabilities must be different for the island and matrix materials $\chi^{(\mathrm{i})}_{\mathbf{h}} / \chi^{(\mathrm{i})\prime}_{\mathbf{h}} \neq \chi^{(\mathrm{m})}_{\mathbf{h}} / \chi^{(\mathrm{m})\prime}_{\mathbf{h}}$ for these two energies. Anomalous scattering near the Ge K edge ($E = 11.103$ keV) was utilized to study GeSi islands in Refs. [SSH+05, SSZ+03, MKMR+03, MPMRM+02].

The three procedures mentioned above allow to determine shape, strain and interdiffusion in NIs. However, for small q_{r}, i.e., near the substrate reflection, and for regions too far from the substrate reflection the ISSM data analysis has not yielded consistent results for the ISV elevation z_i. Alternatively, AFM line profiles of NIs were utilized to provide the relationship between the ISV elevations z_i and the radii r_i in Refs. [SSH+05, MKMR+03, SSZ+03, MPMRM+02].

2.4 Anomalous X-ray scattering

Anomalous X-ray scattering exploits abrupt changes in the scattering factor $f(\mathbf{Q}, E) = f_0(\mathbf{Q}) + f'(E) - \mathrm{i}f''(E) = |f| e^{\mathrm{i}\phi}$ [see Eq. (2.1)] of one of the sample's constituent elements in the vicinity of one of its absorption edges. For a small energy variation the scattering factor of all other elements, which do not exhibit an absorption edge near the employed energies, remains practically constant. The geometry of the X-ray experiment remains

unchanged with respect to standard measurements. The comparison of measurements at two different energies in this energy region simplifies disentanglement of contributions to the scattered intensity from strain fields and from spatial modulations of the chemical composition.

For InAs QDs on GaAs, anomalous scattering in combination with the ISSM was employed for the determination of composition in Ref. [SSC+02]. Anomalous diffraction close to the (200) reflection replaced the measurement at weak and strong reflections. The measurements were performed for two energies: 11.8 and 12.38 keV, below and above, respectively, the K edge of As ($E = 11.867$ keV). The intensity calculated from $I \propto |\chi_{200}^{\mathrm{GaAs}}|^2 \propto 16|f_{\mathrm{Ga}} - f_{\mathrm{As}}|^2$ (see Fig. 2.8) for GaAs exhibits a global minimum approximately at the latter energy. The InAs intensity is a factor of 500 stronger than the GaAs scattering in this case.

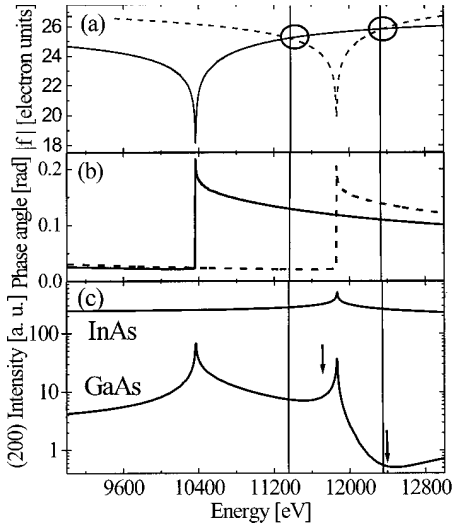

Figure 2.8. (a) Absolute values of the scattering factors of f_{Ga} (solid line) and f_{As} (dashed line), (b) corresponding complex phases ϕ_{Ga} and ϕ_{As}; (c) calculated intensity of the (200) reflections of GaAs and InAs. From Ref. [SSC+02].

Schülli et al. [SSH+05, SSZ+03] applied anomalous scattering in combination with the ISSM for characterization of Ge NIs on Si. They used high-index reflections up to (800) for two energies in the vicinity of the K edge of Ge in order to enhance the difference in the scattering factor of Ge. The usage of high-index reflections brings also higher strain resolution in the ISSM.

Mostly, only laterally averaged chemical composition of NIs was obtained from iso-strain scattering analysis in the past works. Lateral inhomogeneities of the chemical composition of uncapped Ge domes grown on Si(100) were investigate by Malachias et al. in Ref. [MKMR+03]. They showed that angular scans measured at the Ge K edge ($E = 11.103$ keV) are mostly shape sensitive, while angular scans collected at $E = 11.005$ keV, i.e., below the edge, are both chemically and shape sensitive.

Chapter 3

Generalization of the iso-strain scattering method for buried nano-islands

In Section 2.3, we reviewed iso-strain scattering method (ISSM), which allows for a direct structural characterization of *uncapped* nano-islands (NIs) from X-ray data. The elevation of an iso-strain volume (ISV), i.e., a sub-volume of a NI of constant lateral strain $\epsilon_{\|0}$, above the sample surface is determined from the intensity distribution along the q_z-axis. The characteristic maximum in the q_z intensity profiles is due to the interference between beams scattered within the islands and reflected at the sample surface before and/or after scattering. For *buried* nano-islands, this interference pattern is usually absent and the above mentioned analysis is impossible. Prof. V. Holý suggested to use a X-ray standing wave field, which arise in planar periodic multilayers (PPMLs), in order to obtain information on strain fields of buried nanostructures. If the angle of incidence α_i and/or exit α_f of the X-rays is close to the Bragg condition of PPML, a standing wave is excited in the sample with a phase along the growth direction, which results in characteristic modulations (peaks and dips) of the scattered intensity along q_z [SMPF98]. As we show in the first section of this chapter, the shape of the modulations is characteristic for a certain q_r-position, providing a method for determining the vertical position of the corresponding ISV within NIs. In the second section, we discuss the applicability of the method for various island arrangements. The method is applied for the analysis of InAs quantum dots in the next chapter.

3.1 Principle of the generalized ISSM

Here, we discuss the principle of the determination of the vertical strain distribution within buried NIs, which are arranged in a PPML as shown in Fig. 3.1(a): The PPML is formed by bi-layers consisting of a thick spacer layer and a thin wetting layer (WL). NIs are grown directly on WLs in each spacer. The lateral positions of NIs are random and uncorrelated.

As we show in the following section, the NI correlation along the growth direction is decisive for the applicability of the method.

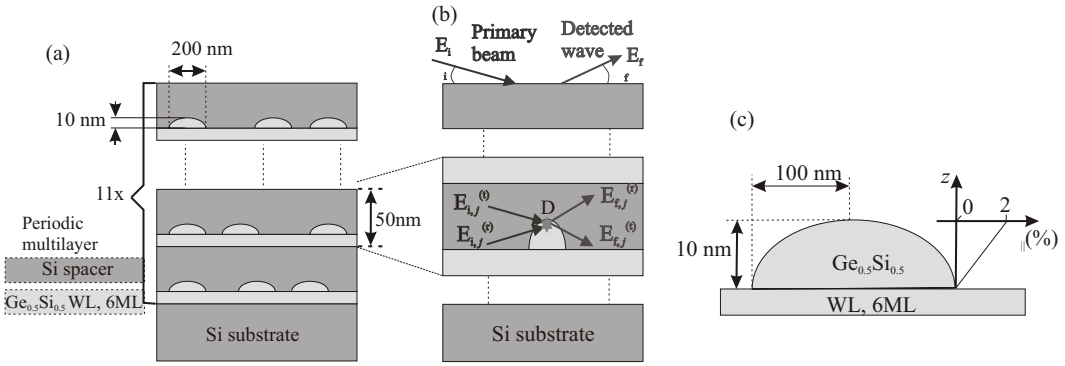

Figure 3.1. (a) Model of the island multilayer used for simulations of the q_z-profiles and the radial scan in Fig. 3.4. The multilayer consist of 11 times repeated motive of $Ge_{0.5}Si_{0.5}$/Si bi-layers of 50 nm thickness. The thickness of the GeSi wetting layer is 6 MLs $\approx$ 8.5 Å. The lateral positions of the islands are vertically uncorrelated. (b) Diffraction of X-rays on NIs in the view of DWBA. The primary beam excites a system of plane waves with positive and negative vertical wave vector components $E_{\mathrm{i},j}^{(\alpha)}$, $\alpha =$ r,t. Each of these waves is then Bragg scattered within the NIs and a new system of plane waves $E_{\mathrm{f},j}^{(\alpha)}$, $\alpha =$ r,t, arises, which is again subjected to transmission and reflection processes. (c) Island model used for simulations shown in this section. NIs in each spacer layer grow directly on the WL. NI height is 10 nm and the bottom radius is $R = 100$ nm. NI shape is rotational paraboloid. Isotropic lateral strain with respect to the Si substrate $\epsilon_{\|}$ increases linearly from 0 % at the bottom of the island to 2 % at the top of the island.

Similarly to ISSM for uncapped NIs, its generalization for buried islands is based on the analysis of measurements in the GID geometry (see Fig. 2.5). In the following we consider diffuse scattering for a momentum transfer $|\mathbf{h}| + q_{\mathrm{r}}$ corresponding to a certain in-plane lattice parameter $a_{\|} = 2\pi/(q_{\mathrm{r}} + |\mathbf{h}|)\sqrt{h^2 + k^2 + l^2}$ in NIs, which is not present in the material surrounding the NIs. Thus, we will neglect diffraction of X-rays in the lattice of the PPML. On the other hand, as the optical reflections of X-rays on the sample surface and the PPML interfaces are strong in the GID geometry, we have to treat the optical reflections of X-rays in PPML dynamically. Since NIs represent only a small volume portion of the sample we may consider the crystalline NIs as a small perturbation. The decomposition of the investigated system on a multilayer, for which the solution of the wave equation is known, and a small perturbation enable us to calculate the scattered intensity in the framework of Distorted Wave Born Approximation (DWBA) (see Sec. 2.1.2), treating the diffraction of X-rays in NIs kinematically.

In view of this approximation, the primary beam, impinging under an angle α_{i} onto the sample surface, excites a system of plane waves with positive and negative wave vector components in z-direction. These waves are partially transmitted and partially specularly reflected at the interfaces of the multilayer (see Fig. 2.2). A wave travelling through a spacer layer is then scattered within a NI and a new system of plane waves arises [see Fig. 3.1(b)], which is again subjected to transmission and reflection processes at the

interfaces. A particular final wavefield that results in a vacuum plane wave with wave vector $\mathbf{K}_\mathrm{f}$, leaving the sample under an angle α_f with respect to the surface, is then selected by the position of the detector.

For simplicity, we assume all island shapes and deformation fields are identical. In particular, we neglect the surface stress relaxation. For our structural model, the diffusely scattered intensity of the wave with the total momentum transfer $\mathbf{q}+\mathbf{h}$ with respect to the primary wave is proportional to the sum of intensities of the waves scattered by a single island in each layer:

$$I_\mathrm{NIs}(\mathbf{q}) \propto |\delta\chi_\mathbf{h}|^2 \sum_{j=1}^{M} \left| \int \mathrm{d}^3\mathbf{r}\Omega(\mathbf{r}-z_{2j-1}\hat{\mathbf{z}}) \exp(-\mathrm{i}(\mathbf{q}_\parallel\cdot\mathbf{r}_\parallel + \mathbf{u}(\mathbf{r})\cdot\mathbf{h})) \right.$$
$$\left. \times \sum_{\alpha,\beta=\mathrm{r,t}} E^{(\alpha)}_{\mathrm{i}\,2j-1} E^{(\beta)}_{\mathrm{f}\,2j-1} \exp(-\mathrm{i}q^{(\alpha,\beta)}_{z\,(2j-1)}(z-z_{2j-1})) \right|^2 . \tag{3.1}$$

Here, $\Omega(\mathbf{r})$ is the shape function of NIs (unity inside NI, zero outside it), $\delta\chi_\mathbf{h}$ is the difference of the $\mathbf{h}$-th polarizability coefficient of the island lattice and the surrounding cap layer, $\mathbf{q}_\parallel$ is the in-plane component of the wave vector transfer measured with respect to the reciprocal lattice vector $\mathbf{h}$ and $E^{(\alpha)}_{\mathrm{i}\,2j-1}$ and $E^{(\beta)}_{\mathrm{f}\,2j-1}$ are complex amplitudes of the initial and final wave fields, respectively, at the bottom of the $(2j-1)$st layer, calculated by Eq. (2.12). $\delta\chi_\mathbf{h}$ is assumed to be constant within the whole island, for the simplicity. The superscript indices r and t refer to the reflected and transmitted waves, respectively, z_{2j-1} is vertical position of the interface $2j-1$ (see Fig. 2.2), $\hat{\mathbf{z}}$ is the coordinate unit vector along the growth direction and M is number of island layers. The complex vertical momentum transfers in the spacer layers are

$$q^{(\mathrm{t,t})}_{z\,j} = -k^{(\mathrm{f})}_{z\,j} - k^{(\mathrm{i})}_{z\,j},\ q^{(\mathrm{r,t})}_{z\,j} = -k^{(\mathrm{f})}_{z\,j} + k^{(\mathrm{i})}_{z\,j},\ q^{(\mathrm{t,r})}_{z\,j} = k^{(\mathrm{f})}_{z\,j} - k^{(\mathrm{i})}_{z\,j},\ q^{(\mathrm{r,r})}_{z\,j} = k^{(\mathrm{f})}_{z\,j} + k^{(\mathrm{i})}_{z\,j}.$$

$k^{(\mathrm{i})}_{z\,j}$, $k^{(\mathrm{f})}_{z\,j}$ are vertical components of the wave vector of the transmitted incident wave and time inverted final wave, respectively, in the layer j, which are calculated by Eq. (2.8).

In the following we will deal only with the q_z intensity profile at q_r fixed at an arbitrary $q_{\mathrm{r}0}$ and let q_a be fixed at 0. We will assume that the strain tensor components ϵ_{xx} and ϵ_{yy} are equal to $\epsilon_\parallel$ and neglect shear components. Thus the term $\mathbf{u}(\mathbf{r})\cdot\mathbf{h}$ reduces to $\Omega(\mathbf{r})\epsilon_\parallel(z)(\mathbf{r}_\parallel\cdot\mathbf{h}_\parallel)$[1]. If the ISV of strain $\epsilon_{\parallel 0} = -q_{\mathrm{r}0}/|\mathbf{h}|$ spreads along a small section of the $z-$axis around a position δz_0 above the island base in each NI and the condition (2.37) holds, then Eq. (3.1) can be approximated by

$$I_{\mathrm{disc},\,q_{\mathrm{r}0}}(\alpha_\mathrm{i},\alpha_\mathrm{f}) \propto \sum_{j=1}^{M} \left| T_{\mathrm{i}\,(2j-1)}\,(\alpha_\mathrm{i},\delta z_0)\, T_{\mathrm{f}\,(2j-1)}\,(\alpha_\mathrm{f},\delta z_0) \right|^2 ,$$
$$\delta z_0 = \epsilon_\parallel^{-1}\left(-\frac{q_{\mathrm{r}0}}{|\mathbf{h}|}\right), \tag{3.2}$$

[1] In our model we consider only scattering on the island lattice and the deformation outside the island is arbitrarily set to $\mathbf{u}=0$.

where

$$T_{\gamma\,(2j-1)}(\alpha_\gamma, \delta z) = E^{(\mathrm{r})}_{\gamma\,(2j-1)} \mathrm{e}^{-\mathrm{i}k^{(\gamma)}_{z\,(2j-1)}\delta z_0} + E^{(\mathrm{t})}_{\gamma\,(2j-1)} \mathrm{e}^{+\mathrm{i}k^{(\gamma)}_{z\,(2j-1)}\delta z_0} \tag{3.3}$$

and $\delta z = \epsilon_{\|}^{-1}(\epsilon_{\|})$ denotes the inversion function. In other words, approximating Eq. (3.1) by Eq. (3.2) we assume that NIs can be dissected into thin discs, i.e., ISVs, of strain $\epsilon_{\|}(\delta z)$, each of them contributing only to the q_z intensity profile taken at $q_\mathrm{r}(\delta z) = -\epsilon_{\|}(\delta z)|\mathbf{h}|$.

The expression in the sum over α, β in Eq. (3.1) is identical to the product $T_{\mathrm{i}\,(2j-1)}\,(\alpha_\mathrm{i}, \delta z) \cdot T_{\mathrm{f}\,(2j-1)}\,(\alpha_\mathrm{f}, \delta z)$ in Eq. (3.2) and gives rise to the above mentioned modulations (peaks and dips) of the q_z-profiles. If α_i and/or α_f are close to the Bragg condition of the PPML (see Fig. 3.2), the initial and/or final wave fields, $T_{\mathrm{i}\,(2j-1)}\,(\alpha_\mathrm{i}, \delta z)$, $T_{\mathrm{f}\,(2j-1)}\,(\alpha_\mathrm{i}, \delta z)$, respectively, become standing waves, which modulate the scattering contributions from different parts of NIs. When α_i or α_f slightly change, still staying in the vicinity of the Bragg condition, the nodes and anti-nodes of the standing wave shift along the height of the NI, i.e., along the vertical $z-$axis (see Fig. 3.3). As a consequence, peaks and dips arise in the q_z-profiles at these positions of α_f when intensity is measured for fixed α_i along the PSD. Such a measurement corresponds to the experimental set-up shown in Fig. 2.5, which is usually employed to collect the experimental data measured in GID experiments. The shapes of the peaks and dips are characteristic for a certain position $q_{\mathrm{r}0}$ because it is connected to a certain direct space position δz_0 as shown by Eq. (3.2).

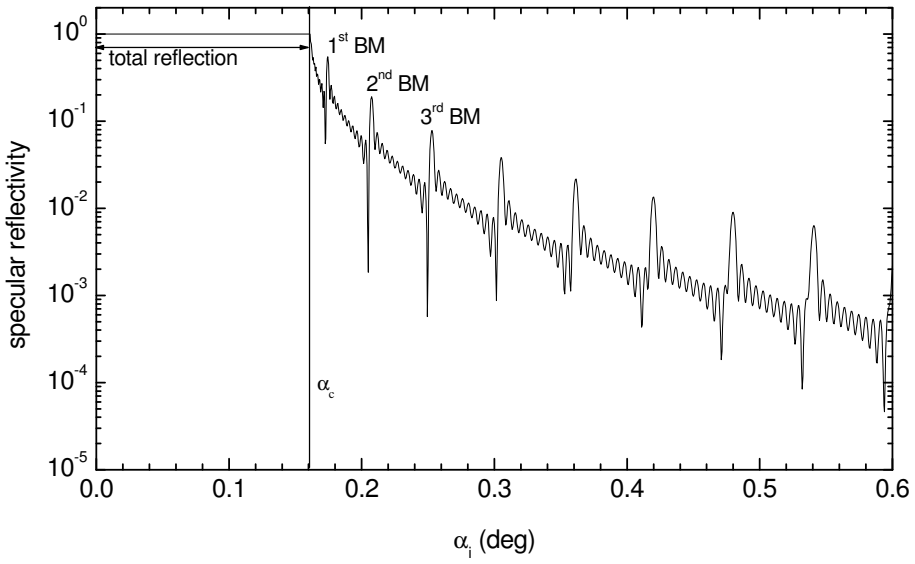

Figure 3.2. Simulation of the specular reflectivity for the GeSi/Si PPML shown in Fig. 3.1(a). Interfaces in the multilayer are considered to be perfectly smooth and the islands are neglected in the calculation. Bragg maxima of the multilayer are denoted by BM. The reflectivity is equal to unity for incidence angles smaller than the critical angle α_c.

A series of simulations was done to show that the shape of the intensity modulations can be successfully simulated by Eq. (3.2) for proposed experiments with GeSi/Si islands. A simulation of a radial map calculated by Eq. (3.1) for GeSi NIs in a PPML is shown in Fig. 3.4(a). The PPML and NIs models are shown in Figs. 3.1(a) and 3.1(c), respectively.

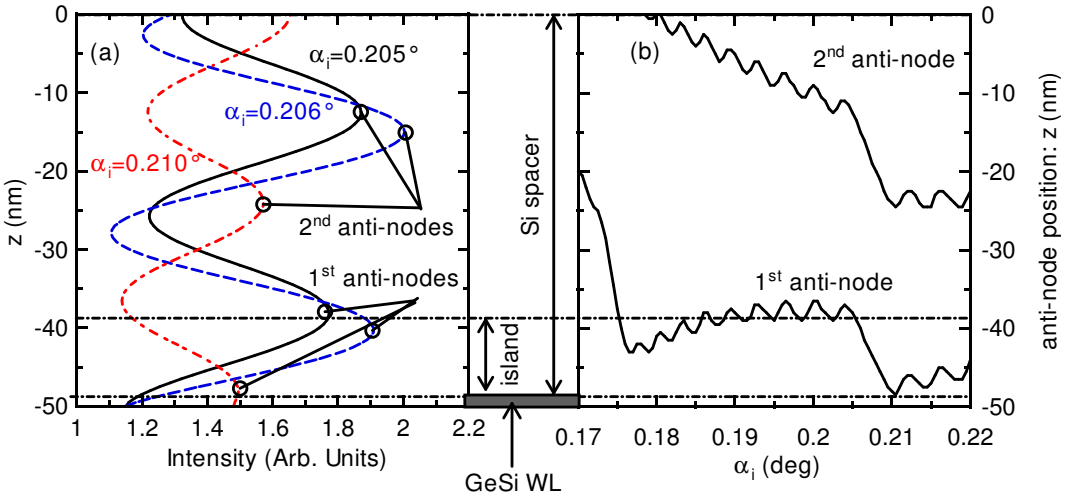

Figure 3.3. (a) Standing wave field intensities in the topmost bi-layer of the multilayer shown in Fig. 3.1(a) as calculated from Eq. (3.3) for the three positions of $\alpha_i = 0.205°$, $0.206°$, and $0.210°$. The nodes and antinodes of the standing wave shift along the height of the island. (b) Vertical positions of the first two standing wave anti-nodes as a function of the incidence angle α_i. The structure of the bi-layer and the extension of islands along the vertical z axis are indicated by horizontal lines and the legend between the panels (a) and (b).

The calculation was done for an X-ray wavelength of 1.123 Å and and angle of incidence of $\alpha_i = 0.2°$, which is larger than the critical angle of the Si spacer $\alpha_c = 0.162°$. The discussed intensity modulations are visible as tiny horizontal sheets at positions of α_f equal to the Bragg angles of the PPML . In Fig. 3.4(b), q_z intensity profiles calculated by Eq. (3.1) for GeSi NIs [Fig. 3.1(c)] in a PPML [Fig. 3.1(a)] are plotted as black solid lines. In fact, these q_z intensity profiles are cuts along q_z-axis through the radial map in Fig. 3.4(a) at q_r positions corresponding to the lateral strains $\epsilon_{\|1} = 0.5$ % and $\epsilon_{\|2} = 1.0$ % [indicated by vertical lines in Fig. 3.4(a)]. ISVs of these lateral strains occurs in the vertical positions $\delta z_1 = 2.5$ nm and $\delta z_2 = 5$ nm, respectively, in the model island [Fig. 3.1(c)]. In Fig. 3.4(b), the q_z-profiles calculated for scattering on the whole island are compared to q_z-profiles calculated for scattering on iso-strain discs using Eq. (3.2) (plotted as red dots). The calculation was performed for the vertical positions of the discs δz_1 and δz_2, i.e., that of to the ISVs. The shape of the peaks and dips calculated using Eqs. (3.1) and (3.2) is very similar. This gives a chance, that q_z-profiles measured in an experiment for real islands can be simulated by Eq. (3.2). By such simulations one can determine the vertical position δz of ISV of a certain strain $\epsilon_{\|} = -q_r/|\mathbf{h}|$ within buried islands. Furthermore, we can see that the shape of the features differ for the q_z-profiles for discs at $\delta z_1 = 2.5$ nm and $\delta z_2 = 5$ nm. As a summary, the vertical strain distribution within NIs similar to our model can be determined using simulations of q_z-profiles by Eq. (3.2) with approximate resolution $\delta\epsilon_{\|} = 0.5$ %.

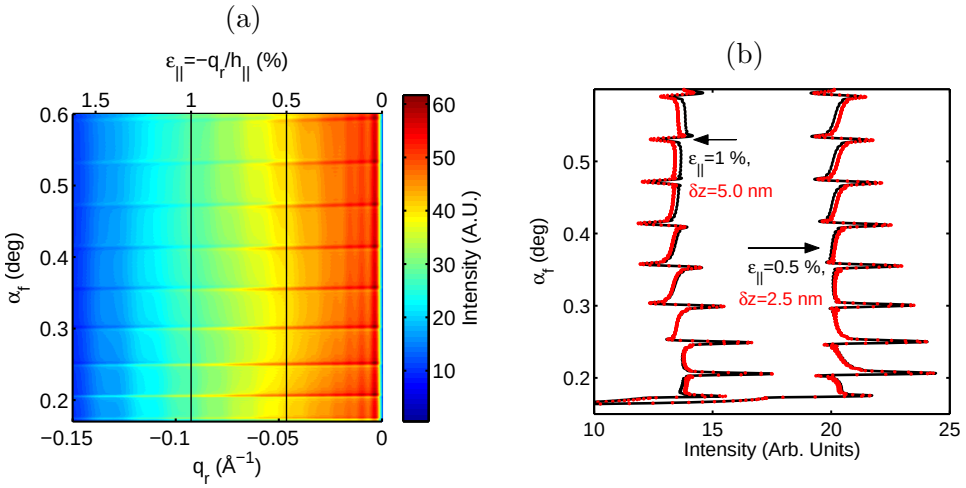

Figure 3.4. (a) Simulation of a radial map calculated by Eq. (3.1) for GeSi NIs [model shown in Fig. 3.1(c)] in a PPML [model shown in Fig. 3.1(a)]. The vertical lines denote positions of the q_z sections through the map, which are plotted by black lines in panel (b). (b) Comparison of q_z-profiles calculated by Eq. (3.1) (black lines) and q_z-profiles calculated by Eq. (3.2) (red dots). Eq. (3.2) is an approximation of Eq. (3.1) and represents scattering on a thin disc at a certain vertical position δz in the PPML. Calculation of q_z-profiles by Eq. (3.1) was performed for q_r-positions corresponding to lateral strain $\epsilon_{\parallel 1} = 0.5$ % and $\epsilon_{\parallel 2} = 1$ %. Calculation of q_z-profiles by Eq. (3.2) was performed for discs in the vertical positions $\delta z_1 = 2.5$ nm and $\delta z_2 = 5$ nm, where ISVs of strains $\epsilon_{\parallel 1}$ and $\epsilon_{\parallel 2}$, respectively, occur in the model island.

3.2 Applicability of the generalized ISSM for various island arrangements

In this section we discuss the applicability of the generalized ISSM for three types of island arrangements shown in Fig. 3.5. In the arrangement (a), only one island layer is grown above a PPML. In the arrangements (b) and (c), the PPML is formed by alternating of WLs and spacer layers. NIs are present in each spacer layer. For the arrangement (b), the lateral positions of the islands are not correlated in the subsequent island layers. For the arrangement (c), NIs are vertically stacked in columns. The NI positions within the bottom island layer are random. Such considerations are of importance because various three-dimensional island stacking occur in real samples. Vertical stacking along the growth direction was reported for Ge/Si islands, e.g., in Refs. [Tha04, Bru02, DSH$^+$97], and for InAs/GaAs quantum dots [DHS$^+$97, XMCK95]. Oblique positioning or even anticorrelation of NIs lateral positions in subsequent island layers was reported for both Ge/Si NIs [KCB04, SMSV01] and for InAs/GaAs QDs [WLS$^+$04]. The type of NI correlation actually formed depends on a large variety of parameters such as the thicknesses of spacer layers and WLs, elastic properties of the materials, the surface orientation, the growth conditions and the chemical composition [Spr05, LNG$^+$99, HSPB99].

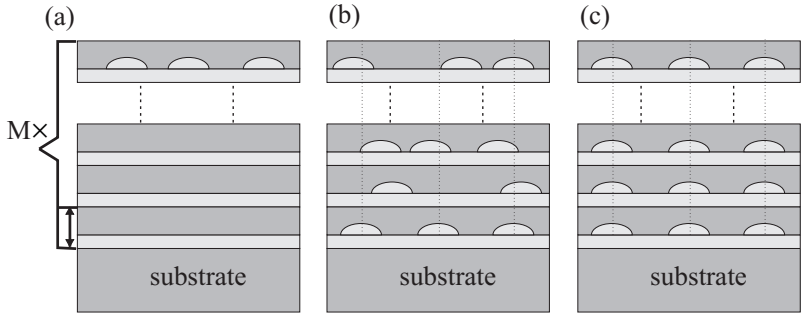

Figure 3.5. Various types of NI arrangements in PPMLs, which were considered for application of the generalized ISSM. (a) NIs are grown in the topmost spacer of a PPML. (b) NIs are grown in each spacer of the PPML. There is no correlation of lateral positions in the subsequent island layers. (c) The NIs are grown in each spacer of the PPML. NIs are vertically stacked.

In the following, we show simulations of the scattered intensity for the three NI arrangements. The intensity scattered on NIs arranged according to scheme (b), is calculated using the formula in Eq. (3.1). For NI arrangement (a), the formula for the scattered intensity reads

$$I_{\mathrm{NIs}}(\mathbf{q}) \propto |\delta\chi_{\mathbf{h}}|^2 \left| \int \mathrm{d}^3\mathbf{r}\Omega(\mathbf{r} - z_1\hat{\mathbf{z}}) \exp(-\mathrm{i}(\mathbf{q}_\parallel \cdot \mathbf{r}_\parallel + \mathbf{u}(\mathbf{r}) \cdot \mathbf{h})) \right. \\ \left. \times \sum_{\alpha,\beta=\mathrm{r,t}} E_{\mathrm{i}\,1}^{(\alpha)} E_{\mathrm{f}\,1}^{(\beta)} \exp(-\mathrm{i}q_{z\,(1)}^{(\alpha,\beta)}(z - z_1)) \right|^2 . \tag{3.4}$$

For NI arrangement (c), scattering contributions from a NI column have to be summed coherently as

$$I_{\mathrm{NIs}}(\mathbf{q}) \propto |\delta\chi_{\mathbf{h}}|^2 \left| \sum_{j=1}^{M} \int \mathrm{d}^3\mathbf{r}\Omega(\mathbf{r} - z_{2j-1}\hat{\mathbf{z}}) \exp(-\mathrm{i}(\mathbf{q}_\parallel \cdot \mathbf{r}_\parallel + \mathbf{u}(\mathbf{r}) \cdot \mathbf{h})) \right. \\ \left. \times \sum_{\alpha,\beta=\mathrm{r,t}} E_{\mathrm{i}\,2j-1}^{(\alpha)} E_{\mathrm{f}\,2j-1}^{(\beta)} \exp(-\mathrm{i}q_{z\,(2j-1)}^{(\alpha,\beta)}(z - z_{2j-1})) \right|^2 . \tag{3.5}$$

By analogy with the approximation of Eq. (3.1) by Eq. (3.2), Eqs. (3.4) and (3.5) can be approximated by

$$I_{\mathrm{disc},\,q_{\mathrm{r}0}}(\alpha_\mathrm{i}, \alpha_\mathrm{f}) \propto \left| T_{\mathrm{i}\,(1)}(\alpha_\mathrm{i}, \delta z_0)\, T_{\mathrm{f}\,(1)}(\alpha_\mathrm{f}, \delta z_0) \right|^2 \text{ and} \tag{3.6a}$$

$$I_{\mathrm{disc},\,q_{\mathrm{r}0}}(\alpha_\mathrm{i}, \alpha_\mathrm{f}) \propto \left| \sum_{j=1}^{M} T_{\mathrm{i}\,(2j-1)}(\alpha_\mathrm{i}, \delta z_0)\, T_{\mathrm{f}\,(2j-1)}(\alpha_\mathrm{f}, \delta z_0) \right|^2 , \tag{3.6b}$$

$$\delta z_0 = \epsilon_\parallel^{-1} \left(-\frac{q_{\mathrm{r}0}}{|\mathbf{h}|} \right),$$

respectively.

In all presented simulations we consider the PPML structure shown in Fig. 3.1(a) and the NI structure shown in Fig. 3.1(c). Simulations of the q_z intensity profiles for all three NIs arrangements are presented in Fig. 3.6. Several number of GeSi/Si bi-layers in PPML are considered in all cases. The simulations were performed for a q_r-position corresponding to the lateral strain $\epsilon_{\|} = 1$ %, an X-ray wavelength of $\lambda = 1.123$ Å and an incidence angle of $\alpha_i = 0.2°$. For NI arrangements (a) and (b), the intensity modulations (peaks and dips) are clearly visible. They become better pronounced with increasing number of bi-layers in the PPML. The angular width (along α_f) of the peaks and dips is inversely proportional to the number of bi-layers. Thus, the maximal useful number of bi-layers is limited by the finite angular resolution of the detector in the experiments. The pronouncement of the intensity modulations also increases with increasing difference of the 0th order polarizabilities χ_0 of spacer layers and WLs (not shown in the figure). For NI arrangement (c), the intensity modulations are overshadowed by maxima arising due to the periodicity of the island positions along the growth direction. Structural analysis using the fitting of the intensity modulation shapes, presented here, is not possible in this case. However, the modulations due to the standing wave can be observed for arrangement (c) if the incidence angle of the primary beam is smaller than the critical angle of the spacer (see Fig. 3.7). In this case, only several topmost island layers are effectively irradiated due to the small penetration depth.

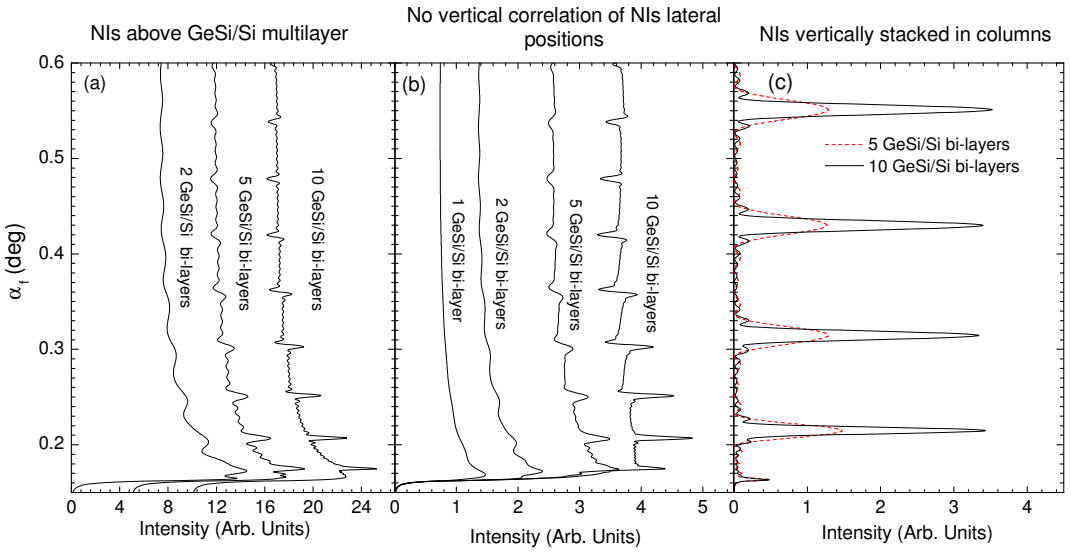

Figure 3.6. Simulation of q_z-profiles for scattering on NIs arranged in GeSi/Si multilayers according to the schemes shown in Figs. 3.5(a-c). The type of NI arrangement for individual graphs are given in the graph titles. Simulations for various numbers of GeSi/Si bi-layers in the multilayer are plotted in each graph.

In summary, to obtain experimental data, which can be analyzed using the presented method, one can optimize the experimental conditions in several ways. The tiny intensity modulations, which are crucial for the data evaluation, can be enhanced by increasing the number of bi-layers M in the PPML and by increasing the contrast of χ_0 of PPML layers.

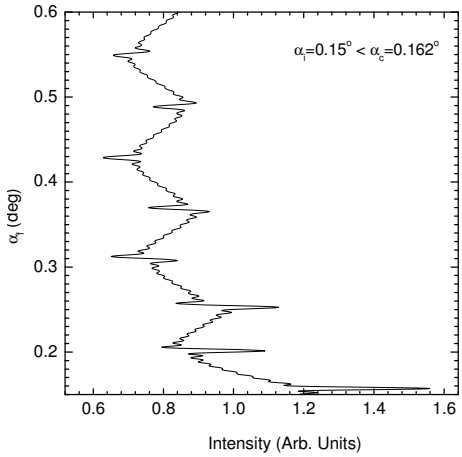

Figure 3.7. Simulation of a q_z intensity profiles for scattering on 10 vertically stacked island layers [as in Fig. 3.6(c)]. In this case, the incidence angle of $\alpha_i = 0.15°$ is smaller than the critical angle of the Si spacer $\alpha_c = 0.161°$.

The latter can be achieved by a proper choice of PPML materials and/or by optimizing the X-ray wavelength, i.e., measuring in the vicinity of an absorbtion edge of one of PPML materials. Maximal number of the PPML bi-layers is limited by the angular α_f resolution of the detector in use.

Chapter 4

Studies on MBE-grown InAs/GaAs QDs using ISSM

This chapter deals with InAs QDs grown by molecular beam epitaxy (MBE) at Max-Planck Institute (MPI) Stuttgart. For these QDs, growth rates as low as 0.01 ML/s, and high growth temperatures (500 °C) were applied, which leads to a significant improvement of QD size homogeneity [SKN+02] compared to conventional growth techniques.

In the first section of this chapter, we present an application of the generalized iso-strain scattering method (ISSM) for buried nano-islands, which was introduced in Chap. 3. In the second section, we show a structural study on an 11-fold multilayer of InAs/GaAs QDs grown partially above a flat part of a GaAs substrate and partially above a patterned part of the substrate. Beside the structure of uncapped QDs of the topmost dot layer we were also able to get information on the quality of ordering in the topmost island layer.

4.1 A study of buried QDs using generalized ISSM

4.1.1 Introduction

In this section, we show an application of the generalized ISSM for the analysis of buried QDs grown on a planar periodic multilayer (PPML). In this method, the strain distribution within buried QDs along the growth direction is determined from the shape of characteristic modulations (peaks and dips), which occur in q_z intensity profiles measured in GID geometry (see Sec. 3.1). Results of X-ray analysis of QDs are compared to transmission electron microscopy (TEM) images of the dots and simulations of photoluminescence (PL) measurements.

From the three QD arrangements proposed for the application of the generalized ISSM in Sec. 3.2, we have chosen that one with only one QD layer, i.e., the arrangement (a) shown in Fig. 3.5. For this arrangement, the loss of the characteristic modulations does not occur for higher incidence angles $\alpha_i > \alpha_c$ as it does for vertically stacked QDs (arrangement (c) shown in Fig. 3.5). Additionally, in QD multilayers (arrangements (b,c) in Fig. 3.5), fluctuations of the structural properties (sizes, chemical composition) of QDs in different

layers may occur. Such fluctuations would lead to a blurring or total disappearance of the characteristic intensity modulations.

4.1.2 Experiment

Sample structure and growth

The nominal structure of the investigated sample is shown in Fig. 4.1(a). The investigated sample structure was designed to obtain as much intensity as possible in the 1st and 2nd Bragg peaks of the PPML in order to enhance the intensity variations in the cusps and peaks. In an optimum case, the cap layer should be thicker than the QD height by only 2 nm, in order to reduce intensity losses by absorbtion. The PPML period was chosen approximately equal to the thickness of the cap to maintain the same 'periodicity' for the whole structure. As our intention was to study strain in InAs QDs embedded in GaAs, GaAlAs/GaAs bi-layers were used for the PPML underneath the QDs: The combination of these two materials yields sufficient electron density contrast for X-ray reflectivity on the one hand, and virtually no mismatch on the other hand, so that highly perfect multilayers can be grown. Growing a PPML with more bi-layers increases the intensity of the PPML Bragg peaks, and decreases the width of the cusps along q_z (see Sec. 3.2). The practical limit to the number of periods is that the width of the cusps must remain larger than the experimental resolution along q_z.

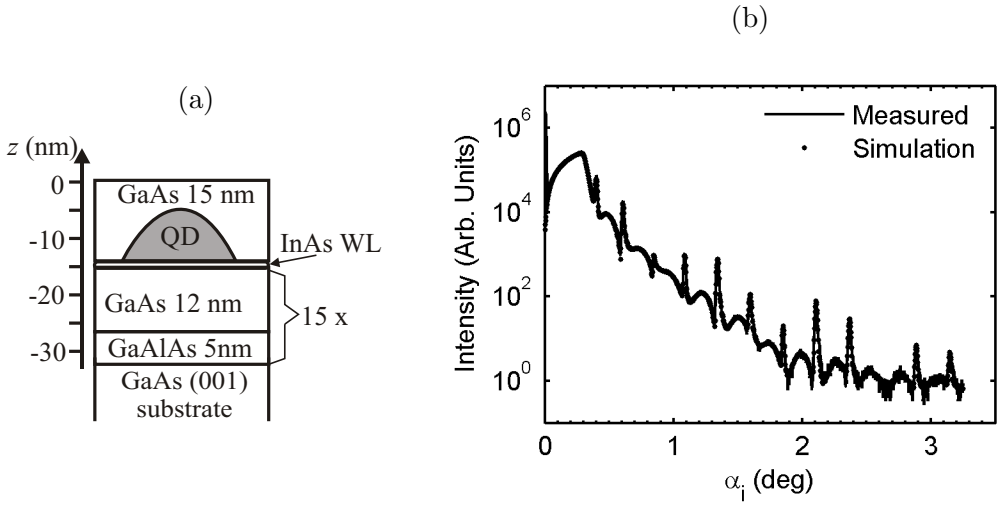

Figure 4.1. (a) Nominal structure of the investigated sample and model structure for simulations. (b) Measured specular reflectivity of the investigated sample (line) and the best fit obtained (dots).

InAs QDs on top of the 15-period GaAs/$Ga_{0.6}Al_{0.4}As$ PPML were grown by MBE by S. Kiravittaya (MPI Stuttgart). 1.8 MLs of InAs were deposited at a growth rate of 0.01 ML/s at 500 °C. The QDs were capped by 15 nm of GaAs at a substrate temperature of 460 °C to reduce InAs/GaAs intermixing. Atomic force microscopy images revealed a somewhat rough surface of the complete structure, which could introduce undesirable

diffuse X-ray scattering. To avoid this effect, the sample was annealed at 580 °C for 10 min.

X-ray measurements

The PPML was characterised by X-ray specular reflectivity [see Fig. 4.1(b)]. Simulations of the experimental data yielded a root mean square (r.m.s.) roughnesses of 0.7 nm for the GaAs/GaAlAs interfaces, and 0.4 nm for the GaAlAs/GaAs interfaces in the PPML, and 0.4 nm for the GaAs cap layer. The thicknesses of the respective layers are 5.0 nm for GaAlAs, 11.9 nm for GaAs in the PPML, and 14.8 nm for the GaAs cap. In addition, an oxide layer of 1.2 nm thickness and 0.5 nm r.m.s. roughness was found on top of the GaAs cap. These parameters were used as an input for the simulations of the q_z-profiles shown in the next section.

GID measurements were performed at beamline ID10B (TROÏKA II) at the ESRF in Grenoble at a wavelength of 1.549 Å. A PSD oriented perpendicular to the sample surface was used as shown in Fig. 2.5, yielding an angular resolution $\Delta\alpha_f = 0.003°$, which results in a reciprocal space resolution $\Delta q_z = 2 \cdot 10^{-4}$ Å^{-1} along q_z direction. q_z-scans were measured in the vicinity of the GaAs(220) Bragg reflection at q_r-positions corresponding to in-plane strains $\epsilon_{\|}$ ranging from -0.8 % to 2.6 % in steps of 0.3 %. The intensity profiles along q_z for each of the q_r positions was obtained by averaging PSD scans taken at two α_f positions of the PSD, in order to eliminate artifacts caused by fluctuations in the PSD sensitivity. The incidence angle was set to the second Bragg peak of the PPML at $\alpha_i = 0.606°$.

Furthermore, 2D reciprocal space maps were measured in the q_r, q_a plane around (440) and $(4\bar{4}0)$ in-plane reciprocal lattice points, keeping the incidence angle at $\alpha_i = 0.3°$. For these reciprocal space maps the PSD spectra were integrated in the range $\alpha_f = 0° - 1.1°$.

AFM analysis

A sample with the same structure as the investigated one was grown with the InAs QDs left uncapped, i.e., the topmost GaAs capping layer was not grown. The uncapped QDs were characterized using atomic force microscopy, yielding a radius of the QDs of approximately 30 nm and a height of 12 nm.

Photoluminescence

Room temperature PL spectra were measured using a Bruker 55 Fourier transform infrared spectrometer. The PL was excited by the 1.06 μm line of a Nd:YAG laser with a power of 50 mW.

4.1.3 Results and discussion

Several measured q_z-profiles are shown in Fig. 4.2(a). Cusps up to the 2nd order are observed in all scans. However, the shape of the cusps is the same for all the q_z-profiles,

except for that corresponding to $\epsilon_{\|} = 2.6$ %. In this case we observe a dip instead of a peak at $\alpha_f = 0.395°$. The similarity of the cusp shape for the smaller strain values $\epsilon_{\|} < 2.6$ % is a consequence of the fact that the corresponding ISVs are extended along the vertical axis: While some bending of the ISVs does not affect the analysis considerably, in buried QDs the strain is not a monotonic function of height in the dot, contrary to the case of uncapped islands. Low strain values are present at the bottom of the island, but also at the top part and/or above the island. Hence, different regions with the same in-plane lattice parameter, but different phases relative to the standing wave contribute to the scattering signal, and the approximation of Eq. (3.6a) cannot be made. In practice, this leads to a blurring of the cusps. For high strain values the situation is better, as they are present only inside the QDs, and the assumptions made in Eq. (3.6a) are valid. Fig. 4.2(b) shows the q_z-profile measured at $\epsilon_{\|} = 2.6$ % together with a simulation, which yields a vertical position $z = -8$ nm, of the corresponding ISV, i.e., 8 nm above the base of the QD. Although the shape of the q_z-profile between the cusps is determined by the actual shape of the ISV, i.e., its curvature and height along the $z-$axis, and is not captured correctly by the simulation, the small dip is very sensitive to the height of the ISV above the island base.

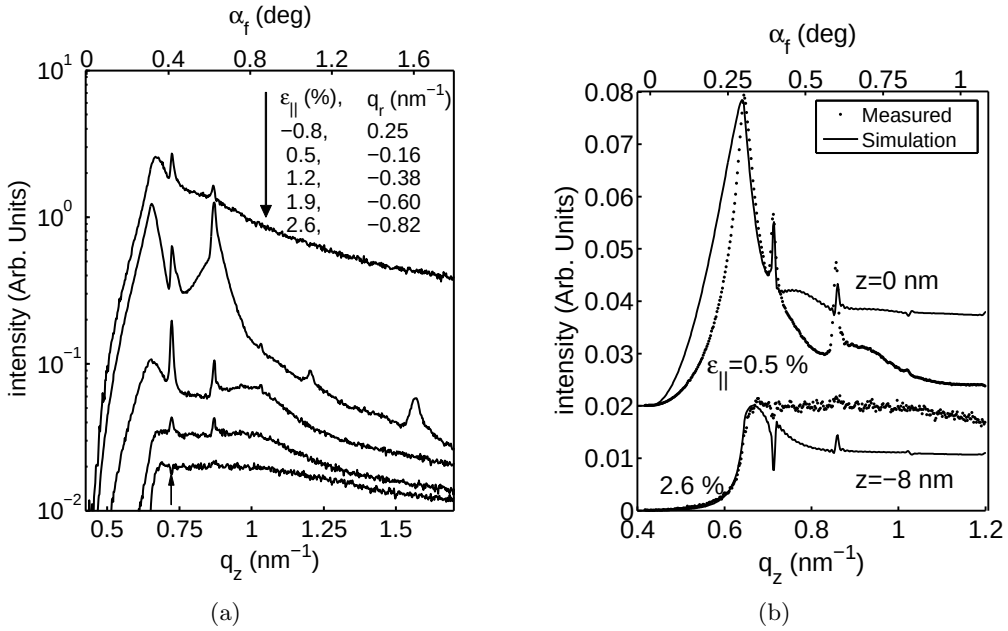

(a) (b)

Figure 4.2. (a) Measured q_z intensity profiles for ISVs of strains $\epsilon_{\|} = 2.6\,\%$, $1.9\,\%$, $1.2\,\%$, $0.5\,\%$ and $-0.8\,\%$ (from bottom to top). The arrow at $q_z = 0.72$ nm^{-1} indicates the dip in the q_z-profile for $\epsilon_{\|} = 2.6\,\%$. (b) Measured q_z intensity profiles for $\epsilon_{\|} = 2.6$ % and 0.5 % (from bottom to top) and their simulations using Eq. (3.6a).

In addition, the q_z intensity profile for a low strain of $\epsilon_{\|} = 0.5$ % was simulated by the scattering from a disc at the surface of the sample ($z = 0$ nm). The blurring of the cusps can clearly be seen in Fig. 4.2(b): the experimental peak width is significantly larger than

the simulated one. In addition to the blurring, it cannot be excluded that the peaks in the scans for $q_r = -0.038$ Å^{-1}, -0.016 Å^{-1} and 0.025 Å^{-1} originate due to the PPML itself.

Our generalization of the ISSM was worked out for a simplified QD model with flat ISVs, as presented in Secs. 2.3 and 3.1. For such a strain distribution in QDs with a morphology similar to the investigated QDs, an analysis employing the generalized ISSM would be possible. To prove that fact, we compare q_z-profiles calculated by the 'exact' Eq. (3.4) and the iso-strain approximation of Eq. (3.6a) in Fig. 4.3. In this case, the morphology of the QD was similar to that obtained from AFM images taken on uncapped QDs. In particular, we assumed the QD shape to be a circular symmetric paraboloid of bottom radius $R_{\mathrm{dot}} = 30\,\mathrm{nm}$ and height $h_{\mathrm{dot}} = 12\,\mathrm{nm}$. Furthermore, we assumed that the lateral strain within the QD evolves linearly from 0 % at the bottom to 6 % at top of the QD and that the QD is grown in the multilayer shown in Fig. 4.1(a). The q_z intensity profiles were calculated for q_r positions corresponding to $\epsilon_{\|} = 1.0$ %, 2.6 %, and 3.0 %. These lateral strains occur in the ISVs in the vertical positions $z = -13\,\mathrm{nm}$, $-9.8\,\mathrm{nm}$ and $-9\,\mathrm{nm}$. The shapes of the characteristic intensity modulations calculated using Eqs. (3.4) and (3.6a) are very similar. Furthermore, we can see that the shape of the cusps of the 2nd order differs for the q_z-profiles for discs at $z = -9.8\,\mathrm{nm}$ and $-9\,\mathrm{nm}$. Thus, we can conclude that the vertical strain distribution within the QDs similar to our simplified model can be determined using simulations of q_z-profiles by equation (3.6a) with a resolution up to 1 nm.

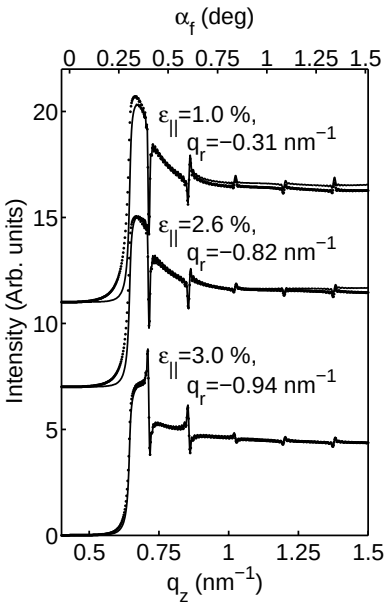

Figure 4.3. Comparison of q_z intensity profiles simulated for scattering on a QD (solid line) and discs (points) using Eqs. (3.4) and (3.6a), respectively. The q_z-profiles were simulated for q_r positions corresponding to $\epsilon_{\|} = 1.0$ %, 2.6 %, and 3.0 % (from top to bottom), which occurs at vertical positions $z = -13\,\mathrm{nm}$, $-9.8\,\mathrm{nm}$ and $-9\,\mathrm{nm}$ in our model dot.

Hence, it turns out that for our sample the measurements of the q_z-profiles for various q_r values alone is not sufficient for a full analysis of the height profile of strain in the dots. Therefore we additionally performed calculations of the strain field in the buried QDs using an analytical method [RHH$^+$02]. For simplicity, we assumed that the QDs are circular symmetric paraboloids with a base radius R_{dot} and a height h_{dot}, and that the In content c_{In} is constant inside the QDs. Within a series of simulations, we searched for

such combinations of R_{dot} and h_{dot} which led to a lateral strain $\epsilon_{\parallel} = 2.6$ % at the vertical position of $z = -8$ nm. The resulting combinations are plotted for In contents of 50 % and 100 % in Fig. 4.4. Obviously, for 50 % In content QDs with unrealistically steep sidewalls need to be assumed in order to reproduce the observed strain values, so that a higher In content is more likely.

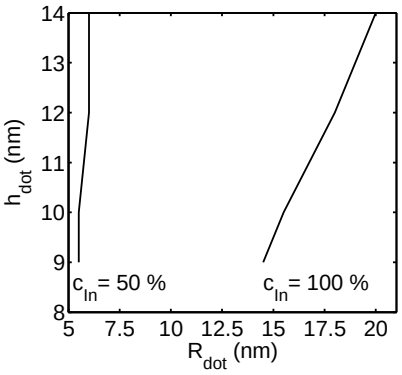

Figure 4.4. Combinations of QDs base radii R_{dot} and heights h_{dot} which lead to an ISV of lateral strain $\epsilon_{\parallel} = 2.6$ % at $z = -8$ nm for In content $c_{\mathrm{In}} = 50$ % and $c_{\mathrm{In}} = 100$ %, respectively.

To further refine the results, we measured RSMs close to the (440) and (4$\bar{4}$0) in-plane reflections (see Fig. 4.5) to obtain information about the lateral QD size. From cuts along the $q_{\mathrm{a}}-$axis through the RSMs at various q_{r} positions, the half widths of the corresponding ISVs $R(\epsilon_{\parallel})$ were obtained by fitting with the model function $I = A\sin^2(q_{\mathrm{a}}R(\epsilon_{\parallel}))/(q_{\mathrm{a}}R(\epsilon_{\parallel}))^2 + B$ [see Eq. (2.40)], where A and B are a multiplicative constant and the background of the detected signal, respectively. The resulting half widths of ISVs along [110] and [1$\bar{1}$0] directions as functions of $\epsilon_{\parallel}$ are plotted in Fig. 4.6. It is obvious that the dots are elongated along [1$\bar{1}$0] direction as also reported for buried InAs QDs grown at similar conditions in Ref. [SKS03].

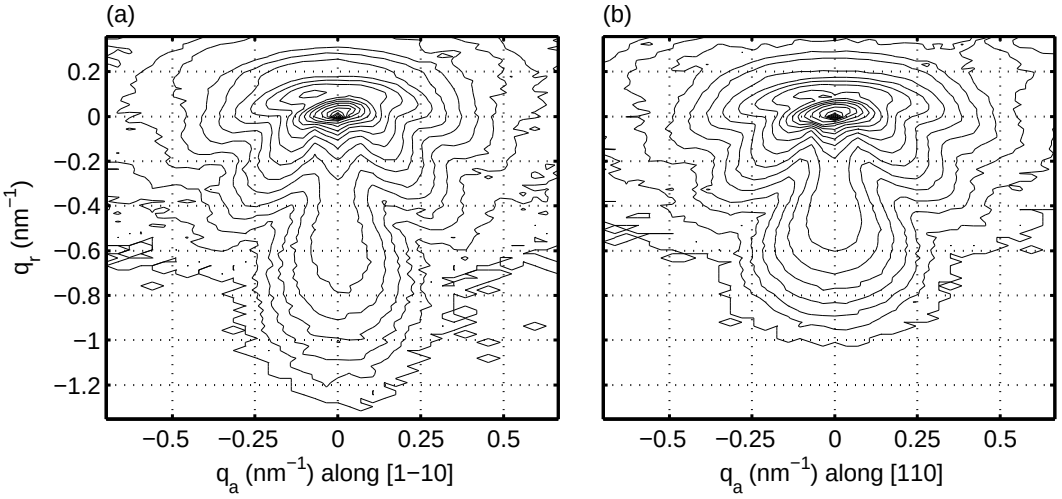

Figure 4.5. Measured GID maps close to the (a) (440) and (b) (4$\bar{4}$0) reflections, the contour step is $10^{0.25}$. The angular axes q_{a} are along the [1$\bar{1}$0] and [110] directions in panels (a) and (b), respectively.

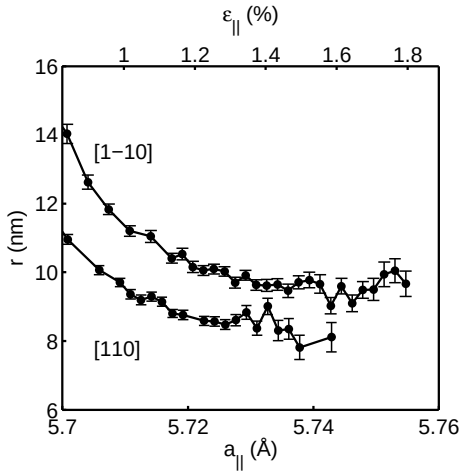

Figure 4.6. Half widths of the ISVs R along [110] (bottom curve) and [1$\bar{1}$0] (top curve) as functions of the lateral strain $\epsilon_{\|}$ obtained from the cuts through the RSMs in Fig. 4.5.

We observed a strain value of $\epsilon_{\|} = 1$ % at the bottom of the QD in most of the strain simulations mentioned above. Thus, for further strain simulations with our rotationally symmetric model we fixed the bottom dot radius to be $R_{\mathrm{dot}} = 10.5$ nm, which is the average of the dot half widths along [110] and [1-10] direction at $\epsilon_{\|} = 1$ % obtained in Fig. 4.6. Varying the height h_{dot} and the In content c_{In} of the model QD we again searched for combinations which lead to $\epsilon_{\|} = 2.6$ % at $z = -8$ nm, as obtained from the cusps in the q_{z} profiles. The resulting h_{dot}, c_{In} combinations are plotted in Fig. 4.7: The average In content in the dots is around $c_{\mathrm{In}} = 70$ %.

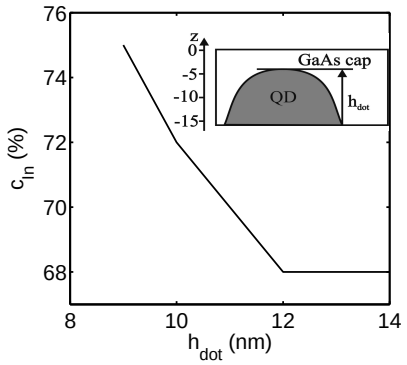

Figure 4.7. Combinations of h_{dot} and c_{In} which lead to an ISV of lateral strain $\epsilon_{\|} = 2.6$ % at $z = -8$ nm for QD radius $R_{\mathrm{dot}} = 10.5$ nm. The inset shows the definition of the $z-$axis.

From the X-ray analysis, we can conclude that the effective radius of the buried QDs reduced from 30 nm observed in AFM for uncapped dots to (10.5 ± 3) nm during capping and annealing, while the In content is roughly comparable to the average value for uncapped islands [KML$^+$01]. However, the content is rather high compared to $c_{\mathrm{In}} = 30$ % reported for buried QDs in Ref. [FHZ03], but in good agreement to $c_{\mathrm{In}} = 65$ % reported in Ref. [ZDM$^+$01]. We believe that such a high In content is explained by the fact that during capping with GaAs the substrate temperature was reduced to 460°C, suppressing InAs/GaAs interdiffusion considerably.

TEM images taken on QDs of the investigated sample show QD width of 28.5 nm (see Fig. 4.8), which is 35 % larger than that obtained from X-ray analysis. However, both the

chemical and strain fields influence the TEM image contrast. The height h_{dot} obtained from TEM is approximately the same as that obtained from X-ray analysis.

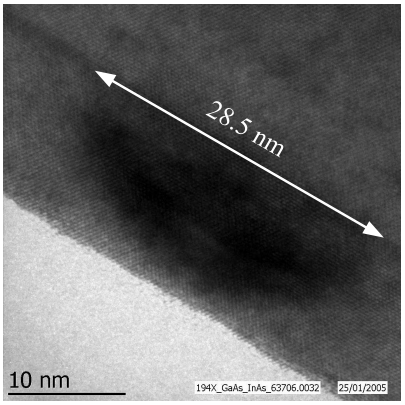

Figure 4.8. TEM image of one of the investigated QDs. Taken by Prof. F. Schäffler, JKU Linz.

The room temperature PL spectra measured on the investigated sample is shown in Fig. 4.9(a). A line from the InAs QDs is observed at an energy of 0.93 eV. Bandstructure calculations of the QDs were performed with the NEXTNANO^3 code developed in the group of Prof. P. Vogel at the Technical University of Munich [nex]. For QDs of height $h_{\mathrm{dot}} = 12$ nm, radius $R_{\mathrm{dot}} = 10.5$ nm, and In content $c_{\mathrm{In}} = 70$ % rather high PL transition energy of 1.05 eV is calculated (see Fig. 4.9(b)). The PL calculations predict larger QD radius and/or higher In content than that obtained from the X-ray analysis.

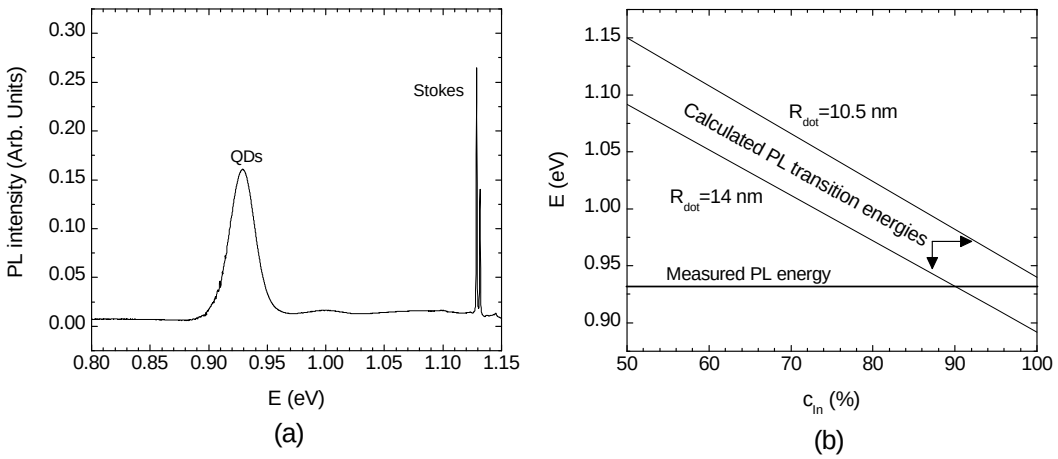

Figure 4.9. (a) PL spectra of the investigated sample taken at room temperature. Measured by Prof. J. Humlíček, MU Brno. (b) PL transition energies obtained from band structure calculations of the InAs QDs. The PL energy is plotted as function of the In content in the dots c_{In}. Calculations were performed for the QD height of $h_{\mathrm{dot}} = 12$ nm and the dot radii of $R_{\mathrm{dot}} = 10.5$ nm (value obtained from X-ray analysis) and $R_{\mathrm{dot}} = 14$ nm (value obtained from TEM). The measured PL transition energy of 0.93 eV is indicated by a horizontal line. Calculations performed by Dr. T. Fromherz, JKU Linz.

The decrease of the dot radius determined from the X-ray analysis and TEM seems strange. We believe that during capping, the islands are actually interdiffused with GaAs

in the outer regions, while a In-rich 'core' remains. Only this core is captured by the cusp analysis, as only for the core the assumptions of flat ISVs with strain values that are not present outside the islands are valid. As we use a simple QD model with a constant composition, and trim the model to reproduce the strain-height dependence found in the cusp analysis, we obtain rather small QDs.

Finally, Fig. 4.10 shows the calculated strain field $\epsilon_{\|}$ in the [100], [001] plane for QD of height 12 nm, bottom radius 10.5 nm and In content 68 %, which were obtained from our analysis. Obviously, the evolution of the strain in the QDs and the surrounding capping layer is not monotonic along the growth direction z. This causes the blurring of the cusps in the q_z-profiles as discussed above.

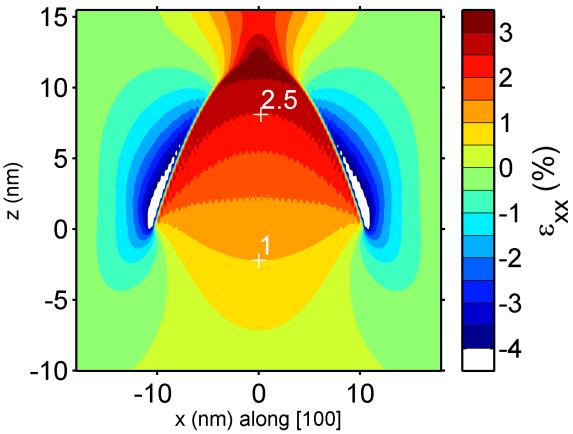

Figure 4.10. Lateral strain distribution within and around a QD of radius $R_{\mathrm{dot}} = 10.5\,\mathrm{nm}$, height $h_{\mathrm{dot}} = 12\,\mathrm{nm}$ and with an In content of $c_{\mathrm{In}} = 68$ %.

4.1.4 Conclusion

The generalized ISSM, introduced in Chap. 3, is applied for an analysis of buried InAs/GaAs QDs. As the strain in buried QDs does not vary monotonically with the height, the method is limited to the highly strained 'core' of the QDs. Hence for a full characterization it is necessary to additionally perform strain calculations using a model of the QDs, but the results from iso-strain scattering yields a good starting point and additional constraints for the model fitting procedure. It can be expected that the method is suited for buried QDs with a high strain, i.e., for systems with sufficiently low interdiffusion and high mismatch, for example InAs/GaAs or InN/GaN.

The radius of the studied QDs reduced from 30 nm, observed for uncapped dots, to (11 ± 3) nm during capping and annealing. The In content decreased to (70 ± 2) %. QDs are elongated along the $[1\bar{1}0]$ in-plane direction.

Acknowledgements

The sample was grown and the AFM analysis was performed by Dr. S. Kiravittaya (MBE group, Max Planck Institute Stuttgart, Germany). The TEM images were taken by Prof. F. Schäffler (JKU Linz, Austria). PL measurements were carried out by Prof. J. Humlíček

and Dr. J. Fikar (MU Brno, Czech Republic). The PL simulations were performed by Dr. T. Fromherz (JKU Linz).

4.2 Laterally ordered and unordered QDs in a 11-fold InAs/GaAs QD multilayer

4.2.1 Introduction

The self assembled growth of nano-islands is governed by statistics so that there is little control over their lateral positions. In addition, nano-islands exhibit variations in size, shape and composition with a corresponding inhomogeneous broadening of the electronic density of states. All these factors can pose significant problems for device applications. Ordering of nano-islands in two-dimensional (2D) lattices, their stacking in multilayers or even ordering in nano-island three-dimensional (3D) crystals has been found to yield improvements in the size uniformity [XJX$^+$99, PBWR03, ZB04, KRS06].

A control of nano-islands sites can be achieved by growing islands on a prepatterned substrate [SJPL$^+$00, JLW00, SKN$^+$02, BZS03, YLL04, ZB04, KRS05]. By stacking island layers separated by spacer layers, such a (2D) island arrangement can be extended into a three-dimensional (3D) island "crystal" using appropriate growth conditions. The buried dots act as stressors in a matrix of different lattice parameter and determine the preferential nucleation sites in the next island layer [SHPB98, KHS04, ZCS$^+$04, KHS05, Spr05]. 3D ordered nano-island crystals might be of interest for certain opto-electronic devices, e.g., photonic crystal structures and gain-coupled distributed feedback lasers. However, the properties of nano-islands grown in periodic holes differs from those of islands grown on a flat substrate at otherwise identical conditions [ZB04, KRS05]. Furthermore, a substantial change of island properties during capping mainly due to interdiffusion with the spacer material is expected [GMRS$^+$97, WKSL01, JKBJ01, SKS03]. Hence a study of such 3D island crystals is of particular interest.

In this section we report on a study of the topmost (uncapped) QD layer of 11 stacked layers of laterally ordered and unordered QDs. We have measured X-ray diffuse scattering on the QDs in GID geometry. Though the scattering took place on both the ordered and the unordered QDs, we were able to extract structural information on each class of the QDs separately from measured data. For the ordered QDs, the presented X-ray scattering analysis is designed to provide a quantitative estimate of the mean deviation of QD positions from the perfect 2D lattice sites on a macroscopic portion of the sample surface. Such fluctuations of lateral QD positions arise due to imperfections in the vertical stacking in QD multilayers [KMP$^+$99, SRB$^+$00, HSS$^+$00]. Additionally, the mean deviation of QD positions was also obtained from AFM images of the topmost QD layer. The results obtained by both methods are comparable.

Two direct methods of obtaining the strain distribution in uncapped QDs from X-ray measurements in GID geometry are commonly used: (i) Purely from X-ray data as described in Sec. 2.3, i.e., the widths of the iso-strain volumes (ISVs) are determined

from the form factor oscillations in the angular scans and the elevations of ISVs above the sample surface δz are obtained from the measured q_z intensity profiles [KML$^+$00, KML$^+$01, HLH$^+$03, KMR$^+$05]. (ii) Widths of ISVs determined from the X-ray angular scans are associated with certain heights δz within the islands using a cross-section profile of the islands from AFM images, linking the elevations δz of ISVs with their in-plane strain $\epsilon_{\|}$ [MPMRM$^+$02, SSZ$^+$03, MKMR$^+$03, MMPKC04, SSH$^+$05]. Both methods were applied for characterization of investigated QDs. The results of the respective methods differ substantially. We compare the resulting strain distribution with strain calculations in literature and discuss appropriateness of the respective methods.

4.2.2 Experiment

Sample growth and structure

The investigated sample was grown by MBE on a GaAs (001) substrate. An e-beam defined pattern was etched into the substrate, resulting in a regular array of holes. The size of the patterned area was 100×100 μm^2. The holes formed a rectangular grid having a spacing of 198 nm along two orthogonal $\langle 100 \rangle$ directions. Details of the pattern preparation can be found in Ref. [KHS04]. An 18 ML GaAs buffer layer was grown on the patterned surface. Then, the first InAs QD layer was grown at 470°C, followed by a spacer layer consisting of a sequence of GaAs/GaAlAs/GaAs layers with a total thickness of 15 nm. During spacer layer growth, the substrate temperature was increased to 500°C. Finally, 10 InAs QD layers separated by GaAs/GaAlAs/GaAs spacer layers were grown. The topmost QD layer was left uncapped. The amounts of InAs deposited for the first QD layer and the following 10 QD layers were 1.5 ML and 1.8 ML, respectively. The growth rate of InAs, GaAs, and $Al_{0.4}Ga_{0.6}As$ were 0.01, 0.6, and 1.0 ML/s, respectively. The structure of the sample is shown in Fig. 4.11(a).

AFM

Atomic force microscopy (AFM) images were taken immediately after finishing the growth. The AFM measurements were performed using a Nanoscope IIIa in tapping mode. One of the AFM images on the patterned area of the sample is shown in Fig. 4.11(b). The QDs form a perfect 2D array with a low number of defect-sites. In the defect-sites predominately double-dots were formed [KHS04, KHS05]. We clearly see that the QDs are located on elevated structures (ridges) spread along the $[1\bar{1}0]$ direction. The heights and widths of the ridges are 3 nm and 100 nm, respectively. The ridges originate from an overlap of the mound structures that develop during overgrowth of large InAs QDs grown at low growth rate with GaAs [JKBJ01, SKS03].

Besides the ordered dots on the patterned part of the sample also unordered dots were observed on the unpatterned part [see Fig. 4.11(c)]. The unordered dots are also located on elevated structures spread along $[1\bar{1}0]$. In contrast to the patterned part of the sample, the structures do not form long continues ridges.

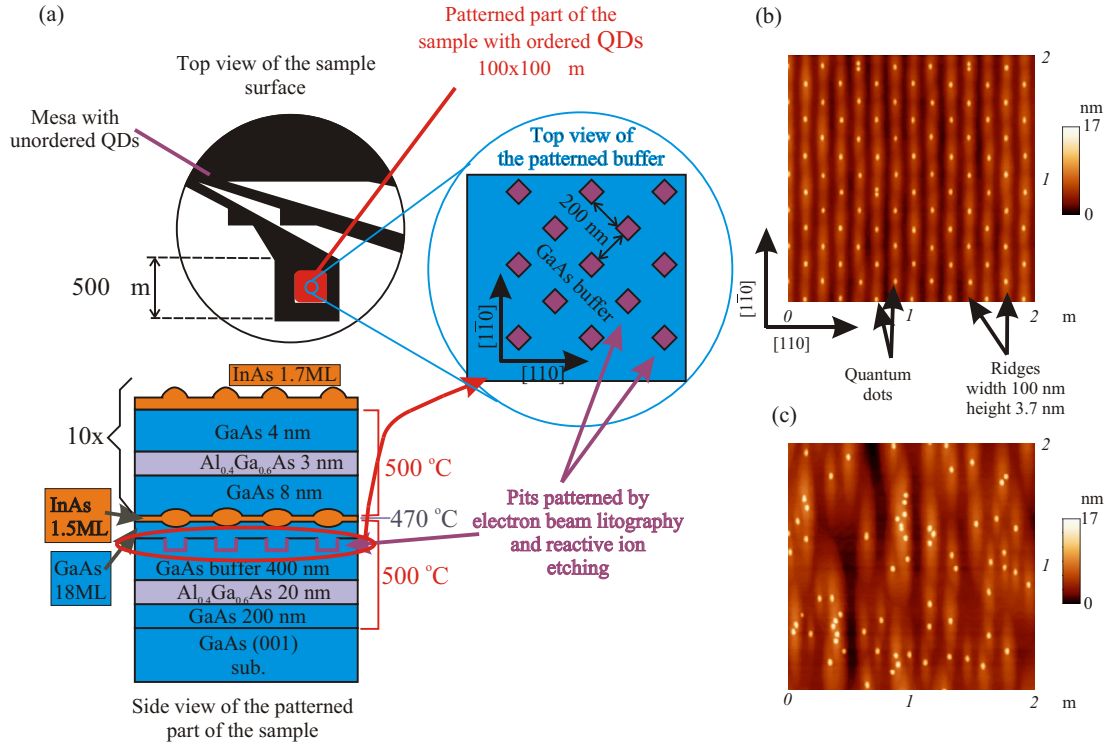

Figure 4.11. (a) Nominal structure of the investigated sample. AFM image of the topmost QD layer (b) above the patterned part of the sample and (c) above the prepatterned part.

X-ray measurements

X-ray measurements were carried out at beam line ID01 at the European Synchrotron Radiation Facility (ESRF), Grenoble (France), with an X-ray energy of $E = 12.33$ keV. The measurements in GID geometry (see Fig. 2.5) were performed close to the $(\bar{2}\bar{2}0)$ and weak $(0\bar{2}0)$ and $(\bar{2}00)$ in-plane Bragg reflections. The X-ray energy was chosen above the K edge of As ($E = 11.867$ keV) to suppress scattering from the GaAs matrix in the weak reflections (see Sec. 2.4 and Ref. [SSC+02]). We used slits of a flight tube behind the sample and one slit (slit 1) before the sample to restrict the beam and detect X-rays scattered dominantly from the ordered QDs (see Fig. 4.12). The distance between the sample and slit 1, and the sample and 1st slit of the flight tube were approximately 10 cm. The widths of the slit 1 and 1st slit of the flight tube were 0.1 mm. The width of the 2nd slit of the flight tube was 0.2 mm and the length of the flight tube was 1 m.

Lateral satellites due to the lateral ordering of QDs were observed in the vicinity of all probed reflections. We measured radial maps, i.e., reciprocal space maps in (q_r, q_z) plane along $q_a = 0$, and angular maps through the lateral satellites, see the scheme in Fig. 4.13. The intensity along q_z direction is distributed into vertical satellites due to the vertical stacking of QDs. As a result, we observed a 2D grid of satellites in each type of scans. The X-ray data hence confirm the successful growth of a 3D QD crystal above the patterned part of the sample. Though the size of the beam was restricted by the slits, scattering on unordered QDs on the unpatterned part of the sample led to some continues diffuse

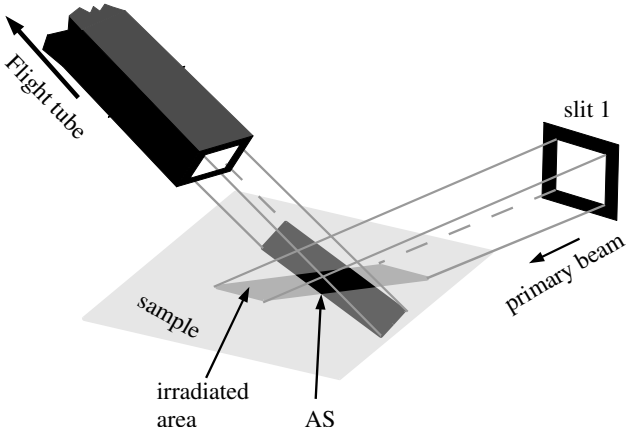

Figure 4.12. Slit setup used to restrict detected signal to scattering from ordered dots on an area of $100 \times 100\ \mu\mathrm{m}^2$. AS denotes the area from which the signal is effectively collected.

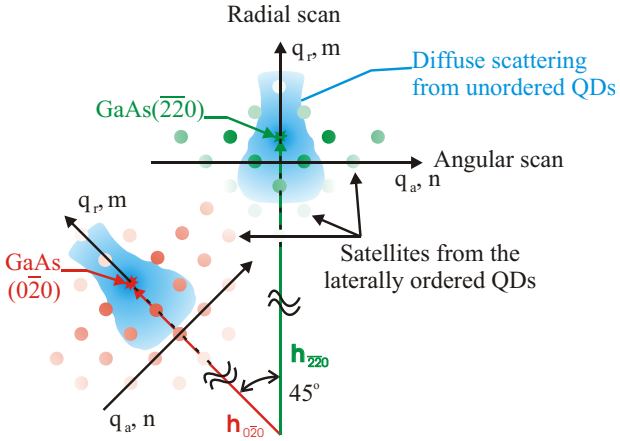

Figure 4.13. Schema of the intensity distribution around GaAs $(0\bar{2}0)$ and $(\bar{2}\bar{2}0)$ Bragg reflections projected to the $(q_\mathrm{r}, q_\mathrm{a})$ plane, parallel to the sample surface. Radial scans and one of angular scans are indicated for each reflection. Satellites order along q_r and q_a are denoted by m and n, respectively, in the text.

scattering between the lateral satellites. However, as we show in the subsection 4.2.4, we are able to separate structural information on both classes of QDs from the measured data.

4.2.3 Theory – QD position correlation

The correlation properties of dot positions can be obtained by direct observation using microscopy (AFM, TEM) or from X-ray scattering. For X-rays, the positions and the widths of the maxima of the scattered intensity in reciprocal space are determined by the interference function Eq. (2.33) containing relative dot positions $\mathbf{R}_m - \mathbf{R}_n$. Here, we develop a model describing the position correlations of the ordered dots and derive formulae for determining the parameters of the model from X-ray scattering and AFM images.

We concentrate only on correlations of QD positions within one QD layer. From the growth mechanism and growth conditions for the dots above the prepatterned substrate it follows that a long-range order model for the QD positions is applicable. Within this

model one assumes that QDs are displaced from the ideal lattice sites by random shifts $\mathbf{U}_{j,l}$. Therefore, the in-plane position of the (j,l)th dot is

$$\mathbf{R}_{j,l} = j\mathbf{T}_1 + l\mathbf{T}_2 + \mathbf{U}_{(j,l)}, \tag{4.1}$$

where $\mathbf{T}_1$, $\mathbf{T}_2$ are translation vectors of the dot lattice (see Fig. 4.14). The displacements of dots are mutually independent and the mean displacement is 0, i.e., $\left\langle \mathbf{U}_{(j,l)} \cdot \mathbf{U}_{(m,n)} \right\rangle = \delta_{j,m}\delta_{l,n} \cdot \text{const.}$ and $\left\langle \mathbf{U}_{(j,l)} \right\rangle = 0$. The brackets $\langle \cdots \rangle$ denote averaging over all possible configurations of the entire ensemble of dots.

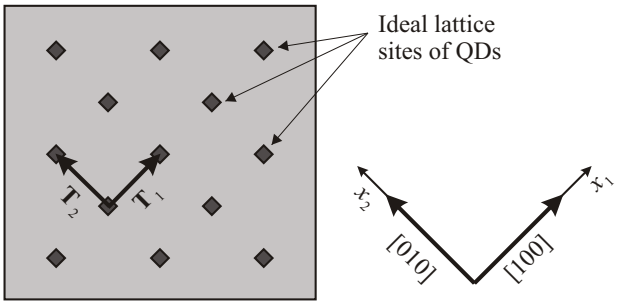

Figure 4.14. To the definition of the in-plane translation vectors $\mathbf{T}_1$ and $\mathbf{T}_2$ of the dot lattice and the orientation of the coordinate system.

We assume that the displacements of the dots along the x_1 and x_2 axes are mutually independent and that they obey the same Gaussian probability function

$$w_s(U_s) = \frac{1}{\sqrt{2\pi}\sigma} \exp(-\frac{U_s^2}{2\sigma^2}),\ s = 1, 2. \tag{4.2}$$

The root mean square displacement σ can be determined both from X-ray scattering and AFM images as described below.

X-ray scattering — interference function

For scattering on ordered QDs, the X-ray intensity distribution is modulated by the interference function of Eq. (2.33). By inserting Eqs. (4.1) and (4.2) into Eq. (2.33) we obtain a formula for the interference function

$$\begin{aligned} P(\mathbf{q}) &= N + |w^{\mathrm{FT}}|^2(\mathbf{q}) \sum_{j,j'} \sum_{l,l'} \left[\exp(\mathrm{i}q_1 T_1 (j - j')) \exp(\mathrm{i}q_2 T_2 (l - l')) - \delta_{j,\,j'}\delta_{l,\,l'} \right] \\ &= N(1 - |w^{\mathrm{FT}}|^2(\mathbf{q})) + |w^{\mathrm{FT}}|^2(\mathbf{q}) \left(\frac{\sin(N_1 q_1 T_1/2)}{\sin(q_1 T_1/2)} \frac{\sin(N_2 q_2 T_2/2)}{\sin(q_2 T_2/2)} \right)^2, \end{aligned} \tag{4.3}$$

where N_1 and N_2, denote the number of dots along the axes x_1 and x_2, respectively, $N = N_1 N_2$ is total the total number of dots, q_1 and q_2 are the components of $\mathbf{q}$ along the axes x_1 and x_2, respectively,

$$w^{\mathrm{FT}}(\mathbf{q})) = \left\langle \mathrm{e}^{\mathrm{i}\mathbf{q}\mathbf{U}} \right\rangle = \exp(-\frac{q_1^2 + q_2^2}{2}\sigma^2) \tag{4.4}$$

is the characteristic function of the displacement probability distribution $w(\mathbf{U}) = w_1(U_1) \cdot w_2(U_2)$, and $\delta_{j,j'}$ is the Kronecker delta.

The first term in Eq. (4.3) describes the diffuse background and the second term accounts of the satellite maxima. The height of the satellite peaks decreases with increasing $|\mathbf{q}|$ (see Fig. 4.15). The decrease is slower for smaller dispersions of QD positions σ. The widths of the satellite peaks are inversely proportional to the total number of QDs along the respective directions N_1 and N_2. While the height of the satellite peaks is proportional to N^2, the diffuse background is proportional only to N, i.e., the peak to background intensity ratio increases with increasing number of QDs. The diffuse background displays a dip around $q_a = 0$. The width of the dip in q-space is inversely proportional to σ.

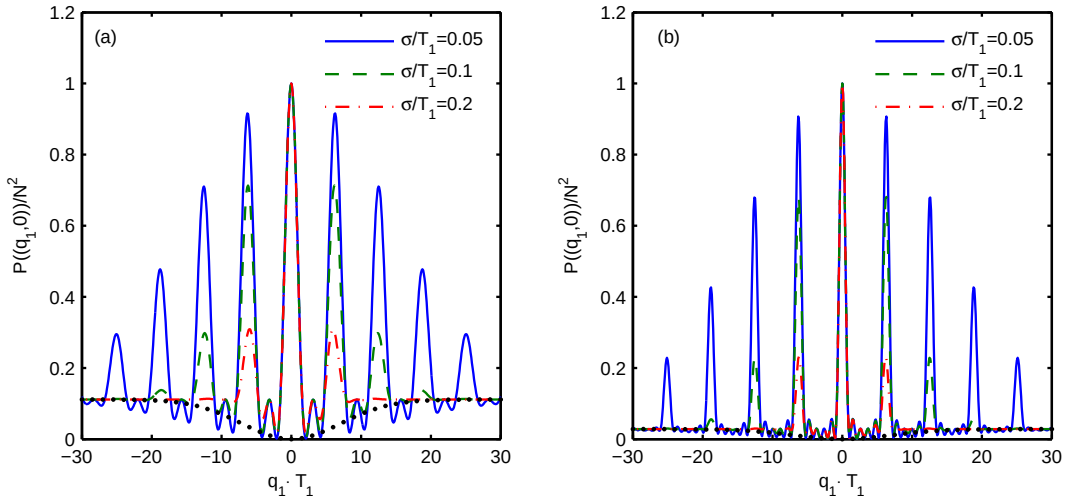

Figure 4.15. Interference function $P(q_1, q_2 = 0)$ [see Eq. (4.3)] plotted for various mean square displacements σ. Numbers of QDs along x_1 and x_2 axes are (a) $N_1 = N_2 = 3$ and (b) $N_1 = N_2 = 6$, respectively. The diffuse background, i.e., the first term of Eq. (4.3), is plotted by dots for $\sigma/T_1 = 0.1$ in each panel.

Determination of σ from AFM images

The root mean square displacement σ can be determined from displacements of individual QDs $U_{(j,l)}$ read out from AFM images. The probability function of the displacement $U = \sqrt{U_1^2 + U_2^2}$ is

$$w'(U) = \frac{1}{\sigma^2} U \exp(-\frac{U^2}{2\sigma^2}), \tag{4.5}$$

as follows from Eq. (4.2). The best unbiased estimate of σ obtained by minimizing the likelihood function

$$f_{\mathrm{L}}(U_{(j,l)}, \sigma) = \frac{1}{\sigma^{2N}} \prod_{\forall j,l} U_{(j,l)} \exp(-\frac{U_{(j,l)}^2}{2\sigma^2}), \tag{4.6}$$

with respect to σ is

$$\sigma = \sqrt{\frac{\sum_{\forall j,l} U_{(j,l)}^2}{2N}}. \tag{4.7}$$

4.2.4 Results and discussion

GID measurements around $(\bar{2}\bar{2}0)$ Bragg reflection

The measurements around $(\bar{2}\bar{2}0)$ in-plane Bragg reflection were performed for an incidence angle of $\alpha_i = 0.155°$, which is smaller than the critical angle of GaAs $\alpha_c = 0.201°$ for the used X-ray wavelength. The penetration depth of the evanescent X-ray wave was only $\Lambda = 3.5$ nm and the scattered signal originated from uncapped QDs dominantly. The radial scan for $(\bar{2}\bar{2}0)$ reflection and the angular scan through the satellite $m = -5$ are shown in Figs. 4.16 (a) and (b), respectively. The intensity distribution in the lateral satellites is elongated along the q_z-axis (so-called crystal truncation rods'). We observe satellite rods up to order $m = -9$ along the radial direction between the GaAs substrate rod at $q_r = 0$ nm^{-1} and the InAs $(\bar{2}\bar{2}0)$ reciprocal space point corresponding to $q_r = -2.1$ nm^{-1} in the radial scan. The other satellites are lost in the diffuse background due to their damping caused by the finite order of the QDs. The intensity integrated along q_z in ranges $\alpha_f \in (0, \alpha_c)$ for angular scans at different q_r positions is plotted in Fig. 4.17(c). Satellites up to order $n = \pm 6$ were observed in angular scans. It is worth to note that the diffuse scattering between the satellites does not display the characteristic dip around $q_a = 0$. Additionally, the central peaks at $q_a = 0$ are only 10−times more intense than the diffuse background while, according to Eq. (4.3), we would expect that the ratio would be approximately 500. We conclude that the diffuse background is due to unintended scattering on unordered dots on the unpatterned area.

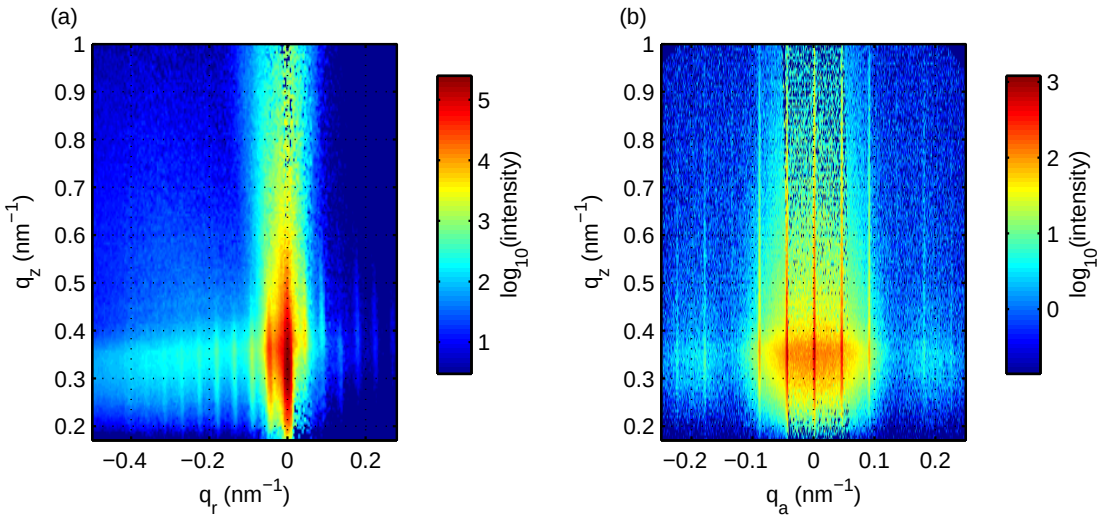

Figure 4.16. (a) Radial scan around $(\bar{2}\bar{2}0)$ in-plane Bragg reflection. (b) Angular scan through the satellite m=-5 of the $(\bar{2}\bar{2}0)$ in-plane Bragg reflection.

Strain distribution along the growth direction

We have performed an iso-strain analysis of the uncapped QDs using the measurements around $(\bar{2}\bar{2}0)$ reflection. First, sections through the measured radial map along q_z-axis

were fitted with the model function Eq. (2.41a) to obtain elevations of the ISVs above the sample surface [see Fig. 4.17(a)]. The q_z sections taken through the satellite rods and between them correspond to the ordered and unordered QDs, respectively. The resulting elevations of ISVs as function of the lateral strain $\epsilon_{\|} = (a_{\|} - a_{\mathrm{Ge}})/a_{\mathrm{Ge}}$ for both kind of dots are plotted in Fig. 4.18(a). For ordered dots, we observed satellites only up to q_r corresponding to strain $\epsilon_{\|} = 1.6$ %, which implies the upper limit of the interval $\epsilon_{\|}$, where values of δz were obtained. In contrast, the diffuse background signal from unordered dots was sufficient to perform the analysis for strains up to $\epsilon_{\|} = 3.1$ %. By inspection of Fig. 4.18(a) ISVs of the same strain seem to be more elevated above the sample surface for ordered dots than for unordered ones. However, the error intervals of $\delta z(\epsilon_{\|})$ for ordered and unordered QDs overlap. AFM images revealed that the ridges on which QDs resides are on average lower for unordered dots and the reference surface with respect to which is the elevation δz determined is not well defined. From this analysis we can not conclude that the unordered and ordered QDs have different strain distribution along the growth direction.

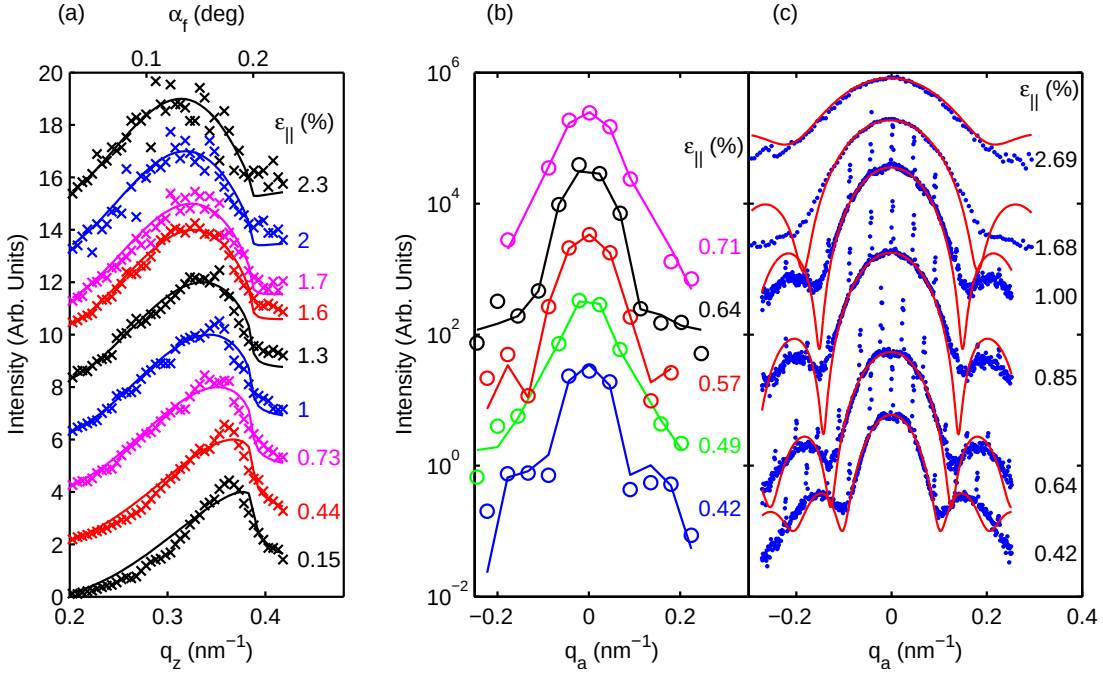

Figure 4.17. Evaluation of the experimental data measured around $(\bar{2}\bar{2}0)$ GaAs Bragg reflection using the ISSM. Experimental data (symbols) were simulated using models mentioned in the text. The best simulations are plotted as solid lines. (a) q_z intensity profiles used to obtain elevations of ISVs above the sample surface for both ordered and unordered QDs. Curves for strains $\epsilon_{\|} = 0.15 - 1.6$ % and $\epsilon_{\|} = 1.7 - 2.3$ % correspond to ordered and unordered QDs, respectively. (b) Amplitudes of the satellite peaks extracted from angular scans. (c) Angular scans integrated along q_z-axis in ranges $\alpha_f \in (0, \alpha_c)$ and fits of the diffuse background originating from unordered QDs. q_z intensity profiles, satellite amplitudes, and angular scans are shown for various q_r positions corresponding to total strains $\epsilon_{\|}$ indicated on the right hand side of each panel.

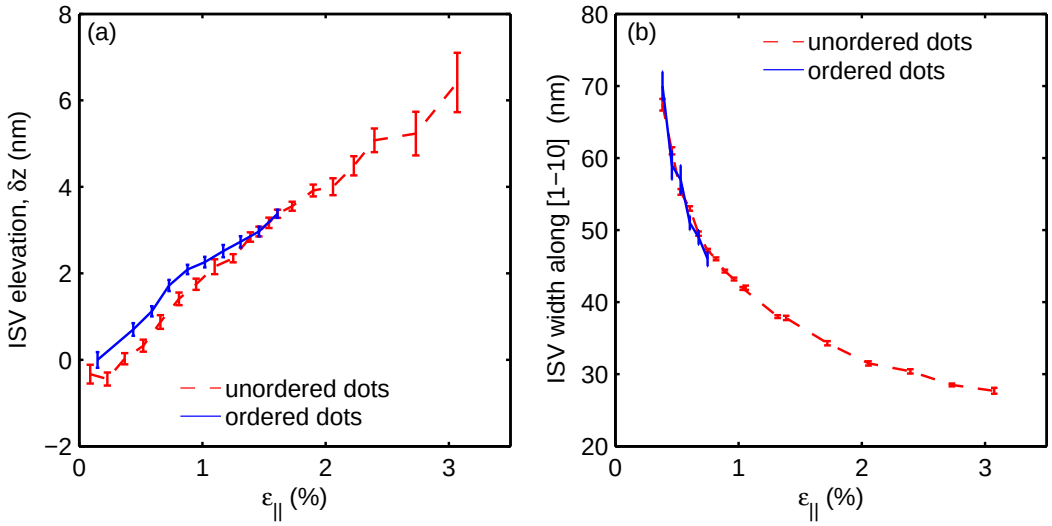

Figure 4.18. (a) Elevations of ISVs above the sample surface as a function of the total strain $\epsilon_{\|}$. (b) Widths of ISVs along $[1\bar{1}0]$ direction as a function of strain. Dependencies for unordered and ordered dots are plotted by the red dashed lines and the solid blue lines, respectively.

Iso-strain analysis of laterally ordered QDs and determination of σ from X-ray measurements

In order to obtain lateral sizes of ISVs for the ordered QDs, we have extracted the amplitudes of the satellite peaks. The satellite peaks in the angular scans integrated along q_z [Fig. 4.17(c)] were fitted with Gaussians superimposed on a sloping background. The amplitudes of the Gaussians for several angular scans at various q_r are plotted in Fig. 4.17(b) as a function of q_a along $[1\bar{1}0]$ direction. The full width at half maxima (FWHM) of the satellites does not depend on the satellite order. An average FWHM of $\Delta q_a = (3.2 \pm 0.2) \times 10^{-3}$ nm^{-1} was observed. The shape of the measured satellite peaks is a convolution of the resolution function of the experimental set-up and of the shape of the satellites of the interference function Eq. (4.3). In our case, the FWHM of the satellites of the interference function can be estimated to be $\Delta q_a \approx 2\pi/(N_1 T_1) \approx 3 \times 10^{-5}$ nm^{-1}, which is much less that the observed value. The shape of the satellites was fully determined by the geometry of the experimental set-up.

The angular variation of the satellite amplitudes was fitted with a model function

$$I(q_a, D, \sigma) = A \left| \frac{\sin(q_a D/2)}{q_a} \right|^2 e^{-q_a^2 \sigma^2}, \tag{4.8}$$

where A is a proportionality constant, D is the width of a ISV along the $[1\bar{1}0]$ direction, and σ is the root mean square displacement of the dots from the 2D lattice sites. While the middle term of Eq. (4.8) $|\sin(q_a D/2)/q_a|^2$ is square of the form factor of the ISV [Eq. (2.40)], the last exponential term is the damping due to the QD displacements [Eqs. (4.3) and (4.4)]. The best simulations for several angular scans are shown in Fig. 4.17(b) and the

resulting widths $D(\epsilon_{\|})$ of ISVs are plotted in Fig. 4.18(b) by the solid line. The root mean square displacement of the dots from their lattice sites is $\sigma = (7.0 \pm 0.5)$ nm.

Determination of σ from AFM images

In order to obtain the root mean square displacement σ of the uncapped ordered QDs from their ideal in-plane lattice site positions, we read out the positions of the QDs in the AFM image in Fig. 4.11(b). Then we matched an ideal lattice (shown in Fig. 4.14) with the experimental dot positions. We fitted the lengths of the translation vectors T_1, T_2, their orientations and the origin of the coordinate system to minimize the root mean square displacement defined in Eq. (4.7). A comparison of the resulting ideal dot lattice and the experimental positions of the dots is shown in Fig. 4.19. We did not involve the double-dots in Fig. 4.11(b) into the analysis. The root mean square displacement of the dots obtained from this analysis is $\sigma = (9 \pm 3)$ nm, which is in a good agreement with $\sigma = (7.0 \pm 0.5)$ nm obtained from the analysis of the X-ray data.

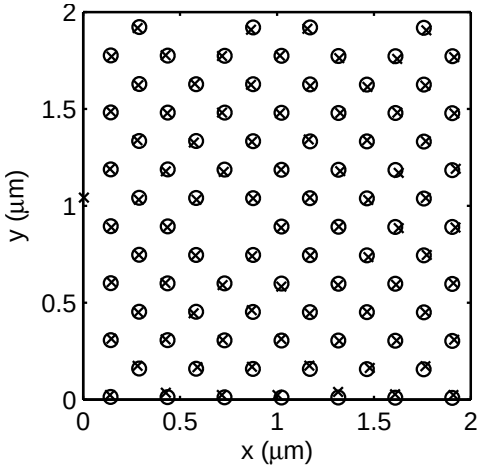

Figure 4.19. QD positions read out from the AFM image shown in Fig. 4.11(b) (crosses) and the sites of the optimized lattice (circles).

Iso-strain analysis of laterally unordered QDs

Lateral sizes $D(\epsilon_{\|})$ of ISVs for unordered QDs were obtained by fitting of the diffuse background in the integrated angular scans with a model function $A\,|\sin(q_a D/2)/q_a|^2$ [see Fig. 4.17(c)]. Here, we did not used any interference term, because the dot positions are random and the scattered intensity is proportional to the scattering from one dot. The resulting lateral sizes of ISVs are plotted in Fig. 4.18(b) by the dashed red line. Obviously there is no substantial difference between the lateral sizes of equally strained ISVs for ordered and unordered QDs. As already mentioned, we do not observe any significant difference in strain distribution along the growth direction [Fig. 4.18(b)] for both classes of QDs as well. Hence, we conclude that the ordered and the unordered QDs have approximately the same size and shape.

We have reconstructed the strain distribution within a section through the center of an average QD on the unpatterned area of the sample in two ways: (i) We combined elevations

of the iso-strain volumes δz and of the widths of the ISVs obtained from the above discussed analysis. The resulting strain distribution is plotted as the filled area in Fig. 4.20(a). Additionally, an averaged QD profile obtained from an AFM image analysis is plotted by the red solid line in Fig. 4.20(a) together with the error interval (dashed green line). The dot profile results from averaging in the AFM image, shown in Fig. 4.11, performed over line-scans along $[1\bar{1}0]$ direction through the centre of 10 QDs on the unpatterned part of the sample. (ii) We associated widths $D(\epsilon_{\|})$ of ISVs determined from the ISSM analysis with certain height $\delta z(D)$ within the dots using the averaged QD profile obtained from the AFM image. Elevations of ISVs were obtained as a function of in-plane strain $\delta z(\epsilon_{\|})$ in this way [see Fig. 4.21(b)]. The resulting strain distribution is plotted in Fig. 4.21(a). For both methods (i) and (ii), we did not obtain any information on the most strained top part of the dots, because the volumes of the corresponding ISVs are small and the scattered signal was too weak.

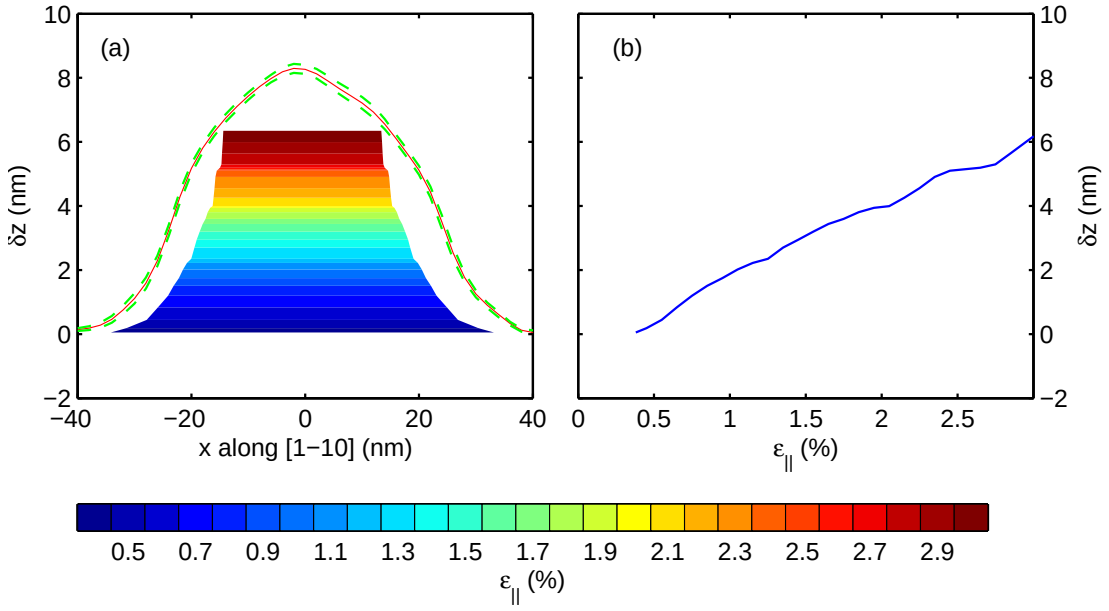

Figure 4.20. (a) A comparison of a real space strain map for unordered QDs obtained by ISSM (filled area) and of an averaged AFM linescan through the center of unordered QDs along $[1\bar{1}0]$ direction (solid red line). Strain within the QD is colourscaled. Error band of the dot shape obtained from the AFM linescan analysis is indicated by green dashed lines. (b) Elevation of ISVs above the sample surface as a function of the in-plane strain relative to GaAs substrate.

The dot size in Fig. 4.20(a) obtained purely from the X-ray data analysis by the method (i) does not match the size obtained from the AFM image analysis. The dot base diameter determined from X-rays is by 11 nm smaller than the diameter determined from AFM. The slope of the sidewalls is the same for the X-ray and AFM analysis in the bottom part of the dot (for $\delta z < 4$ nm). It should be noted that the lateral sizes of dots measured by AFM are upper bounds due to the tip effect [GLX+98]. Additionally, while AFM is sensitive to the morphology of the dots, X-ray diffraction probes the crystalline part of QDs. For InAs QDs, the dot surface is usually oxidized and amorphous. The tip effect

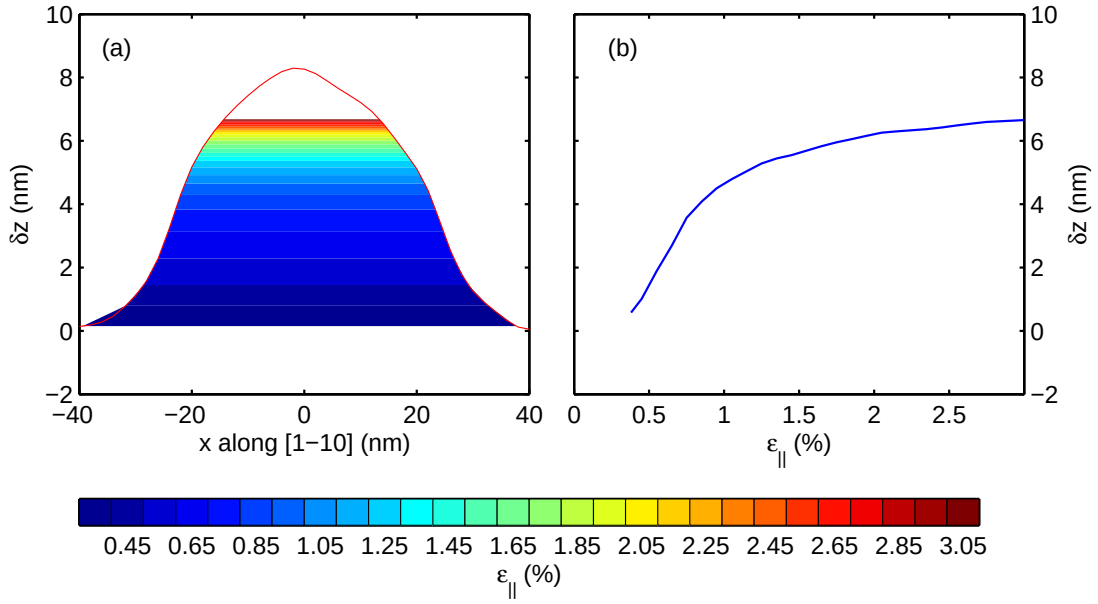

Figure 4.21. (a) Real space strain map for unordered QDs obtained by combining widths of the iso-strain volumes extracted from X-ray data and the dot shape extracted by averaging AFM linescans through the center of unordered QDs along $[1\bar{1}0]$ direction (solid red line). (b) Elevation of ISVs above the sample surface as a function of the in-plane strain relative to GaAs substrate.

can be neglected with respect to the large size of the investigated QDs. We attribute the difference between the QD diameters determined from the X-ray and AFM measurements to an amorphous oxide layer of thickness 5 nm. QDs grown at similar conditions and of similar morphology were observed by Krause et al. in Ref. [KMR$^+$05]. The diameter of the crystalline QD core smaller by approx. 10 nm than that of the morphological diameter, determined from GISAXS and AFM, is reported in this reference in a perfect agreement with the presented results.

The dependence of the in-plane strain $\epsilon_{\|}(\delta z)$ along the growth direction obtained from fitting of the q_z-sections through the radial scan (method (i)) is linear [Fig. 4.20(b)]. The maximum strain at top of the dot obtained from the linear extrapolation is $\epsilon_{\|} = 3.7$ %. The linear dependence $\epsilon_{\|}(\delta z)$ is consistent with strain calculations performed by Nabetani et al. for uncapped InAs QDs using the valence force-field method [NMSS05] (see Fig. 4.22). In contrast, we observe a slow increase of in-plane strain $\epsilon_{\|}(\delta z)$ for $z \in \langle 0, 4 \rangle$ nm and a high strain gradient for $\delta z > 4$ nm in Fig. 4.21(b), where the strain profile was obtained by the method (ii). Such a strain profile can occur if there is a change in the gradient of In content in the dots along the growth direction. In particular, the In content gradient should be higher in the upper part of QDs. Nevertheless, we did not get any information on the In content for these dots. The dot profile obtained from AFM should be corrected for the finite radius of the AFM tip and the thickness of the oxide layer on surface of the island should be subtract from the measured thickness, when an AFM profile is combined with widths of ISVs according to the method (ii).

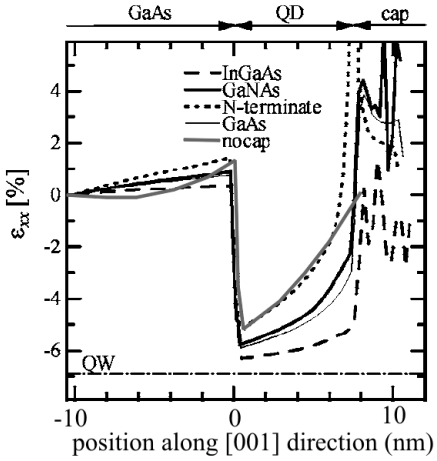

Figure 4.22. Line profiles of the in-plane strain ϵ_{xx} along the growth direction in InAs QDs with different cap (see legend). Local in-plane strain is plotted in this case. The dot dash line at $\epsilon_{xx} = -7$ % corresponds to lattice mismatch between GaAs and InAs. Calculation were performed by valence-force field method. The diameter and height of the dot of 72 nm and 24 nm, respectively, and pure InAs composition were considered in the calculation. From Ref. [NMSS05].

GID measurements around (200) **Bragg reflections**

Three of the measured angular maps for $(\bar{2}00)$ and $(0\bar{2}0)$ reflections are shown in Figs. 4.23 (a-c). In this case we used an incidence angle of $\alpha_\mathrm{i} = 0.23°$, which is larger than the critical angle. Because the penetration depth is $\Lambda = 24$ nm, buried QD layers are irradiated and we observe vertical satellites aligned along the q_z-axis in the RSMs. The satellite alignment along q_z implies that the ordered QDs are stacked along the growth direction. Sheets of continues diffuse scattering along q_a originate from laterally unordered QDs. The sheets are periodically distributed along q_z, which implies vertical stacking of laterally unordered QDs in columns. The weak maxima between the angular satellites $n = 0$ and $n = 1$, which are observed in all angular scans shown in Fig. 4.23, is the analyser streak.

There is an obvious asymmetry of the intensity distribution with respect to $q_\mathrm{a} = 0$ in all angular scans. The angular satellites $n = \pm 3$ are the most intensive for the angular scan through the radial satellites $m = -3$ close to $(0\bar{2}0)$ and $(\bar{2}00)$ GaAs reflections in Figs. 4.23(a) and (b), respectively. For the angular scan through the radial satellite $m = -2$ in Fig. 4.23(c), angular satellite $n = 2$ is the most intensive. As a rule, angular satellites of the order $n = \pm m$ are enhanced in all observed angular scans through radial satellites of orders m. The intensity profiles along q_a are exactly flipped with respect to axis $q_\mathrm{a} = 0$ in angular scans through equivalent radial satellites of $(0\bar{2}0)$ and $(\bar{2}00)$ GaAs reflections. This fact is demonstrated in Fig. 4.23(d), where we show the intensity integrated along q_z for the angular scans through the satellites $m = -3$ of $(0\bar{2}0)$ and $(\bar{2}00)$ GaAs reflections.

The enhancement of the satellites of the order $m = \pm n$ and the asymmetry of the intensity distribution is due to the scattering on ridges observed in AFM images [Figs. 4.11(b) and (c)]. If there were only ridges aligned along the $[1\bar{1}0]$ direction distributed periodically with the period $L = T_1/\sqrt{2}$ along the [110] direction in the analyzed sample, we would have observed a series of satellites of the substrate peak spread along the $[1\bar{1}0]$ direction and periodically distributed along the [110] direction in the $(q_\mathrm{r}, q_\mathrm{a})$ plane of the reciprocal space (see Fig. 4.24). The period would be $\Delta Q_{[110]} = 2\pi/L$. For our sample, the inter-

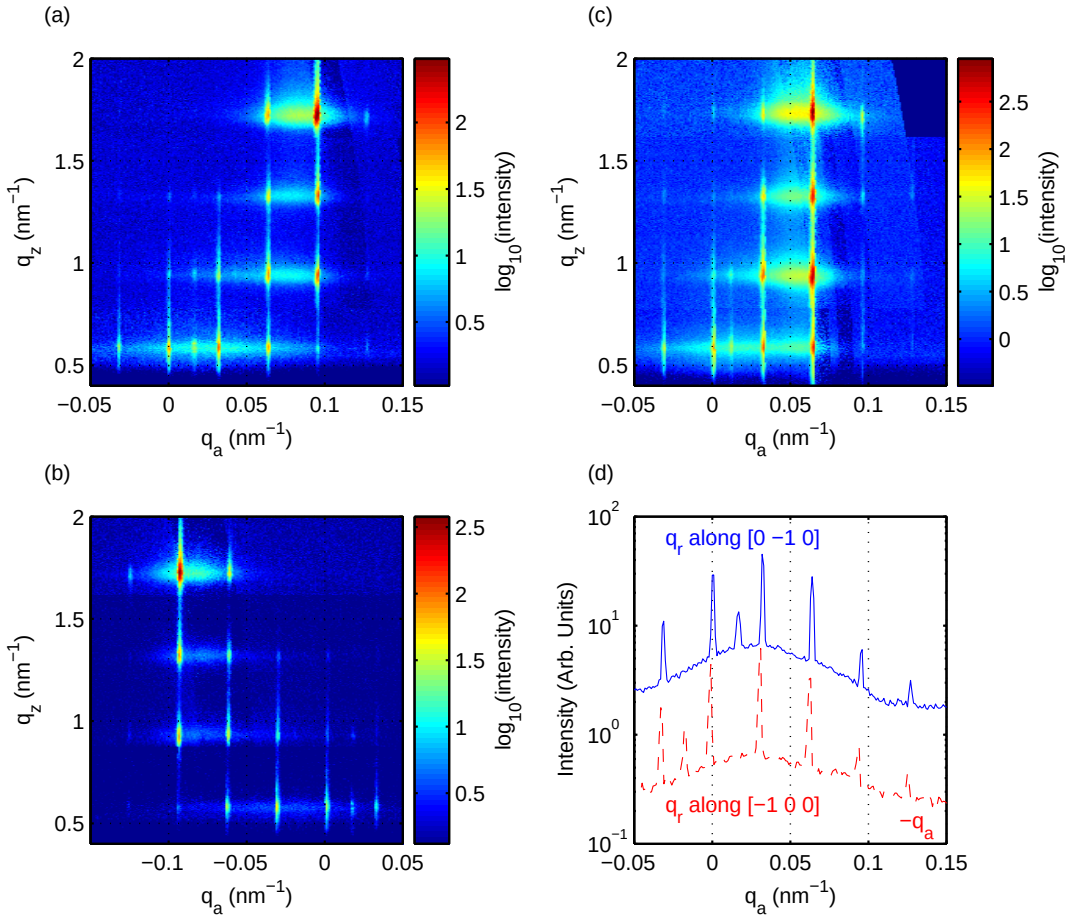

Figure 4.23. (a) and (b) angular scans through the satellite $m = -3$ of the $(0\bar{2}0)$ and $(\bar{2}00)$, respectively, GaAs Bragg reflections. (c) angular scan through the satellite $m = -2$ of the $(0\bar{2}0)$ Bragg reflection. (d) comparison of the integrated intensity of the angular scans through the satellite $m = -3$ of the $(0\bar{2}0)$ (blue solid line) and $(\bar{2}00)$ (red dashed line) GaAs Bragg reflections. The intensity was integrated over the first vertical maximum in a range $q_z \in (0.53, 0.65)$ nm^{-1}. The intensity for $(\bar{2}00)$ Bragg reflection is plotted as a function of $-q_a$ to highlight the mirror symmetry of the intensity distribution in angular scans with respect to the (110) plane.

ference of X-rays scattered on the QDs and the ridges results in an enhancement of the satellites lying on a line going through the GaAs substrate peak along [110] direction.

4.2.5 Conclusion and outlook

Conclusion

Iso-strain scattering was applied to obtain structural information, i.e., shape, size, and strain distribution, of the topmost QD layer of an 11-stack multilayer of laterally ordered and unorder QDs. Though X-ray scattering signals from both the ordered and the unordered QDs were mixed in the measured X-ray data, we were able to extract structural information on each class of QDs separately. Additionally, we have presented a method to determine the mean deviation of QD positions from the perfect 2D lattice sites from X-ray

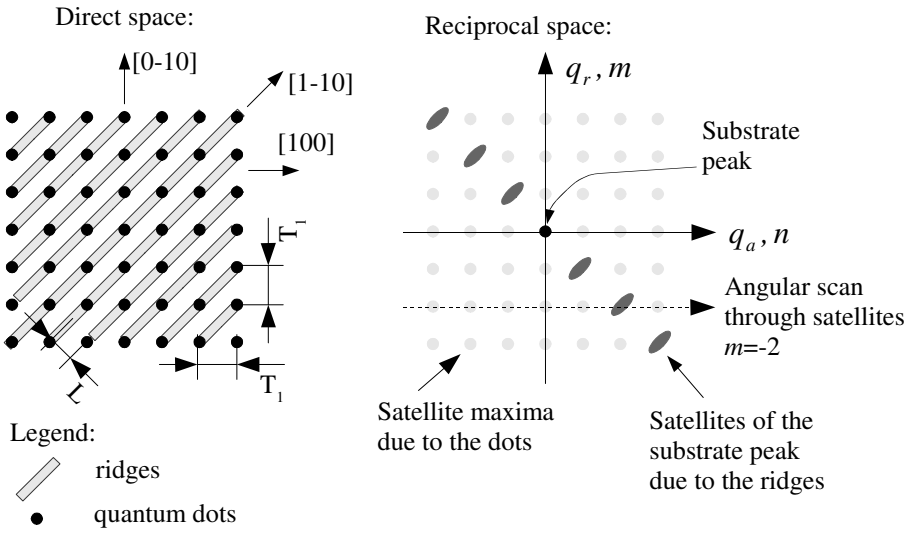

Figure 4.24. Explanation of the asymmetry of the intensity distribution with respect to $q_{\mathrm{a}} = 0$ in angular maps.

scattering on ordered QDs. We have critically compared two direct methods of obtaining the strain distribution in uncapped QDs. As summary of this comparison, we suggest that the oxide layer thickness and finite AFM tip size should be taken into account when the widths of the iso-strain volumes determined from X-ray ISSM analysis are combined with AFM dot profiles to obtain strain distribution within QDs.

No substantial difference was found in the size and shape of the laterally ordered and unordered dots. From X-ray data, the dot width along the $[1\bar{1}0]$ direction was found to be 70 nm. From comparison of dot profiles obtained from X-ray data and from AFM images we conclude that uncapped QDs are covered with an oxide layer of approximate thickness 5 nm. The root mean square displacement of QDs of the topmost QD layer from their ideal lattice sites is found to be $\sigma = (7.0 \pm 0.5)$ nm. This value is in a good agreement with the mean displacement $\sigma = (9 \pm 3)$ nm determined from an AFM image of the ordered QDs. Finally, we found that both the laterally ordered and unordered QDs are vertically stacked in columns.

Outlook

An interesting direction of further research of this type of dot multilayers would be the determination of the chemical composition of the dots and of the ridges underneath the dots. This should be possible by comparing intensities of X-ray scattering for strong and weak in-plane reflections of the zinc blende structure, e.g., (400) and (200) reflections, as described in Sec. 2.3. Additionally structural characterization of the buried dots should be possible by means of high-angle X-ray diffraction and the data analysis presented in the next chapter. Nevertheless, the analysis would be complicated by the presence of the ridges underneath the dots.

Acknowledgements

The sample was grown and the AFM analysis was performed by Dr. S. Kiravittaya (MBE group, Max Planck Institute Stuttgart, Germany). His openness for any discussion on the sample structure is acknowledged. The cooperation with Dr. B. Krause on the synchrotron measurements at ID01 beamline at ESRF Grenoble (France) was of much help.

Chapter 5

Ge/Si islands in a three-dimensional island crystal

5.1 Introduction

Ordering of nano-islands in three-dimensional (3D) crystals yields improvements in the island size homogeneity [ZB04] and in device performances [SE01]. Similar to InAs/GaAs QDs, lateral positions of Ge/Si nano-islands can be controlled by growing islands on a patterned substrate. Stacking of QDs separated by spacer layers of appropriate thickness results in 3D island crystals (see Sec. 4.2.1 and references therein). In this chapter we report on a structural study on a 3D island crystal of Ge islands.

In contrast to the study presented in Sec. 4.2, we used coplanar high-angle XRD to investigate the size and the chemical composition of islands in this case. The aim was to investigate buried islands. The evaluation of the experimental data was based on calculations of the diffusely scattered intensity for a model island. The parameters of the island model were varied until a satisfactory agreement between the experimental data and the simulation was obtained. In order to calculate the diffuse intensity distribution, the strain fields due to the lattice mismatch between Si and Ge are required, and have to be calculated in each iteration of the fitting process. For this purpose we used an analytical solution of the continuum elasticity equations. A similar approach was used for the calculation of strain fields in two-dimensional problems, for systems homogeneous along one direction, e.g., SiGe wires [RHH$^+$02] and laterally modulated $(InAs)_n/(AlAs)_m$ short period superlattices [LHM$^+$02, CKH$^+$04]. Here we present an an extension of this method to the calculation of strain fields in three dimensions and apply it to the calculation of the strain in a 3D island crystal.

The results of the X-ray analysis are used to interpret low-temperature photoluminescence (PL) measurements on the same sample: for 3D bandstructure calculations of the island crystal, the structural parameters are required as an input.

The chapter is organized as follows: sample growth and X-ray experiments are described in section 5.2; in Sec. 5.3 calculations of the diffusely scattered intensity and of

the strain fields for a 3D island crystal are presented; Sec. 5.4 contains an analysis of the experimental data, a discussion of the resulting island structural parameters and of the strain fields within the studied island crystal.

5.2 Experiment

5.2.1 Sample growth

The investigated sample was grown by solid-source molecular beam epitaxy on a Si (001) substrate, which was prepatterned with a square grid of holes using electron beam lithography and reactive ion etching. The hole grid is oriented along ⟨110⟩ directions and its lattice constant is 400 nm (see the scheme in Fig. 5.1). The size of the patterned area is 0.5×0.5 mm^2. After oxide removal, first a 150 nm thick Si buffer layer was deposited. Further depositing 8 ML of Ge at 700 °C results in 2D ordered islands, with one island per hole. After depositing 30 nm of Si as a spacer layer 12 double-layers of Ge islands and Si spacer layers of about 25 nm were deposited at 650 °C. The topmost island layer was left uncapped for atomic force microscopy (AFM) investigations. The islands grew in the same 2D square grid in each island layer due to their preferential nucleation in strain energy minima above the underlying islands and the holes, throughout the entire island multilayer. A nearly perfect 3D island crystal was produced in this way. Further details on the sample growth are given in Ref. [ZCS$^+$04], where also an AFM image of the topmost island layer is shown. The aspect ratio of the uncapped island side facets η = height/width = 0.2, obtained from AFM, corresponds to {105} orientation. This type of side facets is characteristic for pyramidal islands.

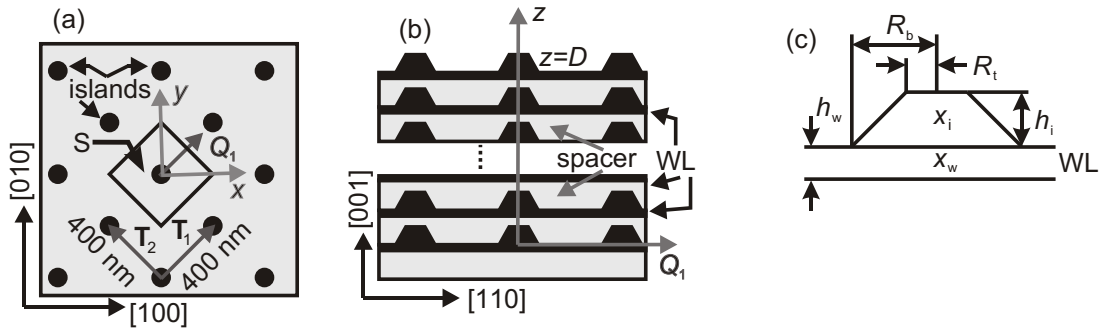

Figure 5.1. Schematic diagram of the investigated 3D island crystal and the coordinate system used in this chapter. (a) Top view of a island layer. $\mathbf{T}_1$ and $\mathbf{T}_2$ are basic translation vectors of the lateral 2D island lattice and S is the corresponding unit cell. (b) The side view on the $(1\bar{1}0)$ plane. Island layers are separated by Si spacer layers. WL denotes the wetting layer underneath the islands. (c) Scheme of the island model used for the simulations of the scattered intensity and the strain field calculations. All islands were assumed to have the same shape of a truncated cone and were characterized by bottom and top radii, R_b and R_t, respectively, a height h_i, and a Ge content x_i. The wetting layer (WL) was characterized by a thickness h_w and a Ge content x_w.

5.2.2 X-ray measurements

The X-ray measurements were carried out at the ID10B beamline at the European Synchrotron Radiation Facility (ESRF), Grenoble, with an X-ray wavelength of $\lambda = 1.547$ Å. High resolution XRD was measured in coplanar geometry. We used a Si (111) analyzer crystal in front of a point detector in order to resolve satellite maxima from the laterally ordered islands. A small primary beam size of 0.2×0.2 mm^2 was used in order to illuminate only the ordered islands above the patterned field.

Diffusely scattered intensity around the symmetrical (004) and asymmetrical (224) substrate lattice points was measured as a function of the wave vector transfer $\mathbf{Q} = \mathbf{K}_\mathrm{f} - \mathbf{K}_\mathrm{i} - \mathbf{h}$, with respect to the reciprocal lattice vector $\mathbf{h}$. The scattering plane normal was oriented along $[1\bar{1}0]$ for both measurements. The lateral component of the wave vector transfer $\mathbf{Q}$, oriented along the [110] direction, will be referred to as Q_1 (see Fig. 5.1) further on. The resulting reciprocal space maps (RSMs) are plotted in Fig. 5.2. The perfect lateral ordering of the islands due to the prepatterning results in lateral satellites up to 12$^{\mathrm{th}}$ and 15$^{\mathrm{th}}$ order for the (004) and (224) RSMs, respectively. Horizontal stripes of enhanced intensity, denoted SL-3 – SL1 in Fig. 5.2, are vertical satellites originating from the vertical ordering in the island superlattice. The distance of the satellites δQ_z is given by the superlattice period $L_\perp$ as $\delta Q_z = 2\pi/L_\perp$. From X-ray data we determined $L_\perp = (30.0 \pm 0.5)$ nm, slightly larger than the nominal superlattice period. Additionally, maxima in the envelope curves of the lateral satellites due to the elastic relaxation in the islands are observed in the (224) RSM. These maxima are denoted SM in Fig. 5.2(b); the intensive Si substrate peaks are denoted by Sub in both RSMs.

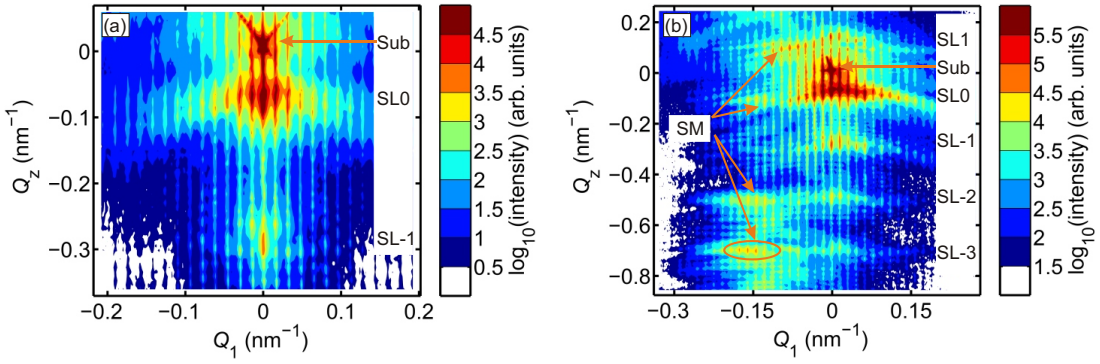

Figure 5.2. Measured reciprocal space maps around the (004) (a) and (224) (b) reciprocal lattice points. Vertical satellites, originating from the periodicity of the island layers along the growth direction, are denoted SL-3 – SL1. Substrate peaks are denoted by Sub and SM denotes maxima in the envelope curves of the lateral satellites.

We measured an $\omega-$scan around the (220) reciprocal lattice point of a pure Si crystal in order to determine the resolution of our experimental setup. The resolution along the Q_1 axis is $\Delta Q_1 = 2 \times 10^{-4}$ Å and $\Delta Q_1 = 5 \times 10^{-4}$ Å for the (004) and the (224) diffractions, respectively. In Sec. 5.4 we show that the width of the lateral satellites is comparable to this resolution.

5.2.3 Photoluminescence

The low temperature ($T = 4.2$ K) PL spectra shown in Fig. 5.3 were measured with an InGaAs line detector cooled to 173 K mounted to a grating monochromator. The PL was excited by the 512 nm line of an Ar^+-ion laser with a power of 40 mW focused to a spot with approximately 0.5 mm diameter. In the luminescence spectra, lines from the two-dimensional wetting layer (950-1050 meV) and from the SiGe islands (830-950 meV) can clearly be distinguished.

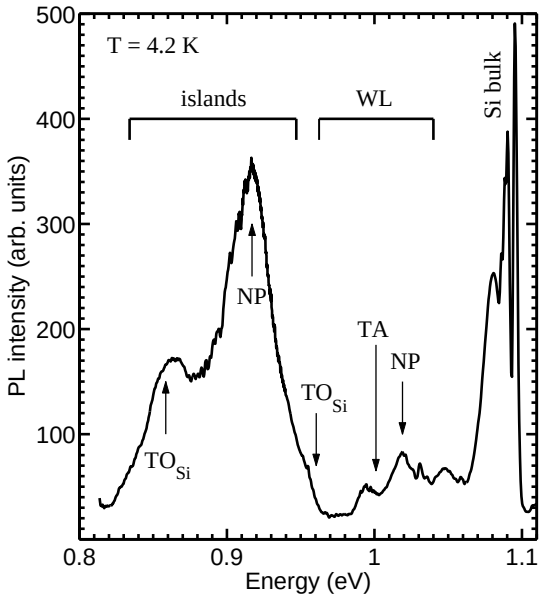

Figure 5.3. PL spectra of the investigated sample taken at 4.2 K. NP denotes the no-phonon luminescence. TO and TA are the transversal optical and transversal acoustic phonon replica, respectively. Lines in the energy regions (950-1050 meV) and (830-950 meV) originate from the two-dimensional wetting layer and the SiGe islands, respectively.

5.3 Theory

In Sec. 5.3.1 we derive expressions for the calculation of the intensity diffusely scattered from a 3D island crystal, which were used in our simulations. The equations for the scattered intensity involve also the displacement field in the sample. Its calculation is discussed in Sec. 5.3.2.

For all calculations we assume that the islands in each island layer form a perfect 2D lattice and that the islands are perfectly stacked above each other along the [001] growth direction in consecutive island layers. Additionally, the size, shape, and chemical composition of all islands in the 3D island crystal are assumed to be identical. The choice of the coordinate system used throughout the calculations is shown in Fig. 5.1. For simplicity we neglect in the calculations the uncapped island layer on top of the sample, but rather assume a perfectly flat sample surface. In the coplanar diffraction geometry, the existence of the uncapped island layer does not influence substantially the scattered intensity, as is shown explicitly in Sec. 5.3.2.

5.3.1 Calculation of the scattered intensity

In the kinematical approximation the diffuse intensity scattered by a 3D island crystal is given as (see Eq. (2.24))

$$I(\mathbf{Q}) \propto \left| \int_V \mathrm{d}^3\mathbf{r}\, [\chi_{\mathbf{h}}^{(\mathrm{s})} + \Delta\chi_{\mathbf{h}}\rho(\mathbf{r})] \exp[-i(\mathbf{Q}\cdot\mathbf{r} + \mathbf{h}\cdot\mathbf{u}(\mathbf{r}))] \right|^2, \tag{5.1}$$

where $\Delta\chi_{\mathbf{h}} = \chi_{\mathbf{h}}^{(\mathrm{i})} - \chi_{\mathbf{h}}^{(\mathrm{s})}$ is the difference between the $\mathbf{h}$th Fourier coefficient of the island material polarizability $\chi_{\mathbf{h}}^{(\mathrm{i})}$ and the polarizability of the spacer lattice $\chi_{\mathbf{h}}^{(\mathrm{s})}$. The concentration of the island material in position $\mathbf{r}$ is denoted $\rho(\mathbf{r})$, where $\rho \in \langle 0, 1\rangle$, and $\mathbf{u}(\mathbf{r})$ is the local displacement field with respect to the nondeformed substrate lattice caused by the presence of both islands and wetting layers. The Fourier integral in Eq. (5.1) is performed over the whole volume V of the island crystal and the underlying substrate.

Since the island crystal is laterally periodic, the functions $\rho(\mathbf{r})$ and $\xi(\mathbf{r}) = \exp[-i\mathbf{h}\cdot\mathbf{u}(\mathbf{r})]$ are laterally periodic as well. Thus, we can express them as the Fourier series

$$\rho(\mathbf{R}, z) = \sum_{\mathbf{G}} \rho_{\mathbf{G}}^{\mathrm{F}}(z) e^{i\mathbf{G}\cdot\mathbf{R}} \text{ and} \tag{5.2a}$$

$$\xi(\mathbf{R}, z) = \sum_{\mathbf{H}} \xi_{\mathbf{H}}^{\mathrm{F}}(z) e^{i\mathbf{H}\cdot\mathbf{R}}, \tag{5.2b}$$

where the summation is done over the lateral vectors $\mathbf{H}$ and $\mathbf{G}$ of the lattice reciprocal to the lateral 2D lattice of the island columns with the basic translation vectors $\mathbf{T}_1$ and $\mathbf{T}_2$ (see Fig. 5.1). The coordinates $\mathbf{R}$ and z are the lateral and the vertical components of the position vector $\mathbf{r}$, respectively. $\rho_{\mathbf{G}}^{\mathrm{F}}(z) = (1/S)\int_S \mathrm{d}^2\mathbf{R}\,\rho(\mathbf{R}, z)\exp(-i\mathbf{G}\cdot\mathbf{R})$ and $\xi_{\mathbf{H}}^{\mathrm{F}}(z) = (1/S)\int_S \mathrm{d}^2\mathbf{R}\,\xi(\mathbf{R}, z)\exp(-i\mathbf{H}\cdot\mathbf{R})$ are the Fourier coefficients of the corresponding series at vertical position z. Here the integration is performed over the lateral unit cell of the island lattice S.

After the substitution of the Fourier series (5.2) into Eq. (5.1) and performing the 2D Fourier integral over the lateral coordinates we obtain

$$I(\mathbf{Q}) \propto \sum_{\mathbf{G}} \delta(\mathbf{Q}_\parallel - \mathbf{G}) \left|F_{\mathbf{G}}(Q_z)\right|^2, \text{ where} \tag{5.3a}$$

$$F_{\mathbf{G}}(Q_z) = \int_{-\infty}^{D} \mathrm{d}z\, [\chi_{\mathbf{h}}^{(\mathrm{s})}\xi_{\mathbf{G}}^{\mathrm{F}}(z) + \Delta\chi_{\mathbf{h}} \sum_{\mathbf{H}} \xi_{\mathbf{H}}^{\mathrm{F}}(z)\rho_{\mathbf{G}-\mathbf{H}}^{\mathrm{F}}(z)] e^{-iQ_z z} \tag{5.3b}$$

is the structure factor of the unit cell of the 3D island crystal. $\delta(\mathbf{Q}_\parallel - \mathbf{G})$ is the Dirac distribution, D denotes the depth of the base of the lowest island array measured from the sample surface, and $\mathbf{Q}_\parallel$ is the lateral component of $\mathbf{Q}$. Equation (5.3a) describes the intensity distribution concentrated in periodic satellite peaks forming the 2D reciprocal lattice $\mathbf{G}$.

5.3.2 Calculation of the displacement field

The method we use here for the calculation of the displacement field $\mathbf{u}(\mathbf{r})$ is based on the analytical solution of the elastic equilibrium equation, presented in Refs. [RHH$^+$02, LHM$^+$02, CKH$^+$04] for 2D elasticity problems. Here, we extend the formalism to the 3D case.

We start from the equilibrium equation

$$\frac{\partial \sigma_{jk}}{\partial x_k} + f_j = 0,\ j,k = x,y,z, \tag{5.4}$$

where

$$f_j = -\delta \frac{\partial}{\partial x_j}[(C_{11} + 2C_{12})\rho(\mathbf{r})] \equiv -\delta \frac{\partial g(\mathbf{r})}{\partial x_j} \tag{5.5}$$

is the jth component of the volume force density,

$$\sigma_{jk} = C_{jklm} \frac{\partial u_l}{\partial x_m} \tag{5.6}$$

is the stress tensor, δ is the lattice mismatch between the island and spacer materials, and C_{jklm} are the elastic constants. For further calculations we restrict ourselves to cubic materials. Then, C_{jklm} reduces to 3 independent components C_{11}, C_{12}, and C_{44} (in the well-known 6×6 notation). Eqs. (5.4) and (5.5) are exact only if we assume that the elastic constants C_{jk} do not depend on the position $\mathbf{r}$. In our sample, however, this dependence cannot be neglected, since the elastic constants of Si and Ge substantially differ. In this case, Eqs. (5.4) and (5.5) are only approximative. In order to avoid mathematical complexity of the problem, we have used elastic constants of the dot material in the expression (5.5) for the volume force density and the elastic constants of the surrounding material in Eq. (5.4). Since the chemical composition of the dot was assumed non-homogeneous, the elastic constants of the dot material depend on the position as well. Roch *et al.* proved in Ref. [RHH$^+$02] that the displacement field $\mathbf{u}(\mathbf{r})$ calculated using this approximation compares very well with finite elements method simulations.

The boundary conditions at the sample top and rear surface are

$$\sigma_{jz}|_{z=D, z\to-\infty} = 0. \tag{5.7}$$

Here, we assume both surfaces to be flat, restricting the calculation to buried islands only.

Since $\mathbf{u}(\mathbf{r})$ and $g(\mathbf{r}) \equiv (C_{11}(\mathbf{r}) + 2C_{12}(\mathbf{r}))\rho(\mathbf{r})$ have the translational symmetry of the lateral lattice of the island columns, we express them using a 2D Fourier series

$$\mathbf{u}(\mathbf{R},z) = \sum_{\mathbf{K}} \mathbf{u}^{\mathrm{F}}_{\mathbf{K}}(z) e^{i\mathbf{K}\cdot\mathbf{R}}, \tag{5.8a}$$

$$g(\mathbf{R},z) = \sum_{\mathbf{K}} g^{\mathrm{F}}_{\mathbf{K}}(z) e^{i\mathbf{K}\cdot\mathbf{R}}. \tag{5.8b}$$

After the substitution of Eqs. (5.6) and (5.8) into Eq. (5.4) we get a set of 3 linear ordinary differential equations for each Fourier coefficient $\mathbf{u}_{\mathbf{G}}^{\mathrm{F}}$

$$\hat{\mathbf{A}}(\mathbf{u}_{\mathbf{K}}^{\mathrm{F}})'' + i\hat{\mathbf{B}}(\mathbf{u}_{\mathbf{K}}^{\mathrm{F}})' - \hat{\mathbf{C}}\mathbf{u}_{\mathbf{K}}^{\mathrm{F}} = \mathbf{P}, \tag{5.9}$$

where prime ($'$) denotes the derivative with respect to z. Matrices $\hat{\mathbf{A}}$, $\hat{\mathbf{B}}$, and $\hat{\mathbf{C}}$ are expressed by Eq. (A.1). The detailed solution of Eq. (5.9) is given in Appendix A. Vector $\mathbf{P}$ is the 2D Fourier transform of the volume force $\mathbf{P} = \delta(\partial g(\mathbf{r})/\partial x_j)^{\mathrm{F}}$, given by Eq. (A.2).

As mentioned above, in the calculations of the strain fields and scattered intensities we neglected the top layer of the uncapped islands. In order to check the validity of this approximation we performed simulations of the (224) RSM according to the following two schemes: (a) The displacement field and the scattered intensity were calculated using Eqs. (5.8a) and (A.11) and Eq. (5.3) for 13 buried island layers, and (b) We used the same displacement field as in (a) for the buried layers but the displacement field in the topmost, 13^{th}, island layer was multiplied by a factor of 2 in order to simulate the higher relaxation in the uncapped islands. The diffusely scattered intensity was calculated using modified Eqs. (5.3), where we took into account the uncapped island layer, i.e., the shape of the sample surface. No significant differences were observed in the simulations of RSMs calculated according to both schemes (a) and (b). Thus, we conclude that for the purposes of our simulations we may consider the topmost island layer as being capped in a good approximation. This is due to the fact that the penetration depth of X-rays in our particular experiment is much larger than the thickness of the island crystal and the RSMs are sensitive mostly to the average shape of the islands and the average strain fields in the island crystal.

5.4 Results and discussion

As already mentioned in Sec. 5.3.1 and clearly visible in measured RSMs (Fig. 5.2), the diffusely scattered intensity from the 3D island crystal is concentrated in lateral and vertical satellites. In order to evaluate X-ray data we fitted the measured intensity profiles along the Q_1 axis by a series of Lorentzians (see Fig. 5.4). The amplitudes of the Lorentzians are plotted in Figs. 5.5(a) and 5.5(c) as a function of the satellite order along the [110] direction and Q_z for (004) and (224) diffractions, respectively. The type of the lateral ordering of the island positions can be determined from the dependence of the full width a half maximum (FWHMs) of the satellites on the satellite order for constant Q_z [HSS$^+$00]. If the island positions obey the short range order model, the FWHM of the satellites increase parabolically with their Q_1 positions while the constant satellite FWHM, i.e., independence of Q_1, is typical for a long-range order. In our measurements the FWHM of the satellites was constant, except for noise. The average satellite FWHM was approximately 3×10^{-4} Å^{-1} for both (224) and (004) RSMs, which is of the order of the resolution of the measurements along the Q_1 axis (see Sec. 5.2.2). In our case the long-range model is more appropriate for the description of the island positions because of the order imposed by

the prepatterning. We assumed the FWHMs of the satellites to be constant for the purpose of the data evaluation and compared the amplitudes of the Lorentzians to intensities $|F_{\mathbf{G}}(Q_z)|^2$ calculated by Eq. (5.3).

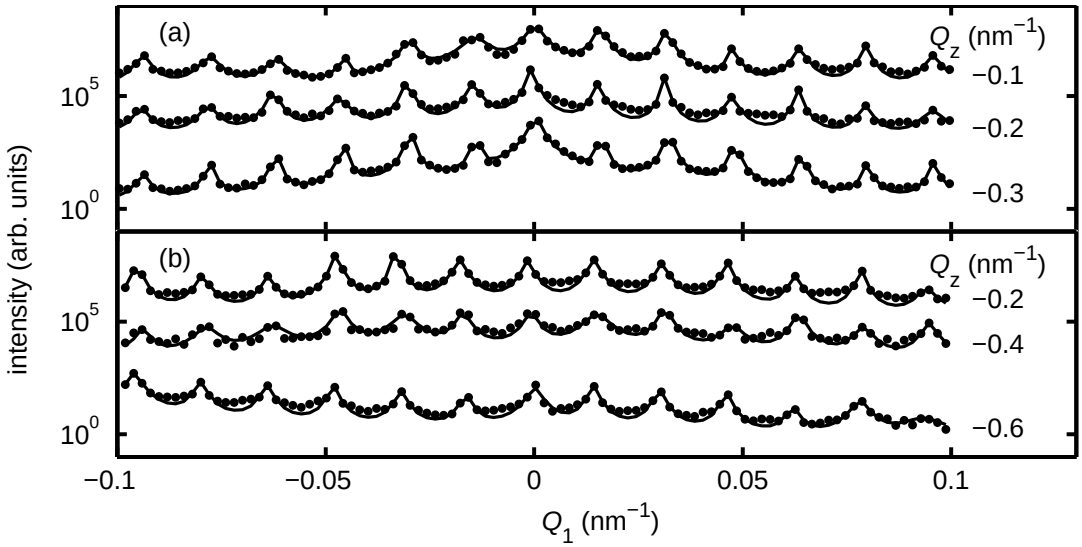

Figure 5.4. Sections along the Q_1 axis through measured (004) (a) and (224) (b) RSMs at various values of Q_z as indicated. The measured data (•) were fitted by series of Lorentzians (lines).

Additionally, the Q_1 position of the lateral satellites of the given order is constant for all measured sections along the Q_1 axis, i.e., it is independent of its Q_z position. This fact implies vertical replication of the lateral island positions in subsequent island layers. For appropriate spacer layer thicknesses, like in our case, Ge islands typically nucleate in vertical columns when deposited in Ge/Si multilayer structures [Bru02]. However, recently some exceptional ordering was reported. Sutter *et al.* and Kermarrec *et al.* in Refs. [SMSV01] and [KCB04], respectively, reported on oblique stacking of Ge islands grown by low pressure chemical vapour deposition, when the spacer thickness is larger than 30 nm. Furthermore, ABAB-type stacking was observed for spacer thicknesses larger than 90 nm. This type of island self-ordering is caused by regular corrugations on the surface of the Si capping layer, which influence the nucleation of the Ge islands in the growing layer [KCB04].

For the simulations of the diffuse intensity and the strain field calculations all islands were assumed to have the same shape of a truncated cone, characterized by its bottom radius R_b, top radius R_t, and height h_i [see Fig. 5.1(c)]. Though Ge pyramids with a square-base are observed in AFM, preferential alloying of the island corners was reported in Ref. [DSS03], so that a rounded shape of buried islands is expected. The rotational symmetric island model used here mimics this effective rounding of the islands. Furthermore, it turned out that the simulations are most sensitive to the slope of the island sides, and hence the aspect ratio, whereas other details of the shape play a minor role. The Ge content x_i was first assumed to be constant within the island. Additionally, a wetting layer (WL) of a constant thickness h_w and a constant Ge content x_w throughout the lateral unit

cell S was involved in the model structure. In a later stage of fitting, a Ge gradient along growth direction was included to refine the result. The parameters of the model were varied to obtain the best correspondence between the measured satellite intensity in the RSMs (Figs. 5.5(a) and 5.5(c)) and simulations obtained by Eqs. (5.3), (5.8a), and (A.11).

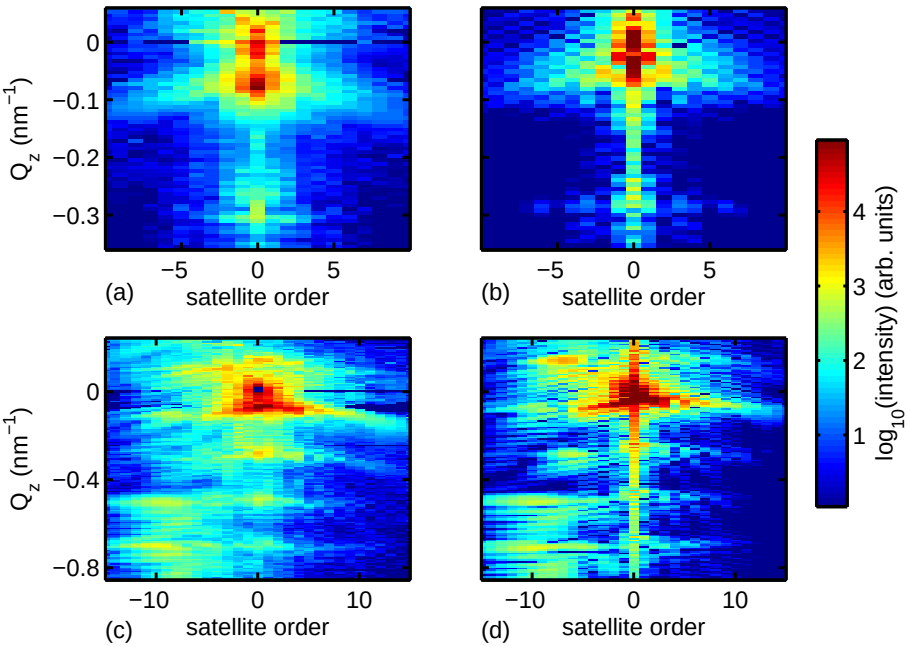

Figure 5.5. 2D maps of the lateral satellite intensities extracted from RSMs measured around the (004) (a) and (224) (c) reciprocal lattice points. The panels (b) and (d) show the satellite intensities $\left|F^{\mathrm{F}}_{\mathbf{G}}(Q_z)\right|^2$ simulated in (004) and (224) diffractions, respectively.

In the course of the fitting process we made the following observations. (i) The lower the Ge content in the islands, the more intensive the lateral satellites are close to the substrate peak. Furthermore, the maxima in the envelope curves of the lateral satellites [denoted SM in Fig. 5.2(b)] move closer to the 0^{th} order lateral satellite, i.e., to $Q_1 = 0$ nm^{-1}. Indeed, this can be explained by the decrease of the island lattice strain due to the lower Ge content. (ii) The positions of the lateral satellite envelope maxima approach the reciprocal space position of fully relaxed Ge at $Q_1 = -1.3$ nm^{-1}, as the lateral strain ϵ_{xx} within the island stack increases with increasing island height. (iii) The vertical shift of the 0^{th} order vertical satellite with respect to the substrate Bragg peak increases with increasing total amount of Ge in the WL, which is expressed in terms of the fitting parameters by the product $x_{\mathrm{w}}h_{\mathrm{w}}$. (iv) Finally, for narrow islands the vertical satellites SL-3 to SL1 are parallel to the Q_1 axis. However, for wider islands the vertical satellites become tilted with respect to Q_1 and the tilt increases more with widening of the island base.

The best simulations [see Figs. 5.5(b) and 5.5(d)] of (004) and (224) experimental RSMs were obtained for island bottom and top radii of $R_{\mathrm{b}} = (85\pm10)$ nm and $R_{\mathrm{t}} = (10\pm10)$ nm, respectively, island height of $h_{\mathrm{i}} = (19\pm4)$ nm, and a Ge content of $x_{\mathrm{i}} = (40\pm5)$ %. The WL

thickness was $h_{\mathrm{w}} = 0.8$ nm and the Ge content in WL was $x_{\mathrm{w}} = 10$ %. We present these two values without errors, since only the product $x_{\mathrm{w}} h_{\mathrm{w}}$ can be determined from the fitting process. There are significant differences between the simulation and the experimental data close to the substrate peak and the truncation rod (zero order satellite along Q_x). This is because the kinematical approximation [Eq. (5.1)] fails in these regions. Nevertheless, the correspondence of the simulation and the experimental data in the regions more distant from the substrate peak, where the kinematical approximation is applicable, is good. From the obtained island parameters an aspect ratio of $\eta = h_{\mathrm{i}}/(R_{\mathrm{b}} - R_{\mathrm{t}}) = (0.25 \pm .05)$ follows. This value is close to $\eta = 0.2$ corresponding to the $\{105\}$ facets, which are typical for Ge pyramids, and different from $\eta = 0.47$ corresponding to $\{113\}$ facets, which are typical for Ge domes. Thus, we conclude that the shape of the capped islands does not differ considerably from that of the uncapped ones.

Additionally, in order to estimate errors of the determined island parameters, we also simulated a series of (224) RSMs changing individual fitting parameters in the vicinity of their optimum. As an example we show a comparison of the sections through experimental and simulated RSMs along Q_1 axis in Fig. 5.6, where the experimental data are plotted by lines and simulations by symbols. The sections were taken approximately through the vertical satellites SL-3 ($Q_z = -0.07$ Å^{-1}), SL-2 ($Q_z = -0.0505$ Å^{-1}), and SL-1 ($Q_z = -0.0285$ Å^{-1}) (from top to bottom in each panel). Figure 5.6(a) shows simulations for the optimal set of island parameters, i.e., cuts through the RSM shown in Fig. 5.5(d). The correspondence between the simulation and the experimental data for SL-1 (lower curve) is worse than those for SL-2 and SL-3 (upper two curves). This is because the fitting process was done by simulating the whole RSMs and the stress was laid on correspondence between the simulation and the experimental data in the regions more distant from the substrate peak, where the intensity distribution is mainly determined by the strain state in the islands. Figure 5.6(b) exhibits the sensitivity of the Q_1 profiles on the aspect ratio of the islands. All island parameters were the same as for Fig. 5.6(a) except for the island base radius, which was set to $R_{\mathrm{b}} = 103$ nm, yielding an aspect ratio of $\eta = 0.2$, equal to the value obtained from AFM for uncapped islands. This shows that a slight shape change does indeed take place during capping. For the simulation in Fig. 5.6(c) we used the same set of the island parameters as for the simulation in Fig. 5.6(a) except for the Ge content, which was higher by 10 %.

In order to further improve the fit, we introduced a gradient along growth direction of the Ge content. In accordance with previous results we assumed a square-root dependence [SDH$^+$01, HSH$^+$02] from x_{b} at the bottom of the island to x_{t} at the top. The best simulation was always obtained for Ge content increasing from the island base to the top and an average Ge content of $\langle x_{\mathrm{i}} \rangle = 40$ %. The Ge content gradient with increase towards the island top is typical for MBE grown Si/Ge islands [SDH$^+$01, HSH$^+$02] as well as for liquid-phase epitaxy grown islands [WSH$^+$00, HSG$^+$04]. In fact, the sensitivity of the fits to the Ge profile was not very pronounced, however, a maximum possible difference between the Ge content at the island base and at the top of $x_{\mathrm{t}} - x_{\mathrm{b}} = 10$ % can be derived.

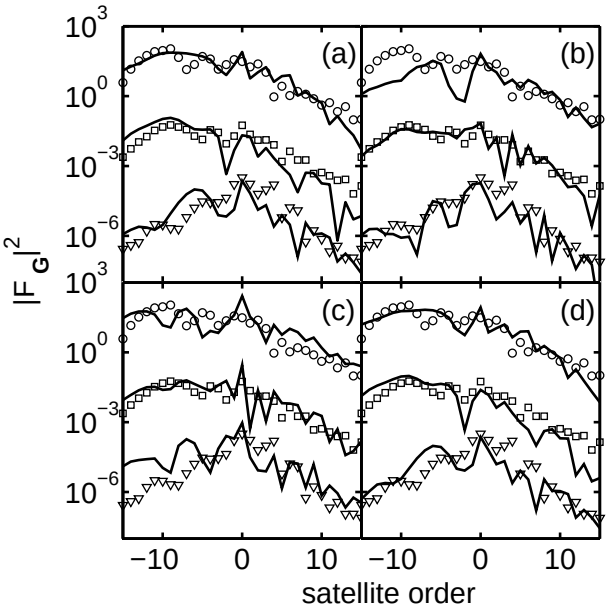

Figure 5.6. Comparison of the intensities of the lateral satellites in sections through the measured (224) RSM taken approximately through the vertical satellites SL-3 ($Q_z = -0.7$ nm^{-1}), SL-2 ($Q_z = -0.505$ nm^{-1}), and SL-1 ($Q_z = -0.285$ nm^{-1}) (symbols from top to bottom in each panel) and simulations (full lines in each panel) of the corresponding sections. The respective panels show (a) the best simulation obtained; (b) the simulation for all island parameters as in (a) except for the bottom radius of the island, which was set to $R_\mathrm{b} = 105$ nm, yielding island aspect ratio of $\eta = 0.2$; (c) the simulation for all island parameters as in (a) except for the Ge content, which was by 10 % higher than in (a); (d) the simulation for the same island shape as in (a) and Ge content increasing from 35 % at the bottom of the island to 45 % at its top. The intensities of the 3 sections are mutually shifted by the same multiplication factor for both the experimental and simulated data in each panel.

The sections through the (224) RSM simulated for $x_\mathrm{b} = 35$ %, $x_\mathrm{t} = 45$ %, while keeping the island shape parameters at $R_\mathrm{b} = 85$ nm, $R_\mathrm{t} = 10$ nm, and $h_\mathrm{i} = 19$ nm, is shown in Fig. 5.6(d). The reduced sensitivity on the Ge profile as compared to studies on randomly distributed islands is due to the fact that the positions of the lateral envelope maxima is difficult to determine: it is influenced by background subtraction and the precision of the peak area determination. Most importantly, however, this study on a multilayer determines the average over several island layers. The island layers close to the substrate and the surface exhibit different strain fields (see description below), which will actually lead to differences in the island properties for these layers. It is not feasible, however, to include these differences into our model, as this would lead to a very large number of free structural parameters.

Calculated lateral ϵ_{xx} and vertical ϵ_{zz} strains within the island stack in plane (010) cutting through the centres of the islands are shown in Fig. 5.7. Here zero strain corresponds to the non-deformed Si lattice. The presented strain distributions have been calculated for the best-fitting set of island parameters. Only in the region $z = 90$ – 210 nm, i.e., in the 4$^\mathrm{th}$ to 7$^\mathrm{th}$ island layers from the bottom of the stack, the strain field is almost periodic in

vertical direction. This vertical periodicity is violated by the underlying Si substrate and the surface relaxation outside this region. Additionally, the real strain fields in the latter region are also influenced by the surface island layer, which was not taken into account in our calculation. The following discussion concerns only the strain state in the region $z = 90 - 210$ nm. The lateral strain ϵ_{xx} decreases in the lateral direction from the centres of the islands towards their sidewalls. The maximum lateral strain of $\epsilon_{xx} = 0.90$ % is observed in compressed GeSi in the top edges of the islands. This value corresponds to the degree of relaxation of 55 % for $Ge_{0.4}Si_{0.6}$. The lateral strain minimum of $\epsilon_{xx} = -0.55$ % is observed in compressed Si around the bottom edges of the islands. The vertical strain ϵ_{zz} increases in the lateral direction from the center of the islands towards their sidewalls. The maximum vertical strain of $\epsilon_{zz} = 2.7$ % is observed in expanded SiGe in the bottom edge of the islands and the minimum vertical strain of $\epsilon_{zz} = -1.8$ % is observed in compressed Si just above the island tops. The calculation of the elastic displacement field in the island volumes and around them was performed using the elastic constants of the island material in Eq. (5.5) and the elastic constant of the Si matrix in Eq. (5.4). For the island sizes in our sample, this approach yields results very similar to numerical finite element calculations [RHH+02]. A more elaborate iterative scheme for the calculation of the strain field around a quantum dot as suggested in Ref. [ADFO99], needs not be applied here.

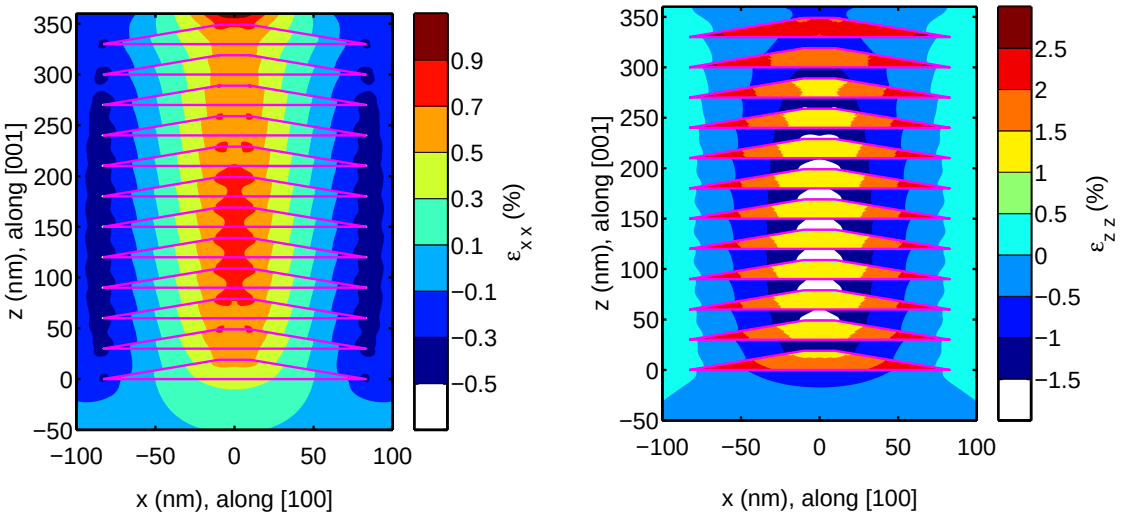

Figure 5.7. ϵ_{xx} and ϵ_{zz} components of the total strain tensor, i.e., strain with respect to the nondeformed Si lattice, calculated for the island parameters $R_b = 83$ nm, $R_t = 10$ nm, $h_i = 19$ nm, and $x_i = 40$ %. Contour steps in the respective plots are $\Delta\epsilon_{xx} = 0.2$ % and $\Delta\epsilon_{zz} = 0.5$ %.

The detailed information about dimensions and composition of the islands obtained by the evaluation of the X-ray data presented above is a prerequisite for a comparison of measured PL lines and a calculated bandstructure of the SiGe islands. The bandstructure calculations were performed by Dr. T. Fromherz (JKU Linz) with the NEXTNANO^3 code developed in the group of P. Vogl at the Technical University of Munich [nex]. A detailed discussion of these calculations is beyond the scope of this thesis and will be

given elsewhere [Fro]. As a summary, for the islands of this work, PL transition energies of 750 meV and 865 meV are calculated. For the low energy emission, heavy holes (HH) located in the SiGe island recombine with electrons in states that are built up from the Si conduction band minima in the growth direction (Δ_z). These states are bound to the Si region in the vicinity of the top circle of the SiGe cone. The larger transition energy corresponds to a recombination of electrons in bound states built up from the conduction band minima perpendicular to the growth direction (Δ_x, Δ_z). These states are located in the Si matrix in [100] and [010] directions around the circumference of the cone's basis. Wavefunction calculations, performed by Dr. T. Fromherz using NEXTNANO^3, revealed that for the islands investigated here the high energy transition is expected to be the predominant one due to a delicate interplay between the spatial distribution of the groundstate hole wavefunction, which critically depends on the island composition, and a presumably highly efficient trapping of the excited electrons into the states bound to the cone's basis (see Fig. 5.8). For this transition, the calculated PL transition energy (865 meV) is in reasonable agreement with the position of the no-phonon (NP) line in the PL spectrum shown in Fig. 5.3. In order for this mechanism to be effective, the Ge content variation along growth direction must not exceed about 10 %, which agrees well with the data obtained from X-ray diffraction.

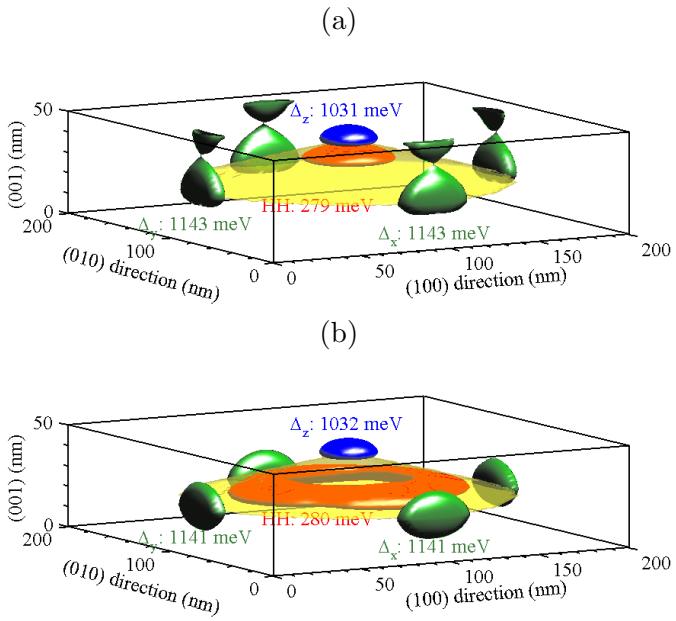

Figure 5.8. Isoprobability surfaces of the electron groundstate wavefunctions Δ_{xy}, Δ_z and of the heavy hole (HH) wavefunction. Energies corresponding to the respective wavefunctions are indicated. The surface of the SiGe cone is shown in yellow. Two different Ge content gradients 35–45 % and 37–43 % were assumed in wavefunction calculations shown in Figs. (a) and (b), respectively.

5.5 Summary

An analysis of coplanar high-angle X-ray diffraction data was performed and structural information on buried Ge islands forming a 3D island crystal was obtained. We have demonstrated that the combination of an analytical solution of the equilibrium equations of linear elasticity with kinematical scattering theory can be used to simulate the exper-

imental X-ray diffraction data. Comparing the measured reciprocal space maps of the diffracted intensity with simulations, we found that the capped islands have a side facet slope close to that of {105} facets, i.e., shape changes during capping are not dramatic. Additionally, the Ge content in the capped islands is about (40 ± 10) %, slightly increasing from bottom to top. The lateral island size is about (170 ± 20) nm, and their height turned out to be (19 ± 4) nm. The strain state in the buried islands and their surrounding Si matrix was determined. The surprisingly high energy of no-phonon PL from the islands is explained by transitions involving states in conduction band minima perpendicular to the growth direction. These states are located in the Si matrix around the island basis.

Acknowledgements

The sample was grown by Dr. Zhenyang Zhong (JKU Linz). The X-ray diffraction measurements and pre-processing of the experimental data were performed by Dr. J. Stangl (JKU Linz). The AFM analysis of the surface island layer was performed by Dr. Gang Chen (JKU Linz). Programs, which were utilized for simulations of X-ray diffraction data and strain fields, arose as a modification of original fortran source codes written by Prof. V. Holý. The PL measurements and band gap calculations were performed by Dr. T. Fromherz (JKU Linz).

Chapter 6

In(Ga)As/GaAs islands grown by low-pressure metal-organic vapour-phase-epitaxy

6.1 Introduction

Whereas the growth of InAs/GaAs QDs using molecular beam epitaxy has been the subject of numerous investigations, less work was devoted so far to low-pressure metal-organic vapour-phase-epitaxy (LP-MOVPE). It is the purpose of this chapter to report on structural properties of In(Ga)As islands grown by this method on (001) GaAs substrates, and on their modification during the growth. These properties are studied by X-ray diffraction and atomic force microscopy (AFM). The results are compared to a previous work [SGPMS02, SG02], carried out on the same structures by transmission electron microscopy (TEM). In particular X-ray data update information on relaxation state and In content of islands. Furthermore, the effect of annealing on InGaAs islands capped with GaAs was studied using both AFM and X-ray diffraction techniques.

6.2 Experimental

Sample growth

A series of LP-MOVPE grown InAs and GaInAs islands was investigated by AFM and high angle coplanar X-ray diffraction as well as grazing-incidence diffraction (GID). The growth sequences for investigated samples are given in Tab. 6.1. They were all grown at a pressure of 60 Torr, using trimethylaluminium, trimethylgallium and trimethylindium as precursors for Al, Ga, and In, and pure AsH_3 as precursor for As. For sample A[1] 2 monolayers (ML) of InAs were deposited on GaAs, for sample B 2 ML InAs followed by 5.2 ML $In_{0.15}Ga_{0.85}As$, sample C was like sample B but capped with 0.56 nm of GaAs,

[1]The samples were denoted as Or4860 (sample A), Or4866 (sample B), Or4867 (sample C), D (sample D), and Or4886 (sample E) in Ref. [SG02].

Sample	InAs (ML)	InAs grown at (°C)	$In_{0.15}Ga_{0.85}As$ (ML)	Capping layer GaAs (nm)	Annealed
A	2.0	460	0	0	No
B	2.0	460	5.2	0	No
C	2.0	460	5.2	0.56	No
D	2.1	460	5.2	1.5	620 °C
E	2.1	500	5.2	2.2	620 °C

Table 6.1. Structure and growth conditions of the samples.

sample D was capped with 1.5 nm GaAs and annealed at 620 °C during 9 minutes and finally sample E was capped with 2.2 nm GaAs and annealed at 620 °C during 9 minutes.

Results of TEM analysis

Here we summarize observations for all samples (see Tab. 6.2) obtained using TEM and reported in previous publications [SGPMS02, SG02] in order to correlate them with the presented results obtained by AFM and X-ray techniques. Small coherent islands, small plastically relaxed islands and large plastically relaxed islands were observed for sample A. The deposition of the InGaAs layer leads to the formation of a second high-density (250 μm^{-2}) population of coherent islands in sample B. Furthermore, the small coherent islands fabricated during the deposition of the InAs layer and observed in sample A overstep the critical size after InGaAs regrowth. They become dislocated and their size is the same as that of the small plastically relaxed islands observed in sample A. The density of large dislocated islands is unchanged for sample B compared to that of sample A. The gallium composition of the islands increases during the GaAs regrowth for sample C. Consequently, the dislocations at the InGaAs/GaAs interface underneath the small dislocated islands disappear and the islands form a population of large coherent islands. Small plastically relaxed islands do not occur for sample C any more. The density of large plastically relaxed islands is the same for samples B and C. The large plastically relaxed islands are partially dissolved during the annealing step in sample D. This annealing step has no influence on the densities of the others populations of islands. The large plastically relaxed islands were totally dissolved for sample E. As this sample was grown at slightly higher temperature the density of small coherent islands is only 25 μm^{-2}.

From TEM images recorded in 220 dark field follows that the dislocations contained in the dots are sessile 90° dislocations. Their lines are parallel to a $\langle 110 \rangle$ in-plane direction and their Burgers vectors are parallel to the other (perpendicular) $\langle 110 \rangle$ direction. The dislocations are at the interface of the island or the wetting layer and the substrate. This observation is in agreement with calculations of the energy of dislocations introduced into two-dimensional islands in Refs. [ST00, ST01]. Here, the authors calculated energy maps of 90° dislocations introduced into islands of various size. The dislocation energy was calculated up to the first order in terms of Burgers vector. The dislocation energy minimum was observed at the island/substrate interface. We have performed similar calculations

Sample	Small coherent islands (μm^{-2})	Large coherent islands (μm^{-2})	Small plastically relaxed islands (μm^{-2})	Large plastically relaxed islands (μm^{-2})
A	1.4	—	4	10
B	250 (2^{nd} population)	—	6	10
C	250	6	—	10
D	130	—	—	10
E	25	—	—	—

Table 6.2. Densities of the different types of islands observed for investigated samples by TEM and reported in Refs. [SGPMS02, SG02].

to estimate the energy of a dislocation in three-dimensional islands. The calculation of the dislocation energy as well as a result of the calculation for an island similar to that observed for the samples under investigation are shown in Appendix B. As a summary of these calculations, we observed a dislocation energy minimum, i.e., the equilibrium position of the dislocation, at the wetting layer/substrate interface in the center of the island. The first-order dislocation energy was found to be 7.6 keV in the model system.

AFM images

Fig. 6.1 shows AFM images of selected samples. In the AFM images two types of islands can be distinguished. Large islands higher than 5 nm and with a density up to 15 μm^{-2} are observed for all samples. Furthermore, islands smaller than 5 nm [clearly visible in Fig. 6.1(a)] with a density up to 300 μm^{-2} are observed for samples B, C, D, and E. Additionally, for the annealed sample E [Fig. 6.1(c)] depleted areas and striation are seen on the surface. These features are the result of the dissolution of the large relaxed islands. The shape of their base appears clearly as rhomboidal. Pits and grooves around the dissolved large islands are observed for sample E (Fig. 6.1(c)). The occurrence of pits was explained in Ref. [SGPL$^+$02] as an indication that with increasing GaAs capping layer thickness the large plastically relaxed islands are dissolved and an In-rich GaInAs top layer is formed.

X-ray measurements

To gain information on the lattice deformation of the islands as well as on their In content X-ray diffraction data were recorded. Experiments were performed at the ID01 as well as at the ID10B beamline of the ESRF, Grenoble, France and at the BW2 beamline of HASYLAB Hamburg. For the coplanar geometry, the diffracted intensity was recorded around the asymmetric GaAs (224) Bragg reflection. Resulting reciprocal space maps (RSM's) are shown in Fig. 6.2 for samples A–C. The most intense peak in the RSMs is the GaAs substrate Bragg reflection. The stripe of enhance intensity along the Q_z axis at $Q_x = 31.4$ nm^{-1} is the crystal truncation rod due to the free surface of the sample. For samples A, B and C we observe enhanced diffuse scattering close to the InAs (224)

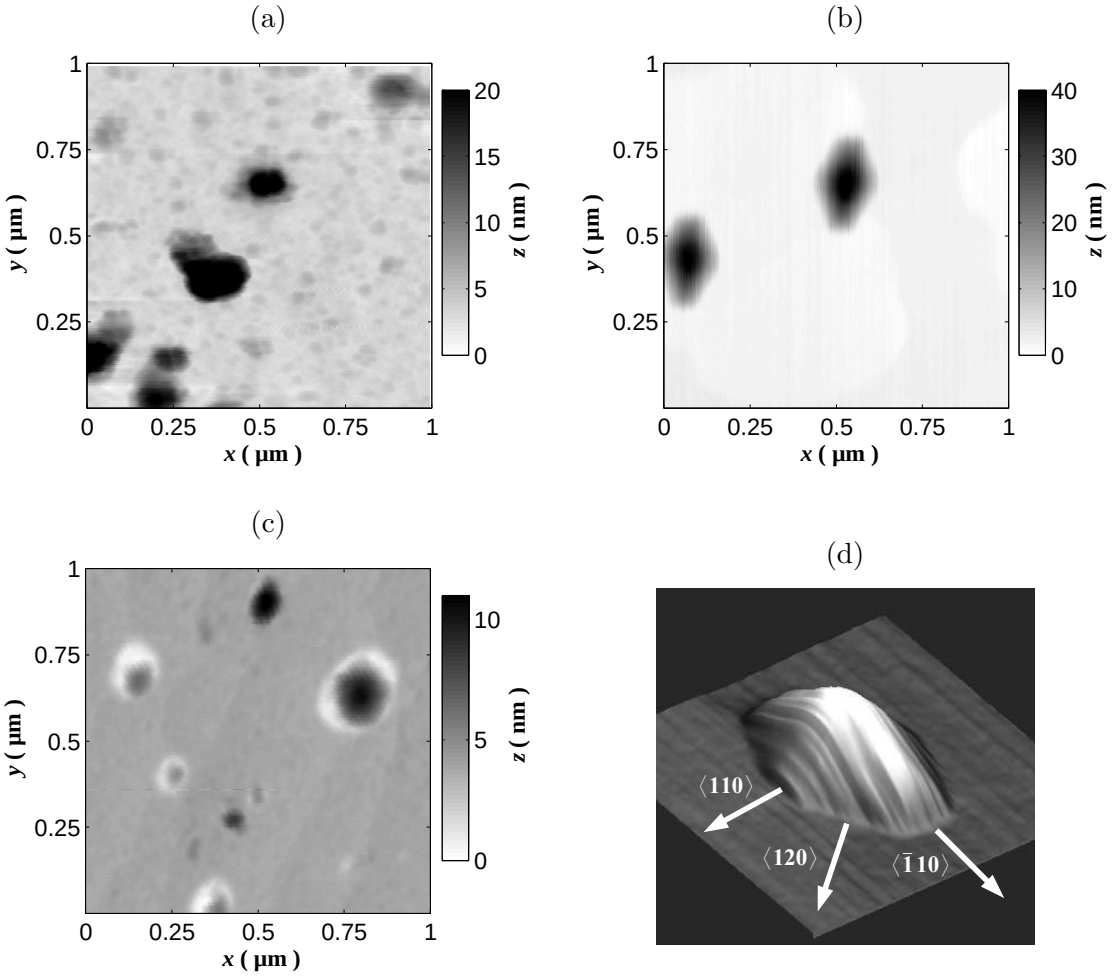

Figure 6.1. AFM images of samples B (a), D (b) and E (c). Enlargement of a faceted island of sample D (d).

Bragg reflection. The diffuse scattering clearly indicate the presence of a nearly completely relaxed InAs islands. For sample D the maximum of diffuse scattering is shifted towards the GaAs Bragg peak. The shift gives an evidence for an increase of the Ga content in islands due to the interdiffusion between the InAs islands and the GaAs substrate and cap layer. For sample E we did not observe any enhancement of the diffuse scattering.

Experiments in grazing incidence geometry (see Sec. 2.2) were performed. We measured radial scans around the (220) in-plane Bragg reflection for samples A, B, C, and E, in order to gain direct information on the in-plane lattice constant $a_{\parallel}$. The measurements in this geometry were done as a function of the sample rotation angle ω, and the in-plane scattering angle 2θ (Fig. 2.5). The incidence angle α_i was fixed and the scattered intensity was recorded as a function of the exit angle α_{f} using a position sensitive detector with an angular range of 0° to 1.2°. The wavelength of the X-rays used was $\lambda = 0.155$ nm. The scattered intensities were recorded as a function of $Q_{\mathrm{r}} = (4\pi/\lambda)\sin(\theta/2)$. A radial scan covers the range of the Bragg peaks from InAs to GaAs and it is sensitive to the strain status of the sample, i.e., regions with different in-plane lattice parameter $a_{\parallel}$ within the

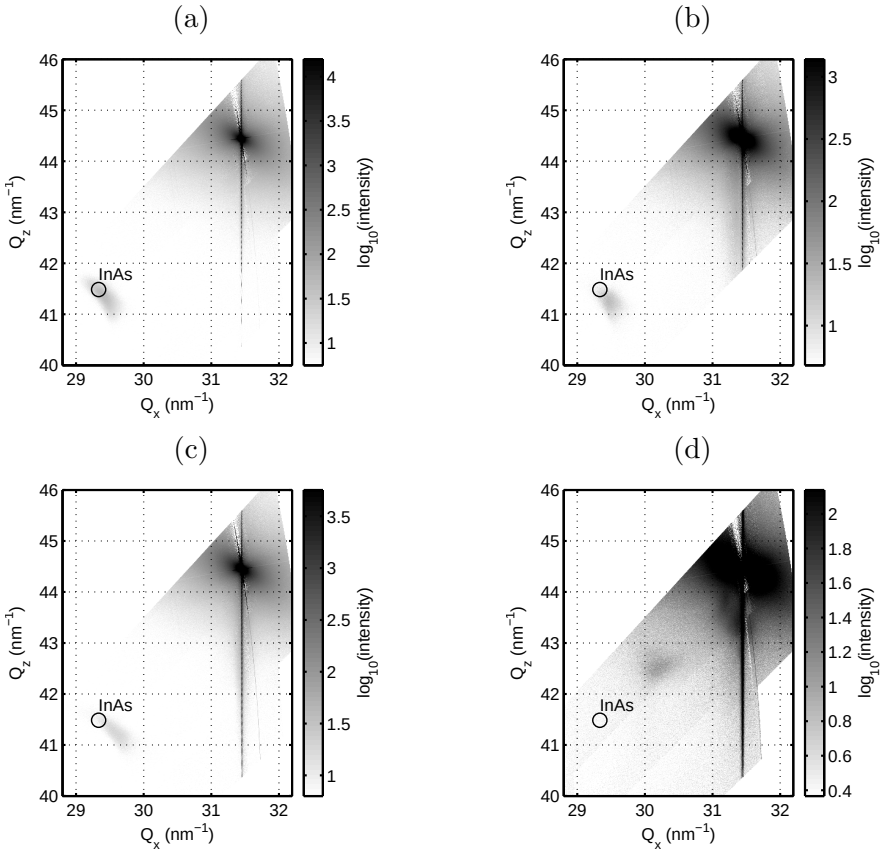

Figure 6.2. High resolution X-ray diffraction data around (224) Bragg reflection in coplanar geometry for samples A-D (from left to right and from top to bottom). The open circle in each graph corresponds to the (224) Bragg reflection of fully relaxed InAs.

sample scatter to different $Q_r = 2\pi/a_{||}\sqrt{h^2+k^2+l^2}$ values. In addition angular scans were recorded for sample A. Angular scans are performed for fixed values of the scattering angle 2θ, while only the sample rotation angle ω is changed. An average island from the whole population of the islands can be thought of as being composed of a distribution of iso-strain volumes (see Sec. 2.3). From the full width at half maximum (FWHM) of the angular scans, one can extract the average diameter D_{iso} of the iso-strain area of particular in-plane lattice constant $a_{||}$. In fact the FWHM values of the diffraction profiles in angular direction are inversely proportional to the lateral size of the iso-strain area.

6.3 Results and analysis

AFM images

As indicated in the previous section the islands observed by AFM can be divided into groups of the large and small islands. The large islands, higher than 5 nm, have a density up to 15 μm^{-2}, which is the same as the total density of large plastically relaxed, small plastically relaxed (for samples A and B), small coherent (for sample A) and large coherent (for sample C) islands observed by TEM in Refs. [SGPMS02, SG02]. Thus we conclude

that these large islands represent the first population of islands grown after the deposition of the InAs layer and observed already for sample A. The lateral sizes and heights of the large islands obtained from AFM are summarized in Tab. 6.3. AFM cannot discriminate between plastically and elastically relaxed islands, but the determination of the size of the islands is more precise than that from TEM, since bright field images, which were presented in Refs. [SGPMS02, SG02], are mainly sensitive to the strain field of the islands. A histogram of the heights of large islands is shown in Fig. 6.3 for sample C. Their most probable height is about 25 nm.

	A	B	C	D	E
Density (μm^{-2})	6–15	2–11	8–15	8–15	5–8
Height (nm)	5–80	5–50	5–60	5–60	1–15
Lateral size (nm)	40–200	50–200	50–200	100–250	40–200

Table 6.3. Structural properties of the large islands obtained from AFM

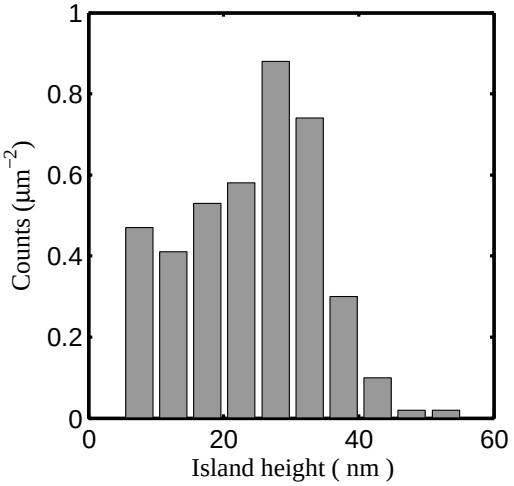

Figure 6.3. Height histogram of the large islands of sample C.

In addition, small islands with a density of the order of 1×10^2 μm^{-2} are observed for samples B–E. They form a second population of islands nucleated on the rough InAs surface after deposition of the InGaAs layer. The root mean square roughness of the InAs surface of the sample A was approximately 1 nm. TEM images show that these islands are elastically relaxed [SGPMS02, SG02]. The height of the small islands is 1–5 nm with most probable height approximately 4 nm for samples B–D and 0.2–1 nm for sample E. Thus the small coherent and the large islands really form two independent populations from the morphological point of view. The lateral size of the small islands is 20–50 nm for all samples B–E.

For both annealed samples D and E we observe additional features in the AFM data. For sample D striation of the layer surface of the depth 1–2 nm [not visible in the Fig. 6.1(b)] and depleted areas with a depth 1.5 nm and a lateral size up to 5 μm are observed. Similarly, pits [see Fig. 6.4(a)] and grooves around the big islands [see Figs. 6.1(c) and 6.4(b)], both of depth 1–4 nm, are observed for sample E. Moreover the

large islands are facetted for the sample D [see Fig. 6.1(d)]. From the slope of the sidewalls the indices of facets can be $\{12h\}$ ($h > 4$) and $\{11h\}$ ($h > 3$). The heights of the islands do not change after annealing in this case. On the other hand, the heights of the large islands are decreased to about 15 nm for sample E and they seem to be rotationally symmetric. These phenomena of channels, grooves, pits, formation of depleted areas and faceting can be explained by dissolution of the large plastically relaxed islands if these are partially overgrown with GaAs and subsequently annealed [SGPL$^+$02]. The process of pit formation is schematically shown in Fig. 6.4(c). Thermodynamic calculations by Wang et al. [WKSL01] and also experimental investigations have shown that such dissolution is energetically favourable. On the top surface an In rich GaInAs layer remains [SG02, SGPL$^+$02]. The dissolution depends of course on the thickness of the GaAs capping layer. While for sample D, the 1.5 nm thick GaAs layer is too thin, for sample E the dissolution of the islands is quite effective and the height of the large islands is drastically decreased.

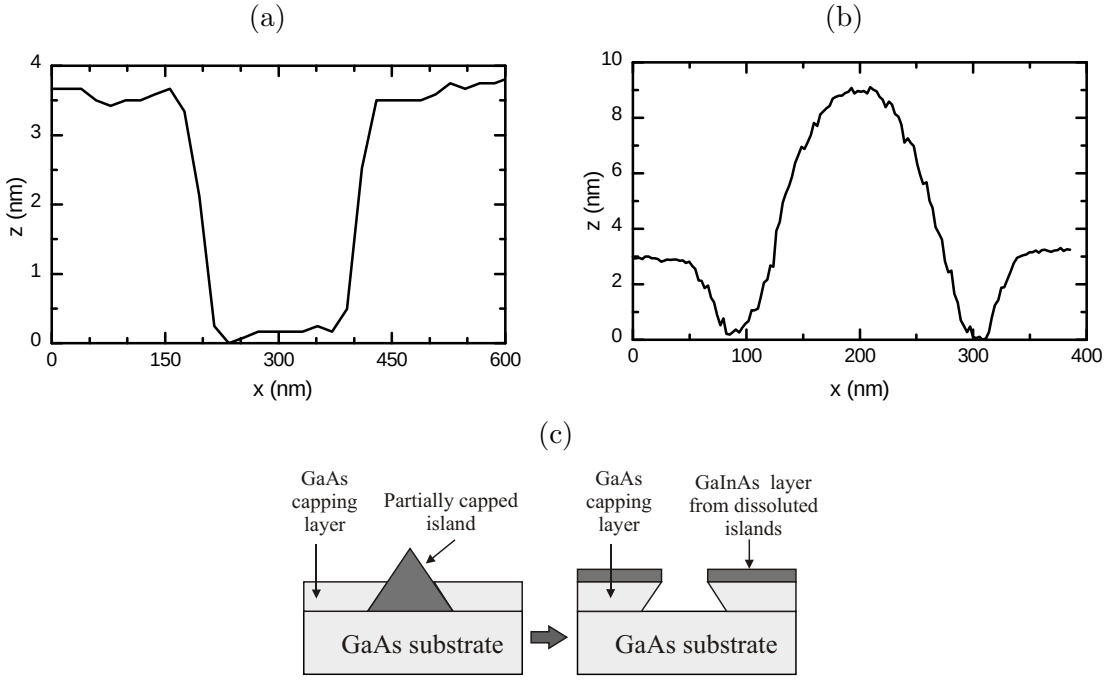

Figure 6.4. (a) Line-scan through one of the pits and (b) an island surrounded by a groove taken from an AFM image of sample E. (c) Schematic of the formation of pits by dissolution of partially capped islands during the annealing.

GID measurements

Radial scans measured in GID geometry are shown in Fig. 6.5. We observe a wide intensive peak around $Q_\mathrm{r} = 29.5$ nm^{-1} for all measured samples. In addition, a small peak occurs at $Q_\mathrm{r} = 30.5$ nm^{-1} for the samples A–C. The integral intensity of the peaks in the radial scans is approximately proportional to the square of the total volume on which X-rays are scattered. Thus, with reference to the TEM data (Tab. 6.1), we conclude that the peak

at $Q_r = 29.5$ nm^{-1} corresponds to the large plastically relaxed islands. The analysis of strain status and In content of these islands was done from XRD and it is postponed to the end of this section.

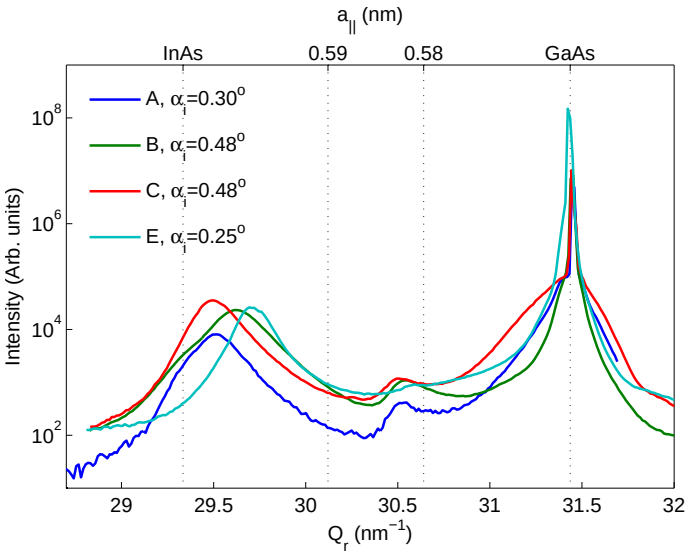

Figure 6.5. Radial scans around the (220) in-plane Bragg reflection for sample A, B, C and E. In-plane lattice parameter corresponding to Q_r coordinate is shown on the top axis. The incidence angle for the particular measurement is given in the legend.

The peak at $Q_r = 30.5$ nm^{-1} arise from the small plastically relaxed and large coherent islands. From the position of this peak we can estimate the mean in-plane lattice parameter of these islands to be $a_{\|} = 5.83\mathring{A}$. Thus their minimal In content determined from the Vegard's law [MS87] is 40 %. The intensity of the peak is lower for the sample C than for the samples A and B since the dislocation disappear from a part of the small plastically relaxed islands. The GaAs, deposited on a surface presenting plastically relaxed islands, could grow directly on them. This is however rather improbable, because it would imply an energetically expensive formation of a second dislocation array to accommodate the lattice mismatch between the plastically relaxed InGaAs island and the GaAs cap. Therefore this derelaxation effect can be attributed to a Ga enrichment of the small dislocated islands during the GaAs deposition [SGPMS02]. Finally, we do not observe any signal from the small plastically relaxed islands at $Q_r = 30.5$ nm^{-1} for sample E. We suppose that all small dislocated islands derelaxed and/or were dissolved during the annealing.

Angular scans through the diffuse scattering maximum corresponding to the large plastically relaxed islands in the vicinity of (220) in-plane Bragg reflections for sample A are shown in Fig. 6.6(a). For the analysis of these data the iso-strain scattering method (see Sec. 2.3) was used. The intensities of the angular scans taken at constant Q_r were fitted by a model function $I = A \cdot (\sin(q_a D_{iso}/2)/q_a)^2 + B$ [see Eq. (2.40)] as shown in Fig. 6.6(a). Here, the parameter D_{iso} is the diameter of the lateral cross-section of the island with a constant in-plane parameter $a_{\|} = 2\pi/Q_r\sqrt{8}$. The parameters A and B denote a proportionality constant and the detector background, respectively. The diameter D_{iso} of the lateral cross-section is plotted in Fig. 6.6(b) as a function of the in-plane lattice parameter $a_{\|}$. Complete relaxation of pure InAs corresponds to the lattice parameter value of 6.0583 Å. The decrease of D_{iso} with increasing $a_{\|}$ for $a_{\|} > 6.01$ Å corresponds to the

decreasing island diameter with increasing height of the lateral cross-sections through the island towards the apex of the plastically relaxed InAs islands. The increase of D_{iso} with increasing $a_{\parallel}$ for smaller values of $a_{\parallel} < 6.01$ Å originates from an overlap of signals from small coherent islands and large plastically relaxed islands in the corresponding angular scans [MMPN^{+}01].

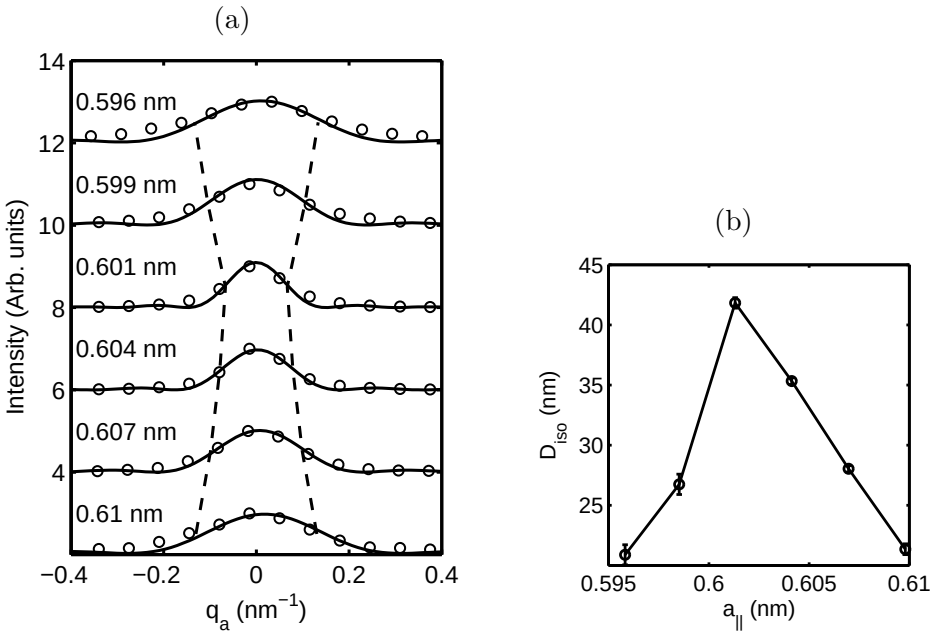

Figure 6.6. (a) Angular scans taken in the vicinity of the diffuse scattering maximum from the large plastically relaxed islands close to the (220) in-plane GaAs Bragg reflection for sample A. The experimental curves (circles) and their fits are shown. The in-plane lattice parameter $a_{\parallel}$ corresponding to the fixed Q_{r} is stated above each profile. The dashed line indicates evolution of the FWHM of the angular scans. (b) The widths D_{iso} of the areas of constant in-plane lattice parameter $a_{\parallel}$ and error-bars of D_{iso} derived from the fits of the angular scans in the panel (a).

High angle XRD

The XRD RSMs measured around (224) Bragg reflection of GaAs are shown in Fig. 6.2 for samples A–D. The diffuse scattering maximum near (224) Bragg reflection of InAs (indicated by circle in Fig. 6.2) occurs at $Q_x = 29.5$ nm^{-1}, which equals to the Q_r position of the intensive peak in (220) GID measurements (Fig. 6.5). Thus we conclude that this maximum corresponds to the large plastically relaxed islands. No maxima from the small plastically relaxed islands and large coherent islands are observed in XRD maps since the diffracting volume is too small. Due to the presence of plastically relaxed islands, the scattered intensities observed in XRD experiments are influenced by diffusely scattered intensity originating from dislocations. Thus one of the usual procedures for the analysis of elastically relaxed islands, based on a finite element calculations of the strain fields and correspondingly calculated diffracted intensities can not be used in this case. Consequently, we plot in the blow-ups of the asymmetric reciprocal space maps shown in Fig. 6.7 lines

of constant relaxation $R = \frac{a_{||}-a_{GaAs}}{a_{bulk}-a_{GaAs}}$, where $a_{||}$ denotes the in-plane lattice constant and a_{bulk} the corresponding one for a completely relaxed $\mathrm{In}_x\mathrm{Ga}_{1-x}\mathrm{As}$ alloy. In content x changes along the lines of constant relaxation and a_{bulk} is determined from the Vegard's law. Additionally, lines of constant In content are plotted in Fig. 6.7. From an inspection of these plots data on R and x_{In} of the large plastically relaxed islands were obtained and they are collected in Tab. 6.4. It is remarkable that capping of the islands with 1.5 nm GaAs and annealing at 620 °C already decreases the average In content of the dislocated islands from nearly 100 % to 60 %. This is due to inter-diffusion of In and Ga atoms from the InAs islands and the GaAs capping layer and substrate.

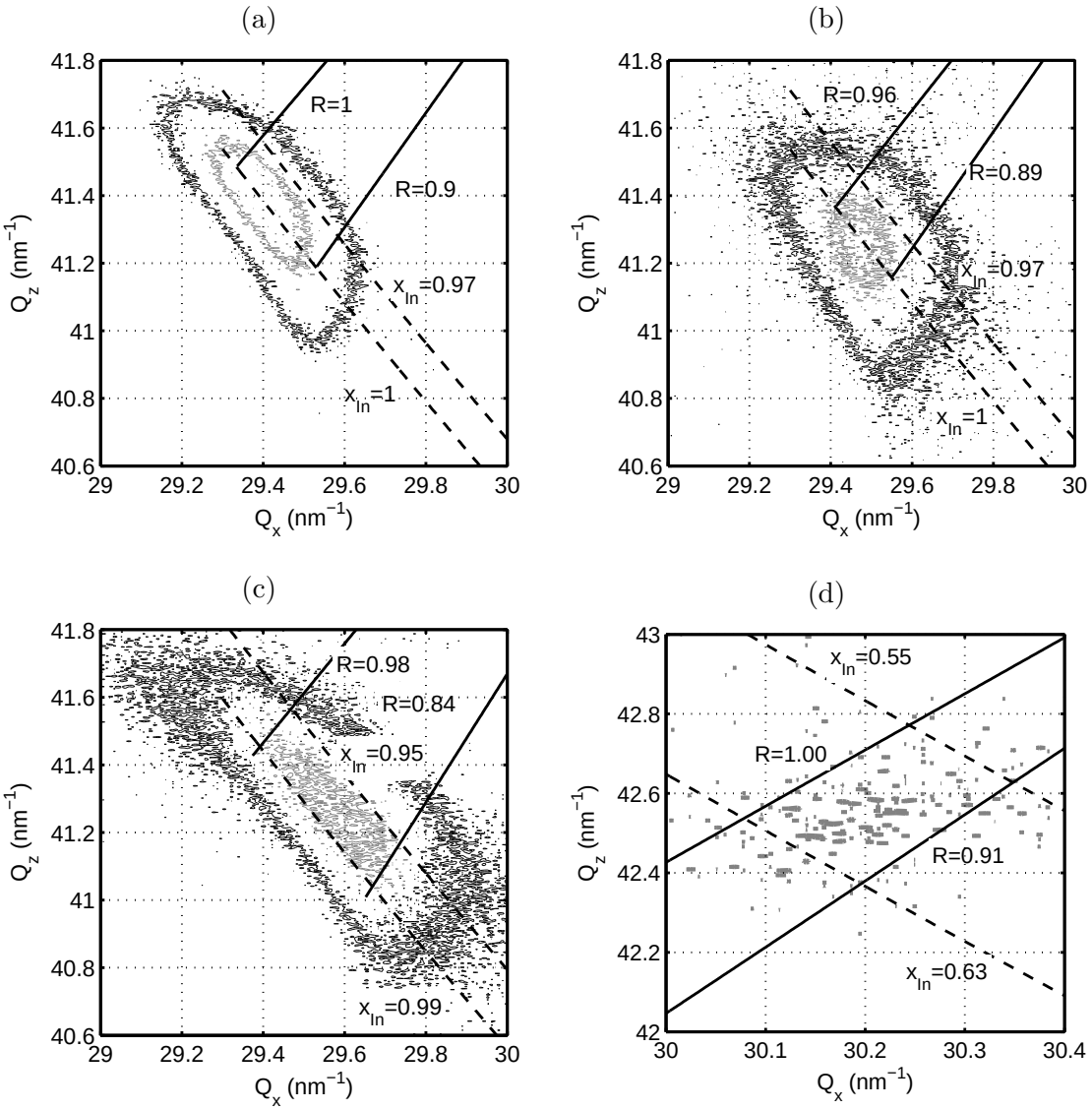

Figure 6.7. Blow-up of (224) reciprocal space maps of samples A–D (from left to right and from top to bottom) with lines indicating constant degree of relaxation R and constant In-content x_{In}. The iso-lines of constant intensities are plotted for 20 %, 50 % and 80 % of the diffuse intensity maximum for samples A, B and C. For the sample D iso-lines are plotted for 60 % of the diffuse intensity maximum only.

	A	B	C	D
R (%)	90–100	89–96	84–97	91–100
x_{In}	97–100	97–100	95–99	55–63

Table 6.4. Relaxation degree R and In content x_{In} in large dislocated islands obtained from XRD.

6.4 Conclusions

A series of samples with different populations of InAs and GaInAs islands, grown by LP-MOVPE was investigated by atomic force microscopy as well as by X-ray diffraction techniques. The latter give information on the composition and the strain status of the islands. The dominant signals in X-ray diffraction arise from plastically relaxed islands. The overgrowth of the InAs islands with GaInAs results in an additional nucleation of islands on the wetting layer already present, as already shown in previous TEM studies of these samples. Furthermore, the annealing of the samples D and E at 620 °C leads to the dissolution of partially capped InAs islands and the inter-diffusion In and Ga atoms from the InAs islands and GaAs capping layer and substrate, respectively.

Acknowledgments

The samples were grown by G. Saint-Girons (LPN Paris, France). A part of the X-ray measurements was performed by Dr. J. Stangl and Dr. R. T. Lechner (both JKU Linz). A part of the the AFM images was taken by A. Rehman and U. Kainz (both JKU Linz). We acknowledge staff of Institute of Aerospace Engineering of Brno University of Technology for providing computer time on their SGI computer to perform finite element calculations of stress fields in the islands (see Appendix B).

Chapter 7

Conclusions

The thesis focuses on structural characterizations of semiconductor quantum dots (QDs) and nano-islands (NIs) by means of X-ray diffraction (XRD). InAs/GaAs QDs and Ge/Si NIs grown in Stranski-Krastanow growth mode were studied by means of coplanar high-angle XRD and experiments in grazing-incidence diffraction (GID) geometry. To perform our investigations, we have established new methods for characterization of buried NIs and NIs ordered in three-dimensional island crystals. The results of X-ray analysis were correlated with results obtained by atomic force microscopy, transmission electron microscopy, photoluminescence, and band gap calculations. The studies brought useful information on the investigated NI structures and their changes during capping. The main contributions of the work can be divided into methodological and sample analysis parts.

Methodology

1. We have introduced a generalization of the iso-strain scattering method (ISSM) [KML$^+$01] for buried NIs (Chap. 3). The method allows for the characterization of strain fields in buried NIs and obtaining the geometry (shape and size) of NIs from X-ray grazing-incidence diffraction data without any model assumption on the island shape. Simulations for various spatial correlations of the NI positions have been shown and limitations of the method have been discussed. The method has been applied for an analysis of InAs QDs (Sec. 4.1). Though the full characterization of QDs required to perform additional strain calculations using a model of the QDs, the results from iso-strain scattering yielded a good starting point and additional constraints for the model fitting procedure.

2. ISSM was applied to obtain structural information on the topmost QD layer of an 11-stack multilayer of laterally ordered and unorder QDs (Sec. 4.2). Though X-ray scattering signals from both the ordered and the unordered QDs were mixed in the measured X-ray data, we were able to extract structural information on each class of QDs separately. Additionally, we have presented a method to determine the mean deviation of the QD positions from the perfect 2D lattice sites from X-ray scattering on ordered QDs.

3. We have demonstrated that the combination of an analytical solution of the equilibrium equations of linear elasticity with kinematical scattering theory can be used for studies on 3D NI crystals (Chap. 5). The method is applicable for analysis of data measured in coplanar high-angle XRD.

Studied nano-island structures

Here we summarize main results obtained for studied InAs/GaAs and Ge/Si NIs. For more detailed summaries is the reader referenced to conclusions of corresponding sections.

1. InAs/GaAs QDs grown by molecular beam epitaxy (MBE) at low growth rates were investigated (Chap. 4) by means of GID. The QDs were found to be elongated along the $[1\bar{1}0]$ in-plane direction due to the anisotropy in the surface diffusion of In and Ga atoms.

   (a) Capping of InAs QDs at 460 °C and subsequent annealing at 580 °C resulted in the reduction of the QD lateral size from 60 nm, observed before the capping, to 22 nm [Sec. 4.1]. The In content in the QDs decreased from 100 % to 70 %.

   (b) An 11-stack multilayer of laterally ordered and unorder QDs was studied in Sec. 4.2. No substantial difference was found in the size and shape of the laterally ordered and unordered dots. The lateral size of uncapped QDs (i.e., QDs in the topmost QD layer) along the $[1\bar{1}0]$ direction was found to be 70 nm. These QDs are covered with an oxide layer of approximate thickness 5 nm. The root mean square displacement of the laterally ordered QDs in the topmost QD layer from their ideal lattice sites was found to be $\sigma = (7.0 \pm 0.5)$ nm. This result is in a good agreement with an analysis of the QD positions in an AFM image of the ordered QDs. QDs are located on elevated structures (ridges) spread along the $[1\bar{1}0]$ direction. Both the laterally ordered and unordered QDs are vertically stacked in columns.

   An interesting direction of further research of this type of QD multilayers would be the determination of the chemical composition of the dots and of the ridges underneath the dots. Such investigations could help to clarify the mechanism of the ridges formation. Additionally structural characterization of the buried dots should be possible by means of high-angle X-ray diffraction and the data analysis presented in Chap. 5. Nevertheless, the analysis would be complicated by the presence of the ridges underneath the dots.

2. MBE-grown Ge/Si NIs forming a 3D island crystal were studied by high-angle XRD in Chap. 5. The islands have {105} facets characteristic for Ge pyramids. The lateral island size is about (170 ± 20) nm, and their height turned out to be (19 ± 4) nm. The Ge content in the capped islands is about (40 ± 10) %. The surprisingly high energy of no-phonon PL from the islands (915 meV) is explained by transitions involving states in conduction band minima perpendicular to the growth direction, which resides in Si matrix (spatially indirect PL transition).

The spatially indirect PL transitions should be further investigated. Its existence critically depends on the island chemical composition, which can be obtained from coplanar high angle XRD measurements in combination with our method for the data evaluation presented in Chap. 5.

3. A series of samples with InAs/GaAs islands grown by low-pressure metal-organic vapour-phase-epitaxy (LP MOVPE), effects of NI capping with Ga(In)As, and effects of annealing were studied by means of X-ray diffraction and AFM in Chap. 6. Our results were correlated with previous TEM studies. In contrast to MBE grown QDs, deposition of InAs by LP MOVPE resulted in three types of QDs differing by size and relaxation state. Larger QDs are plastically relaxed, i.e., with dislocations, while the small are elastically relaxed. The overgrowth of the InAs islands with GaInAs resulted in an additional nucleation of islands on the wetting layer already present. Furthermore, the annealing of samples capped with GaAs led to the dissolution of partially capped InAs islands and the inter-diffusion of In and Ga atoms from the InAs islands and GaAs capping layer. Finally, we have demonstrated a calculation of the first-order energy of a dislocation in an island similar to that observed for the LP MOVPE samples (Appendix B).

Appendix A

Calculation of displacement field in buried islands

Here we give details on calculation of the displacement field in buried islands ordered in a laterally periodic lattice. We used the calculations for simulation of X-ray scattering on a Ge/Si island crystal in Chap. 5. The calculation is based on the analytical solution of the elastic equilibrium equation (see Sec. 5.3.2).

The coefficients of the set of linear differential equations (5.9) are given by matrices

$$\hat{\mathbf{A}} = \begin{pmatrix} C_{44} & 0 & 0 \\ 0 & C_{44} & 0 \\ 0 & 0 & C_{11} \end{pmatrix}, \tag{A.1}$$

$$\hat{\mathbf{B}} = \begin{pmatrix} 0 & 0 & K_x(C_{12}+C_{44}) \\ 0 & 0 & K_y(C_{12}+C_{44}) \\ K_x(C_{12}+C_{44}) & K_y(C_{12}+C_{44}) & 0 \end{pmatrix}, \text{ and}$$

$$\hat{\mathbf{C}} = \begin{pmatrix} K_x^2C_{11}+K_y^2C_{44} & K_xK_y(C_{12}+C_{44}) & 0 \\ K_xK_y(C_{12}+C_{44}) & K_x^2C_{44}+K_y^2C_{11} & 0 \\ 0 & 0 & (K_x^2+K_y^2)C_{44} \end{pmatrix}.$$

And the 2D Fourier transform of the volume force is

$$\mathbf{P} = \delta \begin{pmatrix} iK_x g^{\mathrm{F}}_{\mathbf{K}}(z) \\ iK_y g^{\mathrm{F}}_{\mathbf{K}}(z) \\ (g^{\mathrm{F}}_{\mathbf{K}}(z))' \end{pmatrix}. \tag{A.2}$$

The boundary conditions for each Fourier coefficient $\mathbf{u}^{\mathrm{F}}_{\mathbf{G}}$ are

$$\hat{\mathbf{A}}(\mathbf{u}^{\mathrm{F}}_{\mathbf{K}})' + i\hat{\mathbf{M}}\mathbf{u}^{\mathrm{F}}_{\mathbf{K}}|_{z=D, z\to-\infty} = 0, \tag{A.3}$$

where

$$\hat{\mathbf{M}} = \begin{pmatrix} 0 & 0 & K_x C_{44} \\ 0 & 0 & K_y C_{44} \\ K_x C_{12} & K_y C_{12} & 0 \end{pmatrix}. \tag{A.4}$$

The solution of Eq. (5.9) is a sum of a general solution $\mathbf{u}_{\mathrm{g}}^{\mathrm{F}}$ of the set of a homogeneous differential equations

$$\hat{\mathbf{A}}(\mathbf{u}_{\mathrm{g}}^{\mathrm{F}})'' + i\hat{\mathbf{B}}(\mathbf{u}_{\mathrm{g}}^{\mathrm{F}})' - \hat{\mathbf{C}}\mathbf{u}_{\mathrm{g}}^{\mathrm{F}} = 0 \tag{A.5}$$

and a particular solution $\mathbf{u}_{\mathrm{p}}^{\mathrm{F}}$ of the full Eq. (5.9). The general solution of Eq. (A.5) is a linear combination of the eigensolutions

$$\mathbf{u}_{\mathrm{g}}^{\mathrm{F}}(\mathbf{K}, z) = \sum_{n=1}^{6} c_n(\mathbf{K}) \mathbf{u}_{\mathrm{g}\,n}(\mathbf{K}) e^{i\kappa_n(\mathbf{K})z}, \tag{A.6}$$

where $\kappa_{1,\ldots,6}$ are roots of the characteristic equation $\det[\hat{\mathbf{W}}(\mathbf{K}, \kappa)] = 0$,

$$\hat{\mathbf{W}}(\mathbf{K}, \kappa) = \hat{\mathbf{A}}\kappa^2 + \hat{\mathbf{B}}\kappa + \hat{\mathbf{C}}, \tag{A.7}$$

and $\mathbf{u}_n$ are the corresponding eigenvectors

$$\hat{\mathbf{W}}(\mathbf{K}, \kappa_n)\mathbf{u}_{\mathrm{g}\,n} = 0. \tag{A.8}$$

The particular solution of Eq. (5.9) can be found by applying the Fourier transform (FT) over z to both sides of the equation. For the FT of the particular solution

$$\mathbf{u}_{\mathrm{p}}^{\mathrm{FF}}(\mathbf{K}, q) = \frac{1}{2\pi} \int_{-\infty}^{\infty} \mathrm{d}z\, \mathbf{u}_{\mathrm{p}}^{\mathrm{F}}(\mathbf{K}, z) e^{-iqz}, \tag{A.9}$$

where the second superscript F stands for FT over z, we obtain a matrix equation

$$\mathbf{u}_{\mathrm{p}}^{\mathrm{FF}}(\mathbf{K}, q) = -[\hat{\mathbf{W}}(\mathbf{K}, q)]^{-1} \mathbf{P}^{\mathrm{FF}}(\mathbf{K}, q). \tag{A.10}$$

In order to obtain the particular solution $\mathbf{u}_{\mathrm{p}}^{\mathrm{F}}(\mathbf{K}, z)$ in the z domain we apply the inverse FT to both sides of Eq. (A.10). The residual theorem is applied for the evaluation of the inverse FT of the right hand side. Finally, we obtain the expression for the Fourier coefficients of the displacement field

$$\begin{aligned} \mathbf{u}_{\mathbf{K}}^{\mathrm{F}}(\mathbf{R}, z) = & \sum_{m=1,\ldots,6} c_m(\mathbf{K}) \mathbf{u}_{\mathrm{g}\,m}(\mathbf{K}) e^{i\kappa_m(\mathbf{K})z} \\ & + \frac{\delta}{C_{11}C_{44}^2} \left[\sum_{n^+} \mathbf{u}_{\mathrm{p}\,n^+}(\mathbf{K}) G^+(\mathbf{K}, \kappa_{n^+}, z) e^{i\kappa_{n^+}z} \right. \\ & \left. - \sum_{n^-} \mathbf{u}_{\mathrm{p}\,n^-}(\mathbf{K}) G^-(\mathbf{K}, \kappa_{n^-}, z) e^{i\kappa_{n^-}z} \right], \end{aligned} \tag{A.11}$$

where κ_{n^+} and κ_{n^-} denote eigenvalues with positive and negative imaginary parts, respectively,

$$G^+(\mathbf{K},\kappa,z) = \frac{1}{S}\int_S \mathrm{d}\mathbf{R}\int_{-\infty}^{z} \mathrm{d}z'\, g(\mathbf{R},z')e^{-i(\mathbf{KR}+\kappa z')}$$

$$G^-(\mathbf{K},\kappa,z) = \frac{1}{S}\int_S \mathrm{d}\mathbf{R}\int_{z}^{D} \mathrm{d}z'\, g(\mathbf{R},z')e^{-i(\mathbf{KR}+\kappa z')}, \tag{A.12}$$

and (A.13)

$$\mathbf{u}_{\mathrm{p}\,n}(\mathbf{K}) = \frac{1}{\prod_{j\neq n}(\kappa_n-\kappa_j)}\hat{\mathbf{W}}^+(\mathbf{K},\kappa_n)\begin{pmatrix}K_x\\K_y\\\kappa_n\end{pmatrix}. \tag{A.14}$$

Here, $\hat{\mathbf{W}}^+$ denotes a matrix adjoint to $\hat{\mathbf{W}}$. The coefficients c_m are determined by applying the boundary conditions (A.3). From the boundary condition at the rare surface ($z \to -\infty$) $c_{n^+} = 0$ follows. The remaining three coefficients c_{n^-} are obtained after substitution of the general solution (A.11) into the boundary condition at $z = D$, which yields a set of 3 linear algebraic equations. Finally, the displacement field $\mathbf{u}(\mathbf{R},z)$ is obtained by substitution of the Fourier coefficients $\mathbf{u}^{\mathrm{F}}_{\mathbf{K}}$ into the Fourier series (5.8a).

Appendix B

Energetics of a misfit dislocation in an InAs island

In Chap. 6 we have reported on investigations on samples with plastically relaxed In(Ga)As islands. From TEM images it followed that the dislocations in the islands are 90° dislocations with the dislocation line along in-plane ⟨110⟩ directions. In this appendix we present a calculation of the first-order energy of a 90° edge dislocation introduced into an island. We apply the approach for calculations of dislocation energies in equilibrium two-dimensional islands used by B. J. Spencer and J. Tersoff in Refs. [ST00, ST01]. In the first section of this appendix we extend their calculations to three-dimensional islands in order to estimate the dislocation energy in the islands investigated in Chap. 6 and to determine the equilibrium position of the dislocation.

Theory

The stress distribution in an island and substrate can be used to give a first-order estimate of the energy required to introduce a dislocation into the system. In general, the total energy of introducing a dislocation into an island consist of a term which is linear in the Burgers vector $\mathbf{b}$, and terms which are of higher order in $\mathbf{b}$. The higher order terms are essential to understanding when it is energetically favourable to introduce a dislocation [ST00]. However, the calculation of these terms would require to consider all the problematic terms such as image forces and self-interaction energy of the dislocations.

The first-order energy of a dislocation is due to the force on the dislocation from the stress in the island and substrate. A line element $\mathrm{d}\mathbf{s}$ of an dislocation experiences a Peach-Koehler force [PK50]

$$\mathrm{d}\mathbf{F} = (\mathbf{b} \cdot \sigma) \times \mathrm{d}\mathbf{s} = \epsilon_{ijk} \mathbf{e}_i b_l \sigma_{lj} \mathrm{d}s_k \tag{B.1}$$

where $\mathbf{b}$ is the Burgers vector of the dislocation, ϵ_{ijk} $[i, j, k \in (x, y, z)]$ is the total antisymmetric tensor, $\mathbf{e}_i$ are the unit vectors of the Cartesian coordinate system, and $\hat{\sigma}$ is the stress due to the lattice mismatch. In accordance with TEM observations for In(Ga)As

islands mentioned above, we consider an edge dislocation with the dislocation line along $[1\bar{1}0]$ (along y-axis) and the Burgers vector $\mathbf{b} = (b_x, b_y, b_z)$. The coordinate system orientation is shown in Fig. B.1. If the dislocation is placed on the surface of the substrate with the island at point **S**, the energy required to move the dislocation line against the Peach-Koehler force to any point **R** inside the island or substrate is

$$E(\mathbf{R}) = -\int_{\mathbf{S}}^{\mathbf{R}} \mathrm{d}\mathbf{p} \int_{\mathcal{S}(\mathbf{p})} \mathrm{d}\mathbf{F}, \tag{B.2}$$

where **p** is the path from surface point **S** to interior point **R**. The second integral in Eq. (B.2) is performed along the part of the dislocation line $\mathcal{S}(\mathbf{r})$ embedded in the sample. Since the dislocation penetrates all the sample along the y-axis, it is sufficient to investigate the energy of the dislocation as function of the X, Z coordinates. Additionally, the force $\mathrm{d}\mathbf{F}$ is conservative and the integral of Eq. (B.2) is path independent, if $\hat{\sigma}(\mathbf{r})$ corresponds to the mechanical equilibrium. We choose the energy at the sample surface to be $E = 0$ and we performed the path integral from a surface point $(X, h(X))$ along the vertical z-axis to the point (X,Z). Eq. (B.2) then reduces to

$$E(X, Z) = \int_{Z}^{h(X)} \mathrm{d}z \int_{Y_1(X,z)}^{Y_2(X,z)} \mathrm{d}y [b_x \sigma_{xx} + b_z \sigma_{zx}]. \tag{B.3}$$

Here, the second integral is again performed along the dislocation line, i.e., along the y-axis. $Y_1(X, z)$ and $Y_2(X, z)$ are intersections of the dislocation line with the island surface or sample sides.

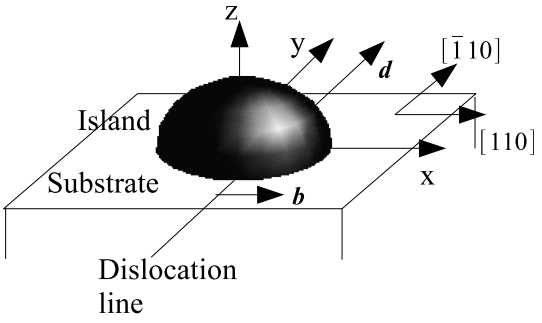

Figure B.1. Scheme of the axis orientation and orientation of the dislocation line **d** for purposes of the calculations of the dislocation first-order energy.

Practical realization of the first-order energy calculation

For the calculation of the first-order dislocation energy, we need to assume a model of the island shape and the profile of the chemical composition throughout the island. From this, the stress distribution is obtained by solving equations of linear continuum elasticity. The solution was performed using the numerical finite element method (FEM). The FEM was in recent years successfully applied to calculate strain and stress in nanostructures [CASM94, WSH$^+$00, HSH$^+$02, ASG$^+$04]. In our case, we used FEM solver software Nastran and its preprocessor Patran for the stress calculations. The description of the application of these programs for such calculations is beyond the scope of this thesis and it is well

described in Ref. [May01]. The energy of the dislocation was then numerically calculated by substituting the stress distribution obtained from FEM into Eq. (B.3). The integral over the dislocation line was performed for a substrate of some "arbitrary" size, roughly corresponding to the average island distance. Thus, while the absolute energy values might be incorrect to some extent, the dependence of the dislocation energy on (X, Z), and in particular the location of the energy minimum, should be very well reproduced by the calculations.

Results and discussion

For our calculations we assumed the island model shape of a truncated rotational paraboloid. In particular, we present here a calculation for an island of bottom radius $R_\mathrm{b} = 40$ nm, top radius $R_\mathrm{t} = 15$ nm and height $h = 6$ nm. Such island proportions correspond to small plastically relaxed In(Ga)As islands described in Chap. 6. We assumed an InGaAs island with In content of $x_\mathrm{In} = 97$ %. The wetting layer underneath the island was assumed to have the same In content of 97 % and height of 1 nm. A pure GaAs (001) substrate with a lateral size of 300×300 nm was assumed in the model. In accordance with TEM observations mentioned in Chap. 6 we assumed a 90° dislocation with the dislocation line along the $[1\bar{1}0]$ direction and the Burgers vector along [110]. The presented calculation was performed for a pure edge dislocation with the Burgers vector $\mathbf{b} = (0, a_\mathrm{GaAs}, 0)$, where $a_\mathrm{GaAs} = 0.565325$ nm is the lattice constant of GaAs.

The resulting dislocation energy distribution in the (x, z) plane is shown in Fig. B.2(a). We observe an dislocation energy minimum of $E_\mathrm{min} = -7.6$ keV at the interface of the wetting layer and the substrate in the centre of the island. The energy minimum corresponds to the equilibrium dislocation position. The orientation of the dislocation line and the Burgers vector of the dislocation corresponds to an extra lattice plane in (y, z) plane inserted within the substrate. Such an result can be expected since the lattice constant of GaAs is smaller than the lattice constant of InAs. The only stress component which influences the first-order energy of the dislocation under investigation is σ_{xx} [see Eq. (B.3)]. Spatial distribution of σ_{xx} in the (x, z) plane going through the center of the island is shown in Fig. B.2(b). The compressive stress σ_{xx} in the island and the wetting layer tends to push the dislocation down towards the wetting layer/substrate interface. The $\sigma_{xx}(\mathbf{r})$ and $E(x, z)$ spatial distributions are symmetric with respect to (y,z) plane. In agreement with our calculation, dislocations at the island/substrate interface were observed in TEM images of samples reported in Chap. 6.

We can do several additional qualitative conclusions about the dislocation energies without need of any further explicit calculations. First, the energy distribution in (y, z) for the 90° dislocation with the dislocation line along the $[\bar{1}\bar{1}0]$ direction and the Burgers vector along $[\bar{1}10]$ would be the same as shown in Fig. B.2(a), since the crystal structure of the sample is invariant with respect to the 90° rotation around the z-axis. Second, reverting the direction of the Burgers vector to $\mathbf{b} = (0, -a_\mathrm{GaAs}, 0)$ results in changing the sign of the energy in Fig. B.2(a). This orientations of the dislocation line $\mathbf{d}$ and

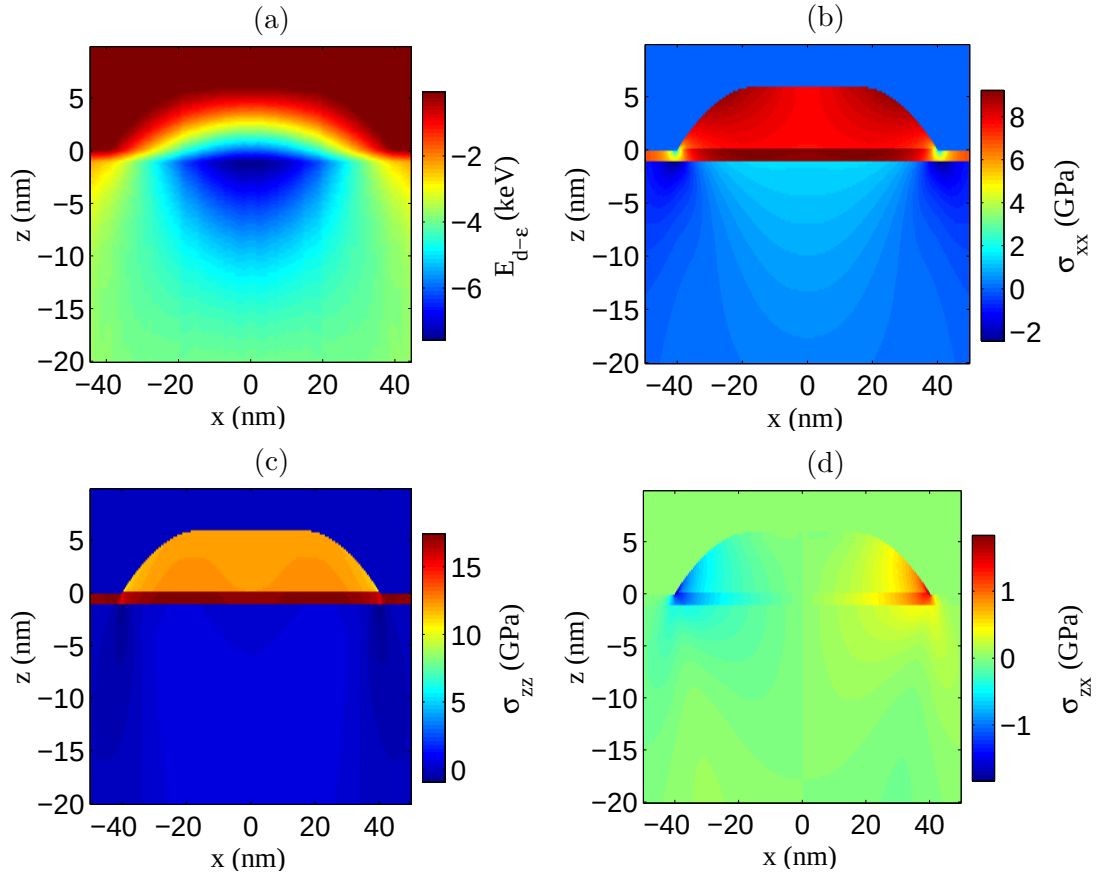

Figure B.2. (a) First-order energy of a 90° dislocation in an island and underlying substrate. (b-d) Components of the elastic stress due to the misfit between the island and the substrate. The stress is plotted within the (x, z) plane going through the center of the island.

Burgers vector $\mathbf{b}$ correspond to introducing an extra lattice plane along the (y, z) plane into the compressively stressed island, which is energetically unfavourable. Third, as follows from Eq. (B.3), the first-order dislocation energy is independent from any Burgers vector component b_y for a straight dislocation with the dislocation line along y-axis. In particular, there is no first order interaction between a pure screw dislocation and the elastic stress in the island. Finally, the $\sigma_{zx}(\mathbf{r})$ stress component, which influences the dislocation energy [see Eq. (B.3)], is plotted in Fig. B.2 for our island model. Here, σ_{zx} is antisymmetric with respect to the mirror plane (y, z), i.e., $\sigma_{zx}(x, y, z) = -\sigma_{zx}(-x, y, z)$. Thus, for a dislocation with the dislocation line along y-axis and non-zero Burgers vector component b_z, the dislocation energy distribution $E(x, z)$ would be asymmetric with respect to z-axis. The equilibrium dislocation position would be biased to the left or right side of the island [ST01].

Bibliography

[ADFO99] A. D. Andreev, J. R. Downes, D. A. Faux, and E. P. O'Reilly. Strain distributions in quantum dots of arbitrary shape. *J. Appl. Phys.*, 86(1):297–305, 1999.

[ASG+04] A. Alizadeh, P. Sharma, S. Ganti, S. F. LeBoeuf, and L. Tsakalakos. Templated wide band-gap nanostructures. *J. Appl. Phys.*, 95(12):8199–8206, 2004.

[BGL99] D. Bimberg, M. Grundmann, and N. N. Lendentsov. *Quantum Dot Heterostructures*. Wiley, New York, 1999.

[Bim05] D. Bimberg. Quantum dots for lasers, amplifiers and computing. *J. Phys. D: Appl. Phys.*, 38(13):2055–2058, 2005.

[Bru02] K. Brunner. Si/Ge nanostructures. *Rep. Prog. Phys.*, 65(1):27–72, 2002.

[BZS03] M Borgström, V Zela, and W Seifert. Arrays of Ge islands on Si(001) grown by means of electron-beam pre-patterning. *Nanotech.*, 14(2):264–267, 2003.

[CASM94] S. Christiansen, M. Albrecht, H. P. Strunk, and H. J. Maier. Strained state of Ge(Si) islands on Si: Finite element calculations and comparison to convergent beam electron-diffraction measurements. *Appl. Phys. Lett.*, 64(26):3617–3619, 1994.

[CDB+06] V. Chamard, M. Dollé, G. Baldinozzi, F. Livet, M. de Boissieu, F. Bley, P. Donnadieu, T.H. Metzger, C. Mocuta, F. Picca, S. Labat, and O. Thomas. Getting smaller and smaller: Coherent microdiffraction imaging to retrieve shape and local strain of a single nanocrystal. http://www.esrf.fr/NewsAndEvents/Spotlight/spotlight33nano/, 2006.

[CKH+04] O. Caha, V. Křápek, V. Holý, S. C. Moss, J. H. Li, A. G. Norman, A. Mascarenhas, J. L. Reno, J. Stangl, and M. Meduňa. X-ray diffraction on laterally modulated $InAs_n/AlAs_m$ short-period superlattices. *J. Appl. Phys.*, 96(9):4833, 2004.

[CRM+04] G. Costantini, A. Rastelli, C. Manzano, R. Songmuang, O. G. Schmidt, K. Kern, and H. von Känel. Universal shapes of self-organized semiconductor quantum dots: Striking similarities between InAs/GaAs(001) and Ge/Si(001). *Appl. Phys. Lett.*, 85(23):5673–5675, 2004.

[DHS+97] A. A. Darhuber, V. Holy, J. Stangl, G. Bauer, A. Krost, F. Heinrichsdorff, M. Grundmann, D. Bimberg, V. M. Ustinov, P. S. Kop'ev, A. O. Kosogov, and P. Werner. Lateral and vertical ordering in multilayered self-organized InGaAs quantum dots studied by high resolution x-ray diffraction. *Appl. Phys. Lett.*, 70(8):955–957, 1997.

[DSH+97] A. A. Darhuber, P. Schittenhelm, V. Holý, J. Stangl, G. Bauer, and G. Abstreiter. High-resolution x-ray diffraction from multilayered self-assembled Ge dots. *Phys. Rev. B*, 55(23):15652—-15663, 1997.

[DSS03] U. Denker, M. Stoffel, and O.G. Schmidt. Probing the lateral composition profile of self-assembled islands. *Phys. Rev. Lett.*, 90(19):196102, 2003.

[FHZ03] P F Fewster, V Holý, and D Zhi. Composition determination in quantum dots with in-plane scattering compared with STEM and EDX analysis. *J. Phys. D: Appl. Phys.*, 36(10A):A217–A221, 2003.

[Fro] T. Fromherz et al., to be published.

[GLX+98] Q. Gong, J.B. Liang, B. Xu, D. Ding, H.X. Li, C. Jiang, W. Zhou, F.Q. Liu, Z.G. Wang, X.H. Qiu, G.Y. Shang, and C.L. Bai. Analysis of atomic force microscopic results of InAs islands formed by molecular beam epitaxy. *J. Cryst. Growth*, 192:376, 1998.

[GMRS+97] J. M. Garcia, G. Medeiros-Ribeiro, K. Schmidt, T. Ngo, J. L. Feng, A. Lorke, J. Kotthaus, and P. M. Petroff. Intermixing and shape changes during the formation of InAs self-assembled quantum dots. *Appl. Phys. Lett.*, 71(14):2014–2016, 1997.

[GXS+05] B. D. Gates, Qiaobing Xu, M. Stewart, D. Ryan, C. G. Willson, and G. M. Whitesides. New approaches to nanofabrication: Molding, printing, and other techniques. *Chem. Rev.*, 105(4):1171–1196, 2005.

[HLH+03] C.-H. Hsu, H.-Y. Lee, Y.-W. Hsieh, Y.P. Stetsko, M.-T. Tag, K.S. Liang, N.T. Yeh, J.-I. Chyi, and D.Y. Noh. X-ray scattering studies on InGaAs quantum dots. *Physica B*, 336:98, 2003.

[HPB99] V. Holý, U. Pietsch, and T. Baumbach. *High-Resolution X-ray scattering from Thin Films and Multilayers*, volume 149 of *Springer Tracts in Modern Physics*. Springer-Verlag, 1999.

[HSG+04] M. Hanke, M. Schmidbauer, D. Grigoriev, H. Raidt, P. Schafer, R. Kohler, A.-K. Gerlitzke, and H. Wawra. SiGe/Si(001) Stranski-Krastanow islands by liquid-phase epitaxy: Diffuse x-ray scattering versus growth observations. *Phys. Rev. B*, 69(7):075317, 2004.

[HSH+02] A. Hesse, J. Stangl, V. Holý, T. Roch, G. Bauer, O.G. Schmidt, U. Denker, and B. Struth. Effect of overgrowth on shape, composition, and strain of SiGe islands on Si(001). *Phys. Rev. B*, 66(8):085321, 2002.

[HSPB99] V. Holý, G. Springholz, M. Pinczolits, and G. Bauer. Strain induced vertical and lateral correlations in quantum dot superlattices. *Phys. Rev. Lett.*, 83(2):356, 1999.

[HSS+00] V. Holý, J. Stangl, G. Springholz, M. Pinczolits, G. Bauer, I. Kegel, and T.H. Metzger. Lateral and vertical ordering of self-assembled PbSe quantum dots studied by high-resolution x-ray diffraction. *Physica B*, 283:65, 2000.

[JKBJ01] P. B. Joyce, T. J. Krzyzewski, G. R. Bell, and T. S. Jones. Surface morphology evolution during the overgrowth of large InAs–GaAs quantum dots. *Appl. Phys. Lett.*, 79(22):3615–3617, 2001.

[JLW00] G. Jin, J. L. Liu, and K. L. Wang. Regimented placement of self-assembled Ge dots on selectively grown Si mesas. *Appl. Phys. Lett.*, 76(24):3591–3593, 2000.

[KAT01] L. P. Kouwenhoven, D. G. Austing, and S. Tarucha. Few-electron quantum dots. *Rep. Prog. Phys.*, 64(6):701–736, 2001.

[KCB04] O. Kermarrec, Y. Campidelli, and D. Bensahel. ABAB organization of Ge/Si(001) islands in multiplanes grown with low pressure chemical vapor deposition. *J. Appl. Phys.*, 96(11):6175–6182, 2004.

[KHS04] S. Kiravittaya, H. Heidemeyer, and O.G. Schmidt. Growth of three-dimensional quantum dot crystals on patterned GaAs (001) substrates. *Phys. E*, 23:253, 2004.

[KHS05] S. Kiravittaya, H. Heidemeyer, and O. G. Schmidt. Lateral quantum-dot replication in three-dimensional quantum-dot crystals. *Appl. Phys. Lett.*, 86(26):263113, 2005.

[KMF+99] I. Kegel, T. H. Metzger, P. Fratzl, J. Peisl, A. Lorke, J. M. Garcia, and P. M. Petroff. Interdependence of strain and shape in self-assembled coherent InAs islands on GaAs. *Europhys. Lett.*, 45(2):222, 1999.

[KML+00] I. Kegel, T. H. Metzger, A. Lorke, J. Peisl, J. Stangl, G. Bauer, J. M. García, and P. M. Petroff. Nanometer-scale resolution of strain and interdiffusion in self-assembled InAs/GaAs quantum dots. *Phys. Rev. Lett.*, 85(8):1694, 2000.

[KML+01] I. Kegel, T. H. Metzger, A. Lorke, J. Peisl, J. Stangl, G. Bauer, K. Nordlund, W. V. Schoenfeld, and P. M. Petroff. Determination of strain fields and composition of self-organized quantum dots using x-ray diffraction. *Phys. Rev. B*, 63:035318, 2001.

[KMP+99] I. Kegel, T. H. Metzger, J. Peisl, J. Stangl, G. Bauer, and D. Smilgies. Vertical alignment of multilayered quantum dots studied by x-ray grazing-incidence diffraction. *Phys. Rev. B*, 60(4):2516, 1999.

[KMR+05] B. Krause, T. H. Metzger, A. Rastelli, R. Songmuang, S. Kiravittaya, and O. G. Schmidt. Shape, strain, and ordering of lateral InAs quantum dot molecules. *Phys. Rev. B*, 72(8):085339, 2005.

[Kri05] S. Krishna. Quantum dots-in-a-well infrared photodetectors. *J. Phys. D: Appl. Phys.*, 38(13):2142–2150, 2005.

[KRS05] S. Kiravittaya, A. Rastelli, and O. G. Schmidt. Self-assembled InAs quantum dots on patterned GaAs(001) substrates: Formation and shape evolution. *Appl. Phys. Lett.*, 87(24):243112, 2005.

[KRS06] S. Kiravittaya, A. Rastelli, and O. G. Schmidt. Photoluminescence from seeded three-dimensional InAs/GaAs quantum-dot crystals. *Appl. Phys. Lett.*, 88(4):043112, 2006.

[LHM+02] J. H. Li, V. Holý, M. Meduňa, S. C. Moss, A. G. Norman, A. Mascarenhas, and J. L. Reno. Lateral composition modulation in $InAs_n/AlAs_m$ short-period superlattices investigated by high-resolution x-ray scattering. *Phys. Rev. B*, 66(11):115312, 2002.

[LNG+99] B. Legrand, J. P. Nys, B. Grandidier, D. Stievenard, A. Lemaitre, J. M. Gerard, and V. Thierry-Mieg. Quantum box size effect on vertical self-alignment studied using cross-sectional scanning tunneling microscopy. *Appl. Phys. Lett.*, 74(18):2608–2610, 1999.

[LO05] B. Lounis and M. Orrit. Single-photon sources. *Rep. Prog. Phys.*, 68(5):1129–1179, 2005.

[LSGS04] Xiaoqin Li, D. Steel, D. Gammon, and L.J. Sham. Optically driven quantum computing devices based on semiconductor quantum dots. *Quant. Inform. Process.*, 3(1–5):147–161, 2004.

[May01] P. Mayer. Finite element calculation of the elastic relaxation in PbSe quantum dots and quantum dot superlattices. Master's thesis, Johannes Kepler Universität Linz, 2001.

[MKMR+03] A. Malachias, S. Kycia, G. Medeiros-Ribeiro, R. Magalhaes-Paniago, T. I. Kamins, and R. Stanley Williams. 3D composition of epitaxial nanocrystals by anomalous x-ray diffraction: Observation of a Si-rich core in Ge domes on Si(100). *Phys. Rev. Lett.*, 91(17):176101, 2003.

[MMPKC04] A. Malachias, R. Magalhaes-Paniago, S. Kycia, and David G. Cahill. X-ray study of strain and composition of $Si/Ge_{0.85}Si_{0.15}$ (111) islands grown in Volmer-Weber mode. *J. Appl. Phys.*, 96(6):3234–3238, 2004.

[MMPN+01] A. Malachias, R. Magalhaes-Paniago, B. R. A. Neves, W. N. Rodrigues, M. V. B. Moreira, H.-D. Pfannes, A. G. de Oliveira, S. Kycia, and T. H. Metzger. Direct observation of the coexistence of coherent and incoherent InAs self-assembled dots by x-ray scattering. *Appl. Phys. Lett.*, 79(26):4342–4344, 2001.

[MPMRM+02] R. Magalhaes-Paniago, G. Medeiros-Ribeiro, A. Malachias, S. Kycia, T. I. Kamins, and R. Stan Williams. Direct evaluation of composition profile, strain relaxation, and elastic energy of Ge:Si(001) self-assembled islands by anomalous x-ray scattering. *Phys. Rev. B*, 66(24):245312, 2002.

[MRG+01] E. Moreau, I. Robert, J. M. Gerard, I. Abram, L. Manin, and V. Thierry-Mieg. Single-mode solid-state single photon source based on isolated quantum dots in pillar microcavities. *Appl. Phys. Lett.*, 79(18):2865–2867, 2001.

[MS87] O. Madelung and M. Schulz, editors. *Landolt-Börnstein: Numerical Data and Functional Relationships in Science and Technology*, volume 22a, page 142. Springer-Verlag Berlin, 1987.

[MS05] D. J. Mowbray and M. S. Skolnick. New physics and devices based on self-assembled semiconductor quantum dots. *J. Phys. D: Appl. Phys.*, 38(13):2059–2076, 2005.

[MSC98] J. Miao, D. Sayre, and H. N. Chapman. Phase retrieval from the magnitude of the Fourier transforms of nonperiodic objects. *J. Opt. Soc. Am. A*, 15(6):1662, 1998.

[MWHM99] I. Mukhametzhanov, Z. Wei, R. Heitz, and A. Madhukar. Punctuated island growth: An approach to examination and control of quantum dot density, size, and shape evolution. *Appl. Phys. Lett.*, 75(1):85–87, 1999.

[nex] http://www.wsi.tu-muenchen.de/nextnano3/index.htm.

[NMSS05] Y. Nabetani, T. Matsumoto, G. Sasikala, and I. Suemune. Theory of strain states in InAs quantum dots and dependence on their capping layers. *J. Appl. Phys.*, 98(6):063502, 2005.

[PBWR03] F. Poster, A. Bhattacharya, S. Weeke, and W. Richter. Growth of spatially ordered InAs quantum dots on step-bunched vicinal GaAs (1 0 0) substrate. *J. Cryst. Growth*, 248:317–321, 2003.

[PK50] M. Peach and J. S. Koehler. The forces exerted on dislocations and the stress fields produced by them. *Phys. Rev.*, 80(3):436–439, 1950.

[PSHD00] G. Park, O. B. Shchekin, D. L. Huffaker, and D. G. Deppe. Low-threshold oxide-confined 1.3-μm quantum-dot laser. *IEEE Photon. Technol. Lett.*, 13:230–232, 2000.

[PSV+02] M. Pelton, C. Santori, J. Vuckovic, Bingyang Zhang, G. S. Solomon, J. Plant, and Yoshihisa Yamamoto. Efficient source of single photons: A single quantum dot in a micropost microcavity. *Phys. Rev. Lett.*, 89(23):233602, 2002.

[RHH+02] T. Roch, V. Holý, A. Hesse, J. Stangl, T. Fromherz, G. Bauer, T. H. Metzger, and S. Ferrer. Strain in buried self-assembled SiGe wires studied by grazing-incidence x-ray diffraction. *Phys. Rev. B*, 65(24):245324, 2002.

[RKvK01] A. Rastelli, M. Kummer, and H. von Känel. Reversible shape evolution of Ge islands on Si(001). *Phys. Rev. Lett.*, 87(25):256101, 2001.

[RV01] I. K. Robinson and I. A. Vartanyants. Use of coherent x-ray diffraction to map strain fields in nanocrystals. *Appl. Surf. Sci.*, 182:186, 2001.

[RVW+01] I. K. Robinson, I. A. Vartanyants, G. J. Williams, M. A. Pfeifer, and J. A. Pitney. Reconstruction of the shapes of gold nanocrystals using coherent x-ray diffraction. *Phys. Rev. Let.*, 87(19):195505, 2001.

[Sch04] M. Schmidbauer. *X-ray Diffuse Scattering from Self-Organized Mesoscopic Semiconductor Structures*, volume 199 of *Springer Tracts in Modern Physics*. Springer-Verlag, 2004.

[SDH+01] J. Stangl, A. Daniel, V. Holý, T. Roch, G. Bauer, I. Kegel, T.H. Metzger, Th. Wiebach, O.G. Schmidt, and K. Eberl. Strain and composition distribution in uncapped SiGe islands from X-ray diffraction. *Appl. Phys. Lett.*, 64:1474, 2001.

[SE01] O.G. Schmidt and K. Eberl. Self-assembled Ge/Si dots for faster field-effect transistors. *IEEE Trans. Electron Devices*, 48(6):1175–1179, 2001.

[SFP+02] C. Santori, D. Fattal, M. Pelton, G. S. Solomon, and Y. Yamamoto. Polarization-correlated photon pairs from a single quantum dot. *Phys. Rev. B*, 66(4):045308, 2002.

[SG02] G. Saint-Girons. *Epitaxie en phase vapeur aux organométalliques et caractérisations structurales et optiques de boîtes quantiques d'In(Ga)As pour l'émission autour de* 1.3 μm *sur substrat de GaAs.* PhD thesis, Universite Paris 6, 2002.

[SGPL+02] G. Saint-Girons, G. Patriarche, L. Largeau, J. Coelho, A. Mereuta, J.M. Gerard, and I. Sagnes. Metal-organic vapor-phase epitaxy of defect-free InGaAs/GaAs quantum dots emitting around 1.3 μm. *J. Cryst. Growth*, 235:89–94, 2002.

[SGPMS02] G. Saint-Girons, G. Patriarche, A. Mereuta, and I. Sagnes. Origin of the bimodal distribution of low-pressure metal-organic-vapor-phase-epitaxy grown InGaAs/GaAs quantum dots. *J. Appl. Phys.*, 91(6):3859–3863, 2002.

[SHB04] J. Stangl, V. Holý, and G. Bauer. Structural properties of self-organized semiconductor nanostructures. *Rev. Mod. Phys.*, 76(3):725, 2004.

[SHH+03] J. Stangl, A. Hesse, V. Holý, Z. Zhong, G. Bauer, U. Denker, and O.G. Schmidt. Effect of overgrowth temperature on shape, strain, and composition of buried Ge islands deduced from x-ray diffraction. *Appl. Phys. Lett.*, 82(14):2251, 2003.

[SHPB98] G. Springholz, V. Holý, M. Pinczolits, and G. Bauer. Self-organized growth of three-dimensional quantum-dot crystals with fcc-like stacking and a tunable lattice constant. *Science*, 282:734, 1998.

[SJPL+00] O. G. Schmidt, N. Y. Jin-Phillipp, C. Lange, U. Denker, K. Eberl, R. Schreiner, H. Grabeldinger, and H. Schweizer. Long-range ordered lines of self-assembled Ge islands on a flat Si (001) surface. *Appl. Phys. Lett.*, 77(25):4139–4141, 2000.

[SKN+02] O.G. Schmidt, S. Kiravittaya, Y. Nakamura, H. Heidemeyer, R. Songmuang, C. Müller, N.Y. Jin-Phillipp, K. Eberl, H. Wawra, S. Christiansen, H. Gräbeldinger, and H. Schweizer. Self-assembled semiconductor nanostructures: climbing up the ladder of order. *Surf. Sci.*, 514:10–18, 2002.

[SKS03] R. Songmuang, S. Kiravittaya, and O. G. Schmidt. Shape evolution of InAs quantum dots during overgrowth. *J. Cryst. Growth*, 249:416–421, 2003.

[SMPF98] T. Salditt, T. H. Metzger, J. Peisl, and R. Feidenhans. Elastic scattering under simultaneous excitation of x-ray standing waves in multilayers. *J. Appl. Phys.*, 83(10):5197, 1998.

[SMSV01] P. Sutter, E. Mateeva-Sutter, and L. Vescan. Oblique stacking of three-dimensional dome islands in Ge/Si multilayers. *Appl. Phys. Lett.*, 78(12):1736–1738, 2001.

[SNS99] Hideaki Saito, Kenichi Nishi, and Shigeo Sugou. Shape transition of InAs quantum dots by growth at high temperature. *Appl. Phys. Lett.*, 74(9):1224–1226, 1999.

[Spr05] G. Springholz. Three-dimensional stacking of self-assembled quantum dots in multilayer structures. *C. R. Physique*, 6(1):89–103, 2005.

[SRB+00] J. Stangl, T. Roch, G. Bauer, I. Kegel, T. H. Metzger, O. G. Schmidt, K. Eberl, O. Kienzle, and F. Ernst. Vertical correlation of SiGe islands in SiGe/Si superlattices: X-ray diffraction versus transmission electron microscopy. *Appl. Phys. Lett.*, 77(24):3953–3955, 2000.

[SSC+02] T. U. Schülli, M. Sztucki, V. Chamard, T. H. Metzger, and D. Schuh. Anomalous x-ray diffraction on InAs/GaAs quantum dot systems. *Appl. Phys. Lett.*, 81:448–450, 2002.

[SSH+05] T. U. Schülli, M. Stoffel, A. Hesse, J. Stangl, R. T. Lechner, E. Wintersberger, M. Sztucki, T. H. Metzger, O. G. Schmidt, and G. Bauer. Influence of growth temperature on interdiffusion in uncapped SiGe-islands on Si(001) determined by anomalous x-ray diffraction and reciprocal space mapping. *Phys. Rev. B*, 71(3):035326, 2005.

[SSZ+03] T. U. Schülli, J. Stangl, Z. Zhong, R. T. Lechner, M. Sztucki, T. H. Metzger, and G. Bauer. Direct determination of strain and composition profiles in SiGe islands by anomalous x-ray diffraction at high momentum transfer. *Phys. Rev. Lett.*, 90:066105, 2003.

[ST00] B.J. Spencer and J. Tarsoff. Dislocation energetics in epitaxial strained islands. *Appl. Phys. Lett.*, 77(16):2533, 2000.

[ST01] B.J. Spencer and J. Tarsof. Stress and first-order dislocation energetics in equilibrium Stranski-Krastanov islands. *Phys. Rev. B*, 63:205424, 2001.

[Tha04] V. Le Thanh. Mechanisms of self-organization of Ge/Si(001) quantum dots. *Phys. E: Low-dimensional Systems and Nanostructures*, 23(3-4):401–409, 2004.

[VCG+00] A. Vailionis, B. Cho, G. Glass, P. Desjardins, David G. Cahill, and J. E. Greene. Pathway for the strain-driven two-dimensional to three-dimensional transition during growth of Ge on Si(001). *Phys. Rev. Lett.*, 85(17):3672–3675, 2000.

[VRO+05] I. A. Vartanyants, I. K. Robinson, J. D. Onken, M. A. Pfeifer, G. J. Williams, F. Pfeiffer, H. Metzger, Z. Zhong, and G. Bauer. Coherent x-ray diffraction from quantum dots. *Phys. Rev. B*, 71(24):245302, 2005.

[WKSL01] L.G. Wang, P. Kratzer, M. Scheffler, and Q.K.K. Liu. Island dissolution during capping layer growth interruption. *Appl. Phys. A*, 73:161, 2001.

[WLS+04] X.-D. Wang, N. Liu, C. K. Shih, S. Govindaraju, and Jr. A. L. Holmes. Spatial correlation-anticorrelation in strain-driven self-assembled InGaAs quantum dots. *Appl. Phys. Lett.*, 85(8):1356–1358, 2004.

[WPVR03] G. J. Williams, M. A. Pfeifer, I. A. Vartanyants, and I. K. Robinson. Three-dimensional imaging of microstructure in Au nanocrystals. *Phys. Rev. Lett.*, 90(17):175501, 2003.

[WSH+00] Th. Wiebach, M. Schmidbauer, M. Hanke, H. Raidt, R. Köhler, and H. Wawra. Strain and composition in SiGe nanoscale islands studied by x-ray scattering. *Phys. Rev. B*, 61(8):5571–5578, 2000.

[XJX+99] Huaizhe Xu, Weihong Jiang, Bo Xu, Wei Zhou, and Zhanguo Wang. Two-dimensional ordering of self-assembled $In_xGa_{1-x}As$ quantum dots grown on GaAs(3 1 1)B surfaces. *J. Cryst. Growth*, 206(4):279–286, 1999.

[XMCK95] Qianghua Xie, Anupam Madhukar, Ping Chen, and Nobuhiko P. Kobayashi. Vertically self-organized InAs quantum box islands on GaAs(100). *Phys. Rev. Lett.*, 75(13):2542, 1995.

[YLL04] Bin Yang, Feng Liu, and M. G. Lagally. Local strain-mediated chemical potential control of quantum dot self-organization in heteroepitaxy. *Phys. Rev. Lett.*, 92(2):025502, 2004.

[ZB04] Zhenyang Zhong and G. Bauer. Site-controlled and size-homogeneous Ge islands on prepatterned Si (001) substrates. *Appl. Phys. Lett.*, 84(11):1922, 2004.

[ZCS+04] Zhenyang Zhong, Gang Chen, J. Stangl, Th. Fromherz, F. Schäffler, and G. Bauer. Two-dimensional lateral ordering of self-assembled Ge islands on patterned substrates. *Physica E*, 21:588, 2004.

[ZDM+01] D. Zhi, H. Davock, R. Murray, C. Roberts, T. S. Jones, D. W. Pashley, P. J. Goodhew, and B. A. Joyce. Quantitative compositional analysis of

InAs/GaAs quantum dots by scanning transmission electron microscopy. *J. Appl. Phys.*, 89(4):2079–2083, 2001.

Acknowledgement

I would like to express my thanks to many people who have supported me during my PhD studies and made this work possible. There are so many that I can not list them all by name. My gratitude goes to:

- Prof. Václav Holý (MU Brno) for guidance, rewarding and inspiring discussions on theoretical as well as experimental topics, and for his help with implementations of numerical calculations.

- Prof. Günther Bauer for guidance, for providing me the invaluable possibility to join the X-ray group at JKU Linz, for managing so many things which are on the background of the thesis, and for his encouragements.

- Dr. Julian Stangl (JKU Linz) and Dr. Petr Mikulík (MU Brno) for proofreading my thesis and for discussions on many practical issues during my studies. Dr. Bärbel Krause (ESRF Grenoble, France) for inspiring suggestions to Sec. 4.2, for her excellent support during many synchrotron beamtimes at the ESRF, and for fruitful discussions. I appreciate the encouragements from all three of them and their passion for physics, by which I was infected. Dr. Mojmír Meduňa (JKU Linz and MU Brno) for long-lasting cooperation, for his readiness to help with every possible technical problem, and for his teaching of patience.

- Dr. Zhenyang Zhong, Dr. Gang Chen (both JKU Linz), Dr. Suwit Kiravittaya (MPI Stuttgart, Germany), Dr. G. Saint-Girons (LPN Paris) for growth of the investigated samples and for many fruitful discussions.

- Dr. T. Fromherz (JKU Linz) for performing PL measurements and extensive discussions on the topic. Prof. F. Schäffler (JKU Linz) and Dr. L. Largeau (LPN Paris) for discussions on TEM.

- Dr. T. H. Metzger (ID01 beamline), Dr. B. Struth, Dr. O. Konovalov (both from ID10B beamline), Dr. N. Schell, and Dr. D. Dekadjevi (both from the ROBL beamline) at the ESRF; Dr. D. Novikov (D4 beamline) and Dr. S. Bessedine (BW2 beamline) at the HASYLAB (Hambrurg, Germany); Dr. N. Darowski and Prof. A. Erko from the KMC2 beamline at BESSY (Berlin, Germany) for their support during synchrotron measurements.

- Prof. J. Humlíček, head of the Institute of Condensed Matter Physics at MU Brno, for providing the conditions, which allowed me to finish the thesis at the institute.

- My colleagues at the Institute of Semiconductor Physics at JKU Linz:
  Dr. R. T. Lechner, A. Hesse, A. Rehman, and E. Wintersberger, ...
  My colleagues at the Institute of Condensed Matter Physics at MU Brno:
  Assoc. Prof. J. Kuběna, Assoc. Prof. Z. Bochníček, O. Caha, P. Klang, V. Křápek, Assoc. Prof. D. Munzar, and A. Dubroka ....

- Administrative staff: S. Lechner, S. Stadler (JKU Linz), and J. Schmidtová (MU Brno).

- ...

- Last but not least to my parents Miroslava Nováková and Ivo Novák, my brother, and close friends.

Publications and presentations

Publications

- J. Novák, V. Holý, J. Stangl, T. Fromherz, Zhenyang Zhong, Gang Chen, G. Bauer, and B. Struth. Ge/Si islands in a three-dimensional island crystal studied by x-ray diffraction. *J. Appl. Phys.,* 98(7):073517, 2005.

- J Novák, V Holý, J Stangl, G Bauer, E Wintersberger, S Kiravittaya, and O G Schmidt. A method for the characterization of strain fields in buried quantum dots using x-ray standing waves. *J. Phys. D: Appl. Phys.,* 38(10A):A137–A142, 2005.

- O. Caha, P. Mikulík, J. Novák, V. Holý, S. C. Moss, A. Norman, A. Mascarenhas, J. L. Reno, and B. Krause. Spontaneous lateral modulation in short-period superlattices investigated by grazing-incidence x-ray diffraction. *Phys. Rev. B,* 72(3):35313, 2005.

- M Meduňa, J Novák, C V Falub, G Chen, G Bauer, S Tsujino, D Grützmacher, E Müller, Y Campidelli, O Kermarrec, D Bensahel, N Schell. High temperature investigations of Si/SiGe based cascade structures using x-ray scattering methods. *J. Phys. D: Appl. Phys.,* 38(10A):A121-A125, 2005.

- M. Meduňa, J. Novák, G. Bauer, V. Holý, C. V. Falub, S. Tsujino, E. Müller, D. Grützmacher, Y. Campidelli, O. Kermarrec, and D. Bensahel. Annealing studies of high Ge composition SiGe/Si multilayers. *Z. Kristallogr.,* 219:195–200, 2004.

Talks

- *X-ray diffraction structural study of Ge/Si islands in a 3D island crystal.* J. Novák, V. Holý, J. Stangl, T. Fromherz, Zhenyang Zhong, Gang Chen, G. Bauer, and B. Struth. 6th Autumn School on X-ray Scattering from Surfaces and Thin Layers, Smolenice (Slovakia), 2005.

- *Structural characterization of Ga(In)As/GaAs nano-islands.* J. Novák, V. Holý, J. Stangl, G. Bauer, and G. Saint-Girons. Workshop "Characterization of thin films by X-ray scattering", Uckley (Germany), 2003.

Posters

- *A method for the characterization of strain fields in buried quantum dots using x-ray standing waves.* J. Novák, V. Holý, J. Stangl, G. Bauer, E. Wintersberger, S. Kiravittaya, and O. G. Schmidt. 7th Biennial Conference on High Resolution X-ray Diffraction and Imaging: X-top; Průhonice near Prgue (Czech Republic), 2004.

- *X-ray study of 3D InAs quantum dot crystal grown on patterned GaAs substrate.* J. Novák, B. Krause, G. Bauer, V. Holý, T. H. Metzger, S. Kiravittaya, and O. G. Schmidt. 13th International Winterschool on New Developments in Solid State Physics: Low Dimensional Systems; Mauterndorf (Austria), 2004.

Curriculum Vitae

Jiří Novák

21. Feb. 1976	born in Brno (Czech Republic)
1982–1990	primary school in Brno
1990–1994	grammar school in Brno (Matyáš Lerch gymnasium)
1994–1999	Studies of physics, Faculty of Science, Masaryk University Brno; Diploma thesis: *Monochromatization of X-rays with metallic multilayers;* Supervisor: Assoc. Prof. J. Kuběna
Oct 2000 – Apr 2002	Civil service in Brno
1999–2006	PhD studies at the Department of Condensed Matter Physics, Masaryk University Brno; Supervisor: Prof. V. Holý; (in Sept 2000 PhD studies interrupted due to the civil service for 18 months) since Sept 2002 PhD studies also at the Department for Semiconductor Physics at the Johannes Kepler University Linz (Austria); Supervisor: Prof. G. Bauer; (joint supervision of the thesis)